

Quantitative PET/CT imaging biomarkers in Lung Disease

Andrew Thornton

Institute of Nuclear Medicine, Division of Medicine, UCL

This dissertation is submitted for the PhD degree

Primary PhD Supervisor: Professor Ashley Groves

Secondary PhD Supervisor: Professor Jo Porter

I, Andrew Thornton, confirm that the work presented in this thesis is my own. Where information has been derived from other sources, I confirm that this has been indicated in the thesis.

Thesis Contribution

My contribution to the Lung Cancer work of this thesis includes the patient recruitment and selection, obtaining results, patient follow-up, analysis and presentation. I personally collected the clinical data for all patients from UCLH as well as from the Lister Hospital and the Princess Alexandra hospital, including patient details, basic histology and survival for all patients. I re-staged all patients as per TNM 8th edition guidelines, measured the ¹⁸F-FDG-PET biomarkers and segmented the entire collection using the TexRAD software. I performed a subset of the CT Perfusion segmentations. I validated the histology results – identifying several issues with the distribution of the results. I performed the majority of the Survival analysis and other statistical analyses.

In the COVID-19 project I was involved at all stages of the project from initial conception to write-up. I personally selected the patients, reviewed their studies and determined their clinical diagnosis. Measurement of the SUV and TBR_{lung} biomarkers were performed by a second reader in order to ensure that results were completely blinded. The selection of patients involved the creation of several small software aids which were written in their entirety by me. The statistical analysis, selection of results and write up of the paper was by me.

Impact Statement

It is estimated that up to half of the UK population will be affected by cancer during their lifetime (1, 2). Whilst half of all people diagnosed with cancer will survive their disease for ten years or more – there is a wide variation in survival between different cancer types and only 9.5% of those diagnosed with non-small cell lung cancer will survive for ten years or more (2, 3).

Imaging plays a crucial role in the detection of cancer, assessment of suitability for and planning of treatment, and assessment of response to treatment. The Tumour-Node-Metastasis (TNM) cancer staging system is the globally recognised standard used for cancer registration of almost all cancers, in particular non-small cell lung cancer, and it categorises patients into stages by the size and spread of disease (4). These stages predict survival and suitability for treatments but these are coarse qualitative categorical determinations which do not completely or fully explain patient survival and prognostication of individual patient survival is poor.

The incompleteness of the staging system assessment of prognosis is further highlighted with the development of treatments specifically tailored to individual tumour characteristics, for example anti-angiogenesis therapies, tyrosine-kinase inhibitors and checkpoint inhibitors. These treatments are only effective in subsets of patients with mutations relating to the expression of cell-receptors.

The work in this thesis provides evidence to suggest that quantitative imaging biomarkers can improve prognostication, predict immunohistochemical expression and mutation status, and thereby contributes to developing, and ultimately delivering, non-invasive precision medicine approaches in patients with non-small cell lung cancer. In particular cut-offs of $SUV_{max} > 7.6$ & $TBR_{lung} > 26.2$ predict prognosis, and more strongly $entropy_{ct_ssf_2} > 4.81$ is an independent predictor of survival in a combined model with staging and survival, it also stratifies survival when there mutations present.

In addition, the thesis also demonstrates that the quantitative techniques are helpful beyond cancer, and can provide additional information in interstitial lung disease. In particular, it demonstrates that ^{18}F -FDG uptake in COVID-19 increases with time after infection and correlates with severity, and provides evidence for the utility of steroid treatment in PCLD as this treatment is associated with reduced ^{18}F -FDG uptake in these patients.

UCL Research Paper Declaration Form: referencing the doctoral candidate's own published work(s)

Please use this form to declare if parts of your thesis are already available in another format, e.g. if data, text, or figures:

- 1 have been uploaded to a preprint server;
- 2 are in submission to a peer-reviewed publication;
- 3 have been published in a peer-reviewed publication, e.g. journal, textbook.

This form should be completed as many times as necessary. For instance, if you have seven thesis chapters, two of which containing material that has already been published, you would complete this form twice.

1 For a research manuscript that has already been published (if not yet published, please skip to section 2):		
1 Where was the work published? (e.g. journal name)	Journal of Nuclear Medicine	
2 Who published the work? (e.g. Elsevier/Oxford University Press):	Society of Nuclear Medicine and Molecular Imaging	
3 When was the work published?	01/02/2022	
4 Was the work subject to academic peer review?	Yes	
5 Have you retained the copyright for the work?	No	
[If no, please seek permission from the relevant publisher and check the box next to the below statement]:		
<input checked="" type="checkbox"/> <i>I acknowledge permission of the publisher named under 1b to include in this thesis portions of the publication named as included in 1a.</i>		
2 For a research manuscript prepared for publication but that has not yet been published (if already published, please skip to section 3):		
1 Has the manuscript been uploaded to a preprint server? (e.g. medRxiv):	Please select.	If yes, which server? Click or tap here to enter text.
2 Where is the work intended to be published? (e.g. names of journals that you are planning to submit to)	Click or tap here to enter text.	
3 List the manuscript's authors in the intended authorship order:	Click or tap here to enter text.	
4 Stage of publication	Please select.	
3 For multi-authored work, please give a statement of contribution covering all		



authors (if single-author, please skip to section 4):			
<p>Andrew Thornton: Conceptualization, Methodology, Software, Validation, Formal Analysis, Investigation, Data Curation, Writing – Original, Review, Editing Francesco Fraioli, Simon Wan, Helen S. Garthwaite, Stefan Vöö, Irfan Kayani, Deena Neriman, Leon Menezes, Jamshed Bomanji, Toby Hillman, Melissa Heightman – Review, Some data-acquisition Balaji Ganeshan – Formal Analysis (Statistics) Robert I. Shortman: Resources, Project administration Raymond Endozo – Formal Analysis (Some Image Processing) Joanna C. Porter and Ashley M. Groves – Supervision, Editing, Review, Funding acquisition.</p>			
4 In which chapter(s) of your thesis can this material be found?			
Chapter7:			
5 e-Signatures confirming that the information above is accurate (this form should be co-signed by the supervisor/ senior author unless this is not appropriate, e.g. if the paper was a single-author work):			
Candidate:		Date:	12/08/2022
Supervisor/ Senior Author (where appropriate):		Date:	12/08/2022

Table of Contents

Thesis Contribution	3
Impact Statement	4
UCL Research Paper Declaration Form: referencing the doctoral candidate's own published work(s)	6
Glossary of Abbreviations	14
General	14
Statistical	15
Histopathological	15
Diffuse Lung Diseases	16
¹⁸ F-FDG-PET/CT	17
CT Perfusion	17
Textural Analysis	18
Scientific Units	18
1 Introduction	20
1.1 Lung Cancer	20
1.1.1 Epidemiology	20
1.1.2 Diagnosis and Staging	21
1.1.3 Treatment	21
1.1.4 Prognosis	22
1.2 Diffuse Lung Disease	23
1.2.1 Disease Tempo	24
1.2.2 Radiological Pattern	25
1.2.3 Clinical Context	26
1.2.4 Treatment	26
1.2.5 Prognosis	27
1.2.6 Coronavirus Disease 2019 (COVID-19) and Post-COVID-19 Lung Disease (PCLD)	27
1.3 Imaging Biomarkers	29
1.4 ¹⁸ F-FDG-PET	31
1.5 CT Perfusion	33
1.6 Texture Analysis	37
1.6.1 Model-Based Approaches	37
1.6.2 Geometrical and Structural Approaches	38
1.6.3 Statistical and Histogram Metric Approaches	39
1.6.4 Signal Processing (Transform and Filtration) Approaches	40
1.6.5 TexRAD: Combined Signal Processing (Filtration) and Statistical Approach	40
2 Methodology	42
2.1 Introduction	42
2.2 Lung Cancer Patient Population	42
2.3 ¹⁸ F-FDG-PET/CT Imaging Protocol	42
2.4 ¹⁸ F-FDG-PET/CT Image Analysis	43
2.4.1 Tumour SUV _{max}	43
2.4.2 Tumour SUV _{mean}	43
2.4.3 Tumour SUV _{min}	43

2.4.4	Normal Vessel SUV_{max}	43
2.4.5	Normal Lung SUV_{max} , SUV_{mean} and SUV_{min}	44
2.4.6	Tumour Target-to-Background Ratio (TBR_{lung})	44
2.4.7	Tumour Dimensions	44
2.5	CT Perfusion Population	44
2.6	CT Perfusion Imaging Protocol	44
2.7	CT Perfusion Image Analysis	45
2.7.1	CTP4 Average	45
2.7.2	CTP4 Base	45
2.7.3	CTP4 Time to Peak (TTP)	45
2.7.4	CTP4 Positive Enhancement Integral	46
2.7.5	CTP4 Mean Slope of Increase	46
2.7.6	CTP4 Blood Volume (BV)	46
2.7.7	CTP4 Blood Flow (BF)	46
2.7.8	CTP4 Mean Transit Time (MTT)	46
2.7.9	CTP4 Time of Arrival (IRF(t_0))	47
2.7.10	CTP4 Time to Maximum (t_{Max})	47
2.7.11	CTP4 Permeability Surface Area Product (PS)	47
2.8	TexRAD Population	47
2.9	TexRAD Image Analysis	47
2.9.1	Mean intensity (mean)	48
2.9.2	Standard Deviation (sd)	48
2.9.3	Shannon Entropy (entropy)	48
2.9.4	Mean of Positive Pixels (mpp)	48
2.9.5	Histogram Skewness (skewness)	49
2.9.6	Histogram Kurtosis (kurtosis)	49
2.10	Histology Population	49
2.11	Immunohistochemistry	50
2.12	Mutation Analysis	51
2.13	Statistics and Data Analysis	52
2.14	List of total biomarkers studied	52
2.14.1	^{18}F -FDG-PET quantitative biomarkers	52
2.14.2	CT Perfusion quantitative biomarkers	53
2.14.3	TexRAD derived biomarkers	53
3	^{18}F -FDG-PET Quantitative Biomarkers in Lung Cancer	55
3.1	Abstract	55
3.1.1	Purpose	55
3.1.2	Methods	55
3.1.3	Findings	55
3.1.3.1	Patient Demographics	55
3.1.3.2	Age and Surgical Status	55
3.1.3.3	Disease Stage	56
3.1.3.4	SUV_{max}	56
3.1.3.5	TBR_{lung}	56
3.1.4	Conclusion	56

3.2 Introduction.....	57
3.3 Materials and Methods	59
3.3.1 Patient Population	59
3.3.2 ¹⁸ F-FDG-PET/CT Imaging Protocol.....	59
3.3.3 ¹⁸ F-FDG-PET/CT Image Analysis	59
3.3.4 Statistics and Data Analysis.....	59
3.4 Findings.....	60
3.4.1 Patient Demographics.....	60
3.4.2 Age and Surgical Status.....	60
3.4.3 Disease Stage	60
3.4.4 SUV _{max}	61
3.4.5 SUV _{max} in Non-Surgical Patients.....	61
3.4.6 SUV _{max} in Surgical Patients.....	61
3.4.7 SUV _{mean}	61
3.4.8 TBR _{lung}	62
3.5 Discussion	63
3.6 Conclusion	65
3.7 Tables.....	66
3.8 Figures	72
4 CT Perfusion in Lung Cancer.....	74
4.1 Abstract.....	74
4.1.1 Purpose	74
4.1.2 Methods.....	74
4.1.3 Findings.....	74
4.1.3.1 Patient Demographics.....	74
4.1.3.2 CT Perfusion and Survival.....	74
4.1.3.3 CT Perfusion and SUV _{max}	75
4.1.3.4 CT Perfusion and Surgery.....	75
4.1.3.5 CT Perfusion and Nodal Status.....	75
4.1.4 Conclusion.....	75
4.2 Introduction.....	76
4.3 Materials and Methods	77
4.3.1 Patient Population	77
4.3.2 ¹⁸ F-FDG-PET/CT Imaging Protocol.....	77
4.3.3 CT Perfusion Imaging Protocol.....	77
4.3.4 ¹⁸ F-FDG-PET/CT Image Analysis	77
4.3.5 CT Perfusion Image Analysis	77
4.3.6 Statistics and Data Analysis.....	77
4.4 Findings.....	78
4.4.1 Patient Demographics.....	78
4.4.2 Age and Surgical Status.....	78
4.4.3 Disease Stage	78
4.4.4 SUV _{max}	78
4.4.5 Correlation Between Non-Deconvolution and Deconvolution Dependent Biomarkers	79

4.4.6	CT Perfusion Measures Against Survival.....	79
4.4.7	Can CT Perfusion Predict SUV _{max} ?.....	79
4.4.8	Can CT Perfusion Predict Surgery?	80
4.4.9	Can CT Perfusion Predict Nodal Status?	80
4.4.10	Can CT Perfusion Predict Metastatic Status?.....	80
4.4.11	Can CT Perfusion Predict Survival in Non-Surgical Higher Stage Disease Treated with Chemotherapy?	80
4.4.12	Can CT Perfusion Predict Histological Subtype?.....	81
4.5	Discussion	82
4.6	Conclusion	84
4.7	Tables.....	85
4.8	Figures	89
5	Texture Analysis with TexRAD in Lung Cancer	92
5.1	Abstract.....	92
5.1.1	Purpose	92
5.1.2	Methods.....	92
5.1.3	Findings.....	92
5.1.3.1	Patient Demographics.....	92
5.1.3.2	Individual TexRAD Biomarkers at Median Cut-Point Across the Whole Cohort	92
5.1.3.3	Individual TexRAD Biomarkers at Optimal Cut-point for Stage I Across the Whole Cohort	93
5.2	Introduction.....	94
5.3	Materials and Methods	95
5.3.1	Patient Population	95
5.3.2	¹⁸ F-FDG-PET/CT Imaging Protocol.....	95
5.3.3	¹⁸ F-FDG-PET/CT Image Analysis	95
5.3.4	TexRAD Image Analysis	95
5.3.5	Statistics and Data Analysis.....	95
5.4	Findings.....	96
5.4.1	Individual TexRAD Biomarkers at Median Cut-Point Across the Whole Cohort.....	96
5.4.2	Individual TexRAD Biomarkers at Optimal Cut-Point for Stage I Across the Whole Cohort.....	96
5.4.3	Training and Testing Cohort Analysis	96
5.4.4	Correlation Between TexRAD Biomarkers	97
5.5	Discussion	98
5.6	Conclusion	100
5.7	Tables.....	101
5.8	Figures	106
6	Correlation Between Immunohistochemistry and Mutation and Imaging Biomarkers.....	109
6.1	Abstract.....	109
6.1.1	Purpose	109
6.1.2	Methods.....	109
6.1.3	Results.....	109
6.1.4	Conclusion.....	110

6.2 Introduction.....	111
6.2.1 Inflammation	112
6.2.2 CA-IX.....	113
6.2.3 CD105.....	113
6.2.4 GLUT1.....	113
6.2.5 HIF-1 α	113
6.2.6 MCM2	113
6.2.7 VEGF.....	114
6.2.8 BRAF.....	114
6.2.9 EGFR.....	114
6.2.10 HER2.....	115
6.2.11 KRAS.....	115
6.2.12 PI3KCA.....	115
6.3 Materials and Methods	117
6.3.1 Patient Population	117
6.3.2 ¹⁸ F-FDG-PET/CT Imaging Protocol.....	117
6.3.3 ¹⁸ F-FDG-PET/CT Image Analysis	117
6.3.4 Textural Analysis	117
6.3.5 CT Perfusion Imaging Protocol.....	117
6.3.6 CT Perfusion Image Analysis	117
6.3.7 Immunohistochemistry.....	117
6.3.8 Mutation Analysis	117
6.3.9 Statistical Analysis.....	117
6.4 Results	118
6.4.1 Patient Demographics.....	118
6.4.2 Inflammation	118
6.4.3 CA-IX.....	118
6.4.4 CD105.....	118
6.4.5 GLUT1.....	119
6.4.6 HIF-1 α	119
6.4.7 MCM2	119
6.4.8 VEGF.....	119
6.4.9 BRAF.....	119
6.4.10 EGFR.....	119
6.4.11 HER2.....	120
6.4.12 KRAS.....	120
6.4.13 PI3KCA.....	120
6.4.14 No Mutation Detected.....	120
6.4.15 Multivariate and Univariate Survival Analysis	120
6.5 Discussion	121
6.6 Conclusion	125
6.7 Tables.....	126
6.8 Figures	135
7 Evolution of ¹⁸ F-FDG-PET/CT Findings in Patients Following COVID-19: An Initial Investigation.....	137

7.1 Abstract.....	137
7.1.1 Purpose	137
7.1.2 Methods.....	137
7.1.3 Results.....	137
7.1.4 Conclusion.....	137
7.2 Introduction.....	138
7.3 Materials and Methods	140
7.3.1 Ethics.....	140
7.3.2 Patient Selection	140
7.3.3 ¹⁸ F-FDG-PET/CT Imaging Protocol.....	140
7.3.4 Determination of Temporal Stage.....	141
7.3.5 Quantitative ¹⁸ F-FDG-PET Analysis	141
7.3.6 Statistics	141
7.4 Results	142
7.4.1 Temporal Stage	142
7.4.2 Association of Pulmonary ¹⁸ F-FDG-Uptake with Temporal-staging in Early & Late Stage Disease	142
7.4.3 Pulmonary ¹⁸ F-FDG-Uptake in PCLD	143
7.5 Discussion	144
7.5.1 Limitations	144
7.6 Conclusion	146
7.7 Figures	147
7.8 Tables.....	150
8 Limitations.....	153
8.1 Lung Cancer Dataset.....	153
8.2 COVID-19 Dataset.....	154
9 Conclusion	155
9.1 ¹⁸ F-FDG PET/CT Biomarkers	155
9.2 CT Perfusion in Lung Cancer	155
9.3 Texture Analysis with TexRAD in Lung Cancer	155
9.4 Correlation Between Immunohistochemistry and Mutation and Imaging Biomarkers.....	156
9.5 Evolution of ¹⁸ F-FDG-PET/CT Findings in Patients Following COVID-19	156
9.6 Further Work	157
9.7 Summary.....	157
Bibliography.....	159

Glossary of Abbreviations

General

Abbreviation	Description
^{18}F	Fluorine-18
^{18}F -FDG	2-deoxy-2-(^{18}F)-fluoro-D-glucose
^{18}F -FDG-PET/CT	2-deoxy-2-(^{18}F)-fluoro-D-glucose Positron Emission Tomography/Computed Tomography
2D	Two-dimensional
3D	Three-dimensional
BI-RADS	Breast Imaging Reporting and Database System
CT	Computed Tomography
EBUS	Endobronchial Ultrasound
EBUS-TNA	Endobronchial Ultrasound-guided Transbronchial Needle Aspiration
EUS-FNA	Endoscopic Ultrasound-guided Fine-Needle Aspiration
FDA–NIH	Food and Drug Administration – National Institutes of Health (United States)
GE	General Electric Company
ILD	Interstitial Lung Disease
LVEF	Left Ventricular Ejection Fraction
MDT	Multi-Disciplinary Team
MRI	Magnetic Resonance Imaging
NSCLC	Non-small cell Lung Cancer
PET	Positron Emission Tomography
ROI	Region of Interest
SABR	Stereotactic Ablative Radiotherapy
TNM	Tumour-Node-Metastasis Staging System
TNM8	8 th Edition of the TNM staging system

Abbreviation	Description
UK	United Kingdom
USA	United States of America
VOI	Volume of Interest
WHO	World Health Organization

Statistical

Abbreviation	Description
AIC	Akaike Information Criterion
AUC	Area Under the Curve
CI	Confidence Interval
HR	Hazard Ratio
IQR	Interquartile Range
ROC	Receiver Operating Characteristic curve

Histopathological

Abbreviation	Description
Akt	Ak strain Transforming protein and gene (also known as Protein Kinase-B)
ATP	Adenosine Triphosphate
B-Raf	B-Rapidly Accelerated Fibrosarcoma kinase protein
BAI	Binary sequencing Alignment Index file
BAM	Binary sequencing Alignment Map file
BED	Browser Extensible Data file
BRAF	B-Rapidly Accelerated Fibrosarcoma kinase gene
DNA	Deoxyribonucleic acid
dsDNA	Double-stranded DNA
EGFR	Endothelial Growth Factor Receptor
ERK	Extracellular signal-related kinase(s)

Abbreviation	Description
FFPE	Formalin-Fixed Paraffin-Embedded
GLUT	Glucose transporter membrane protein
HER2	Human Epidermal Growth Factor Receptor 2
HIF	Hypoxia Induced Factor
IFC	Integrated Fluidic Circuit
IGV	Integrative Genomics Viewer software
ILD	Interstitial Lung Disease
K-Ras	Kirsten Rat Sarcoma Virus protein
KRAS	Kirsten Rat Sarcoma Virus gene
MAPK	Mitogen-activated protein kinase(s)
NSCLC	Non-small cell Lung Cancer
PCR	Polymerase Chain Reaction
PI3K	Phosphatidylinositol 3-Kinase protein and its associated protein cascade
PIK3CA	Phosphatidylinositol-4,5-bisphosphate 3-kinase catalytic subunit alpha gene
Raf	Rapidly Accelerated Fibrosarcoma kinase proteins
SNP	Single-Nucleotide Polymorphism
SOP	Standard Operating Procedure
VEGF	Vascular Endothelial Growth Factor
WT	Wild Type

Diffuse Lung Diseases

Abbreviation	Description
ARDS	Acute Respiratory Distress Syndrome
COP	Cryptogenic Organizing Pneumonia
COVID-19	Coronavirus Disease 2019
DLD	Diffuse Lung Disease

Abbreviation	Description
GGO	Ground-Glass Opacity
ILD	Interstitial Lung Disease
IPF	Idiopathic Pulmonary Fibrosis
LCH	Langerhan's Cell Histiocytosis
MERS-CoV	Middle Eastern Respiratory Syndrome – Coronavirus
PCLD	Post-COVID-19 Lung Disease
SARS-CoV-1	Severe Acute Respiratory Syndrome – Coronavirus – 1
SARS-CoV-2	Severe Acute Respiratory Syndrome – Coronavirus – 2

¹⁸F-FDG-PET/CT

Abbreviation	Description
C_{img}	Image-derived concentration of radioactive tracer
C_{inj}	Whole-body concentration of injected radioactive tracer
MTV	Metabolic Tumour Volume
NTV	Necrotic Tumour Volume
SUV	Standardised Uptake Value
SUV_{max}	Maximum SUV in a ROI or VOI
SUV_{mean}	Average SUV in a ROI or VOI
SUV_{min}	Minimum SUV in a ROI or VOI
TBR	Target-to-Background Ratio
TBR_{lung}	Target-to-Background Ratio of lesion to normal lung
TLG	Total Lesion Glycolysis
TTV	Total Tumour Volume

CT Perfusion

Abbreviation	Description
ADW	Advantage Workstation for Diagnostic Imaging (GE Healthcare)

Abbreviation	Description
BF	Blood Flow
BV	Blood Volume
CTP	CT Perfusion
CTP4	CT Perfusion 4D: CT Perfusion imaging analysis platform by GE Healthcare
IRF	Impulse-Residue Function
IRF(t_0)	Time of Arrival
MTT	Mean Transit Time
PS	Permeability Surface Area Product
SPV	Standardised Perfusion Value
t_{max}	Time to Maximum
TTP	Time-to-Peak

Textural Analysis

Abbreviation	Description
GLCM	Grey-level Co-occurrence Matrix
GLRLM	Grey-level Run-length Matrix
mpp	Mean of Positive Pixels
sd	Standard Deviation
SSF	Spatial Scale Factor
TexRAD	Texture + Radiology: A proprietary clinical-research texture analysis software platform from Feedback Medical Limited

Scientific Units

Abbreviation	Description
cm	Centimetre
HU	Hounsfield Unit
kg	Kilogram
kV	Kilovolt

Abbreviation	Description
mA	Milliampere
MBq	Megabecquerel
mm	Millimetres
ng	Nanogram
pM	Picomole
s	Second

1 Introduction

This thesis will investigate quantitative molecular imaging techniques for the development of imaging biomarkers in lung disease. Firstly, it addresses focal lung disease in the investigation of non-small cell lung cancer, and secondly investigate diffuse lung disease in patients with SARS-CoV-2 induced lung disease.

1.1 Lung Cancer

1.1.1 Epidemiology

Lung cancer is the third most common cancer in the UK, with approximately 48,500 new cases every year accounting for 13% of all new cancer cases in 2016–2018 (5). Globally it is the largest contributor to new cancer diagnoses, and the largest cause of cancer-related death worldwide (6).

The incidence of lung cancer in the UK has decreased by 9% since the early 1990s, although this has mostly been driven by a 34% reduction in males and masks a 32% increase in the females. Still one in 13 UK males and one in 15 UK females will be diagnosed in lung cancer during their lives. Globally, incidence rates are increasing, although they are falling in the developed world due to tobacco control policies (7). Incidence rates are highest in people aged 85–89 and 44% of all new lung cancer diagnoses occur in people aged 75 or over (5).

In the UK, 79% of lung cancer cases are thought to be preventable, with 72%–90% caused by smoking (1% of these due to second-hand smoke) and 13% by workplace exposure (8–10). It is estimated that 86% of all UK lung cancer deaths are caused by tobacco smoking (11–13).

Like most sporadic cancers, it is hypothesized that repeated exposure to carcinogens, especially the tar components of cigarette smoke, lead to dysplasia and mutagenesis within the lung epithelium and eventually carcinogenesis (14).

Lung cancers are classified histopathologically by cellular and molecular subtypes using the 2021 World Health Organization (WHO) classification system (15). The three main subtypes of non-small cell lung cancer are: adenocarcinoma (40%), squamous-cell

carcinoma (25%) and large cell carcinoma (10%). Subtypes are determined using cytology and immunohistochemistry staining, with immunohistochemistry staining playing a pivotal role in most classifications (9, 15).

1.1.2 Diagnosis and Staging

Imaging plays a paramount role in the diagnosis, staging and management of lung cancer. Once lung cancer is suspected a diagnostic contrast-enhanced CT Chest and Abdomen is performed and often following that a whole body ¹⁸F-FDG-PET/CT. Pathological correlation with image-guided or flexible-bronchoscopic biopsy of the primary lung lesion and/or endobronchial ultrasound-guided transbronchial needle aspiration (EBUS-TNA) or endoscopic ultrasound-guided fine-needle aspiration (EUS-FNA) of lymph nodes is also often performed to stage and diagnose disease (16). MRI is not routinely used to stage the primary tumour but does play a role in the staging of tumours which involve the superior sulcus and are suspected to be Pancoast tumours. (Pancoast tumours are tumours which are suspected to have invaded the apical chest wall, brachial plexus, first ribs, vertebrae, subclavian vessels or stellate ganglion.) (16) Initial clinical staging is then performed using the Tumour-Node-Metastasis (TNM) system (4). Following evaluation of the above imaging an initial clinical stage is assigned. In Stage I, unless the patient has symptoms, no dedicated brain imaging is performed. In Stage II, if curative treatment is planned, a contrast-enhanced CT Brain will be performed and followed-up with a contrast-enhanced brain MRI if there are suspected brain metastases. Patients with Stage III disease who are planned for curative treatment will have a contrast-enhanced brain MRI. Otherwise, in cases where there are features suggestive of intracranial pathology brain imaging is always performed.

The above findings inform the clinical stage and will upgrade or downgrade the stage as appropriate.

1.1.3 Treatment

The first step recommended for treatment of any lung cancer is to advise patients to stop smoking as soon as lung cancer is suspected. Not only does smoking increase the risk of pulmonary complications after lung cancer surgery, it reduces survival after

treatment (17). It is however, recommended not to postpone definitive treatment to allow for patients to stop smoking: smoking cessation should therefore be concurrent with diagnostics and treatment (16).

In patients who are well enough and curative treatment is suitable, the mainstay of treatment is surgical lobectomy. Patients are assessed for their risk of perioperative mortality, their cardiovascular function optimised and re-vascularisation will be considered before surgery. Lung function with spirometry and transfer factor will be assessed, along with a functional segment count to predict postoperative lung function (16).

If lobectomy is declined or contraindicated in early-stage non-nodal disease (Stages I–IIA), radical radiotherapy with stereotactic ablative radiotherapy (SABR) or sublobar resection may be considered (16).

More extensive surgery including extrapleural resection or en-bloc chest wall resection may be required for more extensive disease (16).

In patients with Stage II or III disease in whom surgery is contraindicated or declined chemoradiotherapy will be recommended. If, however, chemotherapy is contraindicated or not tolerated, then radical radiotherapy alone is not recommended. In addition, in surgical patients who have nodal disease or T2b–T4 N0 disease, adjuvant chemotherapy will be offered (16).

1.1.4 Prognosis

In the UK 21% of all cancer deaths are accounted for by Lung Cancer making it the most common cause of cancer death (1, 5). Prognostication is most often performed using staging with the Tumour-Node-Metastasis (TNM) system (4), however these stages are somewhat coarse and survival within these groups is heterogeneous.

Whilst there has been substantial improvement in one year survival of non-small cell lung cancer from 16% in 1971–72 to 40.6% in 2013–2017, long-term survival remains poor with only 16.2% surviving for five or more years (2, 5).

The one year survival rate for Stage I disease is 88% vs 19% at Stage IV (3). Five year survival for Stage I is 57% vs 3% for Stage IV (3, 5). Survival is significantly higher for females than for males at all stages.

The poor overall survival is partially accounted for by the relatively late presentation of disease, with 46.1% of patients having Stage IV at diagnosis. (19.5% Stage I, 7.4% Stage II, 20.1% Stage III, 46.1% Stage IV and 6.9% Stage Unknown.) (5, 7)

1.2 Diffuse Lung Disease

Diffuse lung disease is used to describe any widespread pulmonary disease process (18, 19). The typical presentation of patients affected by diffuse lung disease is one of breathless with bilateral shadowing present on plain chest radiographs. The severity of breathless can be variable, as can the rate of onset, and a typical patient presentation may range from the asymptomatic patient with apparently isolated and long-standing radiological changes, to acute respiratory failure with rapid progressively worsening breathless and ultimately death (18–20).

The causes of diffuse lung disease are wide and varied — and it is helpful to consider these conditions in relation to lung anatomy (18–21). Many of these diseases will foremost affect the interstitium of the lung — that is the fibrous framework of connective tissue of the lung. These diseases fall under the umbrella terms of Diffuse Interstitial Lung Diseases or Interstitial Lung Diseases (ILD) (18, 19).

Not all diffuse lung diseases primarily affect the interstitium. Whilst the connective tissue framework surrounds the bronchovascular bundles centrally — peripherally, it forms the interlobular septa, defining and organising the lung into secondary pulmonary lobules consisting of lymphatics, venules and acini supplied by a bronchiole and pulmonary arteriole centrally. A process that affects the airways, the vasculature or airspaces can also cause diffuse bilateral shadowing on radiographs and hence would also be considered a diffuse lung disease (18–22).

Unsurprisingly, this wide variation of presentation, prognosis and underlying physiology means that there is a wide range of aetiologies and mechanisms of disease that can

cause diffuse lung disease. Therefore when presented with a patient with a diffuse lung disease of unknown aetiology determination of that aetiology and the diagnosis in order to prognosticate and suggest treatment cannot be made only on radiological appearances alone and requires a combined clinikoradiological approach (18, 20, 21).

Three parameters are most commonly used to narrow the differential diagnosis, guide further evaluation and potential treatment. (20, 21) These are:

- 1 The tempo of the disease process (acute vs chronic.)
- 2 Radiological pattern (on chest radiographs and/or high-resolution CT chest.)
- 3 Clinical context.

1.2.1 Disease Tempo

The duration and progression of potentially relevant symptoms help a clinician to determine the tempo of a pathological process. This may include review of previous radiological imaging. Assessment of disease tempo forms part of the initial assessment (18, 20).

Diffuse lung diseases that are acute (less than 4–6 weeks in duration) most commonly include infectious causes (e.g. bacterial or viral pneumonias), pulmonary oedema be it cardiogenic or non-cardiogenic, haemorrhage or aspiration (18, 20).

Some ILDs may also present acutely, even if the disease process is itself chronic. Most commonly these would include hypersensitivity pneumonitis, drug-induced lung disease, toxin-related pneumonitis, acute eosinophilic pneumonia and cryptogenic organizing pneumonia (18–20).

Chronic diffuse lung diseases are dominated by ILDs but represent many distinct clinicopathological entities with different prognoses, potential treatments and causes. The most common ILDs include: Idiopathic pulmonary fibrosis (IPF), sarcoidosis, connective tissue disorder associated ILDs, pneumoconioses, chronic hypersensitivity pneumonitis and drug-induced lung disease (18–21).

Clearly for patients with a rapidly progressive diffuse lung disease, admission to hospital and empirical therapy is likely to be required (18).

1.2.2 Radiological Pattern

Bilateral pulmonary infiltrates could be used to describe a wide variety of radiological appearances. Closer review of the components of the pattern of opacities, distribution and associated findings can help to further narrow down the differential diagnosis. In addition to plain chest radiographs, high resolution chest CT is generally required to help elucidate this radiological pattern more accurately, especially for opacities other than consolidation (18–21).

Radiological patterns are usually grouped as following:

- Consolidation, due to alveolar filling with accumulated water, blood, cells, pus, or other material. It is characterised by hazy margins, coalescing areas of relatively high attenuation which may contain air bronchograms and/or loss of definition of borders due to adjacent consolidation effacing normally present air/soft-tissue border. (Also known as the silhouette sign) (20, 21).
- Reticular and linear patterns, where interstitial infiltrates cause a thickening of intralobular septae and the appearance of lines, arcs or honeycombing on imaging (18–21).
- Nodules and nodular opacities, ranging in number, size and distribution. This runs the gamut from diffuse micronodular opacities in miliary TB to large nodules in pneumoconioses (18–21).
- Cysts due to destruction of lung architecture, as in for example, Langerhan's cell histiocytosis (LCH), pneumocystis, or idiopathic pulmonary fibrosis (IPF) (18–21).
- Ground-glass opacities (GGO) refer to hazy increases in lung attenuation but not so much that there is effacement of the pulmonary vessels. The mechanism here is thought to be partial filling of the alveolar spaces and/or interstitial thickening (20, 21).

- Septal thickening where interstitial infiltrates cause thickening of the interlobular septae. Irregular, beaded and nodular thickening suggest lymphatic spread of the tumour or cells as in sarcoidosis. Smooth thickening could imply pulmonary oedema (18–21).

Associated intra-thoracic findings such as pleural effusions or thickening and lymphadenopathy as well as extra-thoracic findings help further narrow the differential diagnosis.

1.2.3 Clinical Context

Further refining of the differential diagnosis requires clinical correlation. Integrating the clinical context with the radiological pattern and tempo of disease guides further evaluation and helps to focus the differential diagnosis. Some diseases are strongly associated with characteristic epidemiological features, e.g. IPF predominantly affects middle-aged and older patients whereas lymphangioleiomyomatosis occurs almost exclusively in women of reproductive age. Smoking is another factor, as are environmental and or occupational exposures (18–20).

Drugs and pre-existing diseases may provide further clues as to the nature and aetiology of a diffuse lung disease. Certain medications such as amiodarone are strongly associated with ILD as are connective tissue diseases such as sarcoidosis and neurocutaneous syndromes such as tuberous sclerosis (18–20).

1.2.4 Treatment

As diffuse lung diseases are an umbrella condition with multiple different aetiologies and thence clinical courses there is no unifying treatment and treatment needs to be tailored to the specific, often presumed, aetiology (18, 19).

Patients with bacterial infections will often require antibiotic therapy, and may require further imaging following treatment to ensure resolution and that the disease was not a super-added infection. Similarly, those with TB and other mycobacterial infections require anti-mycobacterial therapy. Patients with viral infections may benefit from anti-virals, but supportive care alone is likely to be effective as most viral infections are self-limiting (18, 19).

In contrast, patients with auto-immune and suspected inflammatory conditions will often benefit from steroid therapy or anti-autoimmune drugs. Antifibrotic therapy is a promising new treatment for IPF — however ultimately the only treatment may be total lung transplantation (18, 19).

Neoplastic or paraneoplastic processes will require cancer treatment and cessation of smoking. Diseases such as desquamative interstitial pneumonia and LCH may resolve completely with cessation of smoking (18, 19).

1.2.5 Prognosis

As with treatment, the prognosis of a diffuse lung disease is intimately linked to its aetiology. Some diseases like bacterial pneumonia have an established and effective treatment and hence whilst some cases may be acutely life-threatening requiring multiple organ support or have significant sequelae like a risk of lung abscess, the prognosis is good. Others, like IPF, have poorly or only partially effective treatments. The only completely effective treatment for IPF appears to be lung transplantation which is not suitable for a lot of patients due to underlying co-morbidities and age. However, without lung transplantation median survival is only three years (18, 19).

1.2.6 Coronavirus Disease 2019 (COVID-19) and Post-COVID-19 Lung Disease (PCLD)

Coronavirus Disease 2019 (COVID-19) is a contagious disease caused by the novel severe acute respiratory syndrome – coronavirus – 2 (SARS-CoV-2) virus. The first known case was identified in Wuhan, China in December 2019 (23) but despite efforts at containment, the virus rapidly spread worldwide and a pandemic was declared by the World Health Organization (WHO) on 11 March 2020 (24). The disease spread rapidly throughout London and the rest of the UK during late February–early March 2020 (25).

Coronavirus disease 2019 (COVID-19) has a large variety of clinical symptoms and manifestations, but within the lungs it primarily causes a bilateral interstitial pneumonia which can become severe with symptoms of dyspnoea, tachypnoea,

hypoxia, hypercapnia and the development of acute respiratory distress syndrome (ARDS) (23, 26–35).

The median time from onset of symptoms to admission to intensive care is 10 days, however, only up to 5% of unvaccinated patients will require admission to intensive care (23, 34–36). The protracted clinical course, in contrast to the rapid course expected of viral disease (35, 37), suggests that the acute lung changes and damage may be a consequence of inflammation from the adaptive immune response rather than from the virus itself (35, 38).

On CT imaging, COVID-19 typically presents with ground-glass opacities (GGOs) and/or bilateral pulmonary consolidation in multiple segmental and subsegmental regions. In early stages, changes are often limited to peripheral GGOs and bronchovascular thickening (26–29, 31–33). Consolidation and spread to the centre of the lungs occurs later (26–28, 30–33) with subpleural sparing and development of organising pneumonia occurring even later (26–28, 31–33, 38). The appearance of recovery and chronic changes remains poorly described (39). Many other signs such as interlobular septal thickening and crazy paving have also been demonstrated (33, 39) however, other typical pulmonary infection features: enlarged lymphadenopathy, pulmonary nodules, pleural effusions and cavitation are not commonly observed, except as features of intercurrent disease e.g. heart failure (26). Lymphadenopathy although not a common feature may be associated with prognosis (40). The overall findings are similar to those described in Middle Eastern respiratory syndrome – coronavirus (MERS-CoV) and severe acute respiratory syndrome – coronavirus (SARS-CoV-1) (26, 30).

Patients with COVID-19 may have a prolonged or delayed recovery with a reduced transfer factor of the lung for carbon monoxide (DLCO) noted at discharge in >40% patients (41) and approximately two-thirds of hospitalised patients have persistent symptoms post-COVID-19 with at least one-third suffering respiratory symptoms (42–45). It is notable that permanent lung damage has been demonstrated following severe respiratory disease associated with infection with other beta-coronaviruses such as

SARS-CoV-1 and MERS-CoV (44, 46, 47). It may be difficult to determine whether those patients who are slow to recover represent a cohort with a novel interstitial lung disease, or post-COVID-19 lung disease (PCLD), or whether their slow recovery is due to other factors such as fatigue or cardiac inflammation.

¹⁸F-FDG-PET/CT imaging has been shown to have utility in the diagnosis, prognostication and management of diffuse lung disease and ILDs like IPF (48–53) where inflammation and fibroblast proliferation have been associated with increased ¹⁸F-FDG avidity. It would be reasonable to hope that, whilst the role of nuclear imaging in acute or recovering COVID-19 is minimal (37), there may be a role for ¹⁸F-FDG-PET/CT in the diagnosis and potential management of patients with persistent symptoms and the diagnosis of PCLD.

1.3 Imaging Biomarkers

A biomarker is a “defined characteristic that is measured as an indicator of normal biological processes, pathogenic processes or responses to an exposure or intervention, including therapeutic interventions” (54). The FDA–NIH Biomarker Working Group definition includes “molecular, histologic, radiographic or physiologic characteristics ...” (55). Imaging biomarkers can represent some direct measurement of some underlying biomarker, but this is not necessarily the case, nor do they have to have a putative diagnostic or prognostic use (54–56).

Before a putative imaging biomarker can be used to guide clinical decisions, there are two fundamental translational gaps that they must cross. The so-called “first gap in translation” relates to the process of evaluating a putative imaging biomarker and assessing if it can be a robust enough and reliable measure to be used in clinical research. The “second gap in translation” relates to integrating a proven biomarker into patient management and pathways. Many putative biomarkers fail at the second gap and many more fail at the first gap. Even if a putative biomarker can be shown to be robust and reliable it may be impracticable or too expensive to use in routine clinical care; however, these could still play a significant role in clinical research.

Examples of currently used imaging biomarkers in clinical care include clinical TNM Staging, BI-RADS in breast cancer, left ventricular ejection fraction (LVEF), T-score and Z-score from DEXA bone density studies, and Deauville scale in lymphoma, amongst others.

An imaging biomarker can be quantitative e.g. SUV_{max} or categorical e.g. TNM Stage. They are considered as distinct entities separate from the underlying modality or technique that the measurement is derived from, and a single imaging measurement can provide measurements for multiple imaging biomarkers. For example, an ^{18}F -FDG-PET/CT may provide measurements of the SUV_{max} , TBR_{lung} , texture measurements and clinical stage.

If a quantitative biomarker is to guide therapy or help diagnose, it will often need to be categorized by splitting a biomarker above and below a critical cut-off point. Blood glucose in the diagnosis of diabetes mellitus is often the traditional non-imaging example; however, imaging biomarker examples include the diagnosis of anthracycline-induced cardiotoxicity with a reduction of LVEF $\geq 10\%$ below the lower-limit for normal (itself another example of a critical cut-off point) (57).

Although some imaging biomarkers can be considered to have direct, and sometimes indirect, correlated and established histopathological or pathophysiological biomarkers, e.g. LVEF, many imaging biomarkers do not and establishing reference models (biological or otherwise) can be difficult and not cost-effective. This is particularly relevant for cut-offs mentioned above. This can lead to problems with validation, repeatability and reproducibility. Technical, biological and clinical validation with multicentre and multivendor reproducibility is often deferred, or performed in parallel with the development of the biomarker. This lack of reference models also means that technical validation and cost-effectiveness needs to be re-evaluated as imaging software and hardware improves (58, 59).

It is the intention of this thesis to predominantly focus on imaging biomarker discovery, although, as mentioned above validation and discovery of imaging biomarkers go hand-in-hand.

1.4 ¹⁸F-FDG-PET

¹⁸F-FDG-PET provides a measure of glucose metabolism as it is actively transported in to cells through glucose transporters (GLUTs), and then phosphorylated by hexokinases to ¹⁸F-FDG-6-phosphate. ¹⁸F-FDG-6-phosphate will then accumulate in cells as cannot be further metabolised until the ¹⁸Fluorine decays into ¹⁸Oxygen through emission of a positron, or the ¹⁸F-FDG-6-phosphate is dephosphorylated by phosphatases (56, 60, 61). Metabolically active cells, often cancerous cells, will therefore accumulate ¹⁸F-FDG. Although full metabolism of the glucose is an oxygen dependent process, the initial phosphorylation of glucose is not, and hypoxia induces cells to increase expression of GLUTs and thus uptake and accumulation of ¹⁸F-FDG and ¹⁸F-FDG-6-phosphate. In this way ¹⁸F-FDG uptake is increased in hypoxic and metabolically active cells (56, 62), however it is difficult to differentiate between the aerobic and anaerobic induced uptake, and tumours with low metabolic rates or low glucose uptake, e.g. mucinous adenocarcinomas will have falsely reassuring low ¹⁸F-FDG avidity (56).

In non-small cell lung cancer staging, ¹⁸F-FDG-PET/CT is used primarily as means of additional assessment of T-stage, to help assess nodal stage and help guide EBUS targeting and to help rule out metastatic spread. T-stage is often more clearly demonstrated on contrast CT however, in cases of downstream consolidation and lung collapse the size of metabolic volume can help more clearly determine T-stage. However, the main usefulness lies in nodal staging and distant spread: meta-analyses have shown that ¹⁸F-FDG-PET/CT has significantly improved sensitivity and specificity for nodal metastases and distant metastases over those for CT alone, with the exception of brain metastases (16, 63–67).

The standardised uptake value (SUV) is a semi-quantitative method for assessing ¹⁸F-FDG uptake and thence glucose metabolism (68). The SUV is the ratio of the image-derived radioactivity concentration (c_{img}) and the whole body concentration of the injected radioactivity (c_{inj}) (56, 69). The maximum SUV (SUV_{max}) is the maximum voxel value of SUV in a volume of interest, often the tumour. As tumours are often much more avid than the surrounding normal lung parenchyma, measuring the SUV_{max} of a tumour is generally simple and easily reproducible, making it an observer independent

parameter. The SUV_{max} is therefore the most commonly used parameter in clinical practice and was the first parameter considered as prognostic biomarker (69). Various prognostic thresholds of SUV_{max} have been described for primary lung cancer, usually ranging from 5–20, but sometimes as low as 2.9 (69–71, 71–76, 76–93), and 5–10 in recurrence (76, 78, 94–100). However, consistency of results and predictions relating to any particular cut-off across studies has been poor and thus, although the SUV_{max} is commonly used in reporting to help make diagnostic decisions and inform staging, it has not directly been incorporated into staging systems like TNM 8 (4, 78, 90, 101–103).

It is often argued that SUV_{max} is a poor representation of the total tumour as it is derived from a single voxel, and therefore other measures have been proposed. SUV_{mean} is the average SUV value for some region of interest, often the whole tumour (78, 81, 85). The SUV_{min} similarly represents the minimum SUV value within that same region of interest. However, these apparently simple definitions omit the difficulties of the selection of the region of interest and segmenting the whole tumour. There are multiple options for the determination of the region or volume of interest but a common option is automatic voxel selection using a thresholding algorithm with a relative threshold of 40% of the SUV_{max} (85, 104, 105). These automatic techniques almost completely remove the problem of operator dependence, but these then suffer from several other problems. One is that necrotic areas of tumours will often be below the threshold and thus not included in the volume of the tumour. Another is that the estimated volume of a very avid tumour will be likely too small because the minimum threshold could be significantly above the background. A third common problem is that the 40% lower threshold boundary for poorly avid tumours is likely to be below the soft-tissue background SUV and thus lead to over-estimation of the size of the tumour. Alternative options include absolute thresholding with a fixed minimum SUV, and manual segmentation, though these also have challenges associated with them.

The calculated tumour volume has also been proposed as a potential measure. This can then be combined with other data to form synthetic measures. The metabolic tumour volume (MTV), is the calculated volume of the metabolically active region segmented

as described above (78, 85, 102, 104, 104–106) . Total lesion glycolysis (TLG) is a synthetic measure formed from the MTV multiplied with the SUV_{mean} of the volume (78, 85, 102, 104, 105). Some papers have suggested adding the necrotic tumour volume (NTV) to the MTV to obtain the total tumour volume (TTV) in non-surgical stage III/IV disease (107).

1.5 CT Perfusion

CT perfusion techniques permit the direct quantification of vascular function in a non-invasive manner. CT perfusion works by monitoring the first-pass of an iodinated contrast bolus through the vascular system and monitoring the change in attenuation or enhancement of a region or volume of interest (ROI/VOI) over time with a rapid-sequence of CT images at the same slice location (108). The change in attenuation or degree of enhancement of a region can be quantified in Hounsfield units, and is proportional to the concentration of iodine within the region of interest, in usual practice. Images are then processed to provide time-attenuation data and parameters such as enhancement rate can then be extracted. Enhancement rate is an example of a semi-quantitative biomarker being an approximate measurement of perfusion.

There is little-to-no intracellular absorption of iodinated contrast media and excretion is primarily via glomerular filtration. Thus, the pharmacokinetics of iodinated contrast media can be considered a multi-compartment model consisting of intravascular and extravascular spaces with contrast flowing between these spaces. Model parameters associated to flow within and into the intravascular space can be used as biomarkers assessing luminal vessels and microvessel density. Model parameters associated to flow into and out of the extravascular phase can be used as biomarkers assessing vascular permeability. This makes these agents well suited to the study of vascular changes within solid lesions, such as tumours (109, 110) and in tumours these pathological markers are associated with tumour angiogenesis, which is essential for tumour growth and metastasis. Morphologically, tumour angiogenesis is characterized by proliferation of blood vessels and capillaries, but this pathological growth involves the creation of malfunctioning and leaky vessels with irregular blood flow. Thus,

angiogenesis is associated with increased microvessel density and increased vascular permeability, and thence with the parameters associated with the intra-vascular and extra-vascular compartments.

These pharmacokinetics allow for three data analysis approaches (110–114):

- Model-independent approaches using the Fick principle (essentially conservation of mass) either through gradient/slope estimation or deconvolution. (This is essentially a 1-compartment model.)
- Compartmental modelling e.g. Patlak or Logan plot based analysis.
- Distributed parameter modelling of perfusion and capillary permeability.

Each approach has its own assumptions and, with those, its own sources of error, and there is no consensus on technique between manufacturers and providers of commercially available software (111, 112, 115, 116). Each approach also has different recommended acquisition protocols, and measurements acquired by different approaches are not interchangeable (112, 115, 116).

One assumption within basic two-compartment models is that there is a single supply of blood to the intravascular compartment(s). This assumption is clearly not correct within the liver, where the portal venous system provides a second supply, however, it is increasing recognised within lung lesions that lung lesions can have both pulmonary and bronchial arterial supply (117–123). In the liver, because of the inherent delay to portal enhancement, the two components of liver enhancement can be quantified separately using splenic enhancement to split the time-attenuation curve into arterial and portal venous phases, or through estimating the arterial input function of the portal vein and the aorta separately. Similarly, in the lung, one can use peak enhancement of the left atrium as the dividing line between pulmonary circulation and the bronchial circulation, or use ROIs taken from the pulmonary artery and aorta to estimate arterial input functions for the pulmonary arterial and bronchial arterial input respectively (119, 123). The effect on this dual input on the estimated parameters depends on the approach taken and the size of the tumour. In lung lesions, the

bronchial arterial input is usually dominant, and it becomes more dominant in larger tumours. The results of single-input analysis techniques will tend to estimate the bronchial arterial perfusion with the pulmonary perfusion acting as a cause for error in those estimates. Gradient/slope methods allow for the pulmonary arterial input to be essentially ignored and thus should be less badly affected by the dual-arterial supply (110, 121).

Another consideration is the effect of motion on the study. Not only is there the problem of patient movement, respiratory motion can be significant. CT perfusion acquisition can last up to a minute and lung cancer patients are often unable to hold their breath for that long. Clearly, if a lesion moves in and out of the VOI during the study the time-attenuation curves will be affected, and consequently any parameter estimated from these will also be affected. Several papers have shown improvements in reproducibility and using motion correction to re-register, translate and adjust the VOI to match the tumour timepoint-by-timepoint (124–127). Such corrections are complicated by the need to take account of the anisotropy in scaling between intra-axial movement and inter-slice movement, even if they elide more complex effects like partial volume effects and non-rigid transformations. However, motion correction software for lung lesions is poorly available and most centres do not have access to it (124). The effect of respiratory motion can however be reduced without software by noting that its effect is greatest on lesions lying most inferior within the lungs: mechanisms such as external binding, therefore, help reduce this by physically restricting motion (124).

Partial volume effects and stochastic noise are common problems with all functional imaging techniques. Partial volume effects are greatest for small structures and at tissue interfaces. Some suggest that ROIs should therefore be placed inside the boundaries of arteries or organs of interest; however whilst this is practicable for regions used for arterial input, this is unlikely to be the case for tumours. Image processing techniques such as region thresholding and blood-air fraction correction techniques may be used to exclude voxels most likely to be affected by these or to correct for the partial volume effects. The effect of stochastic noise, also known as

photon noise, can be reduced using reconstruction filters, higher radiation doses and/or by choosing larger regions of interest. Beam hardening is another artefact that requires consideration. High concentrations of contrast, calcium, external metalwork, and pacemakers or other implantable devices can all cause significant artefact.

The biomarkers derived from parameters of CT perfusion models can be considered as falling into two major groups: semi-quantitative and physiologic (110, 128). The semi-quantitative biomarkers consist of parameters which can be measured directly from the time-attenuation curves, e.g. peak enhancement, enhancement rate, time-to-peak, and area under the curve (AUC). These require minimal processing, but also represent a synthesis of intra- and extra-vascular components, and of cardiac-output. They are thus considered estimates, hence “semi-quantitative” rather than “quantitative”.

Physiologic biomarkers require more processing and are calculated from fitting one of the models above. These parameters themselves also fall into two major groups: those that (predominantly) measure intravascular components and those that measure extravascular components. Parameters measuring predominantly intravascular components consist of blood flow or perfusion (arterial/portal, bronchial/pulmonary arterial or comparisons thereof e.g. perfusion index), blood volume, mean transit-time. Permeability and permeability surface area products can be considered to be measuring the extra-vascular component (110, 129). The correlation and association between these CT perfusion biomarkers and the histopathological biomarkers of angiogenesis such as VEGF staining, luminal vessel number, area or perimeter, or microvessel density, appears complex, although blood flow has been shown to be correlated with luminal vessel area and perimeter (130–133). The complexity of the relationship between measured flow and microvessel density and other markers of angiogenesis should not be surprising as angiogenesis in cancer is disordered and associated with necrosis (128, 132–136).

CT perfusion biomarkers have been shown to differ between lung adenocarcinomas and squamous cell carcinomas (125, 133, 137, 138), and can be used to monitor anti-angiogenesis chemotherapy in unresectable lung cancer (139–142). Blood flow and standardized perfusion value (SPV) have also been shown to be associated with

regional lymph node metastasis (130, 143, 144). Dual-input perfusion CT biomarkers have been associated with predicting response to chemotherapy in advanced non-small cell lung cancer (NSCLC) (121, 145) and response to stereotactic ablative radiotherapy (SABR) (146). CT perfusion biomarkers have been shown to be predictive in differentiating between benign and malignant pulmonary nodules (126, 147–149). Permeability has been shown to predict survival in NSCLC (150), however later studies have shown that CT perfusion does not add significant information for initial staging as compared to ^{18}F -FDG-PET/CT (151).

1.6 Texture Analysis

Texture analysis is an image processing method to acquire additional quantitative information about a tumour's heterogeneity as reflected by the distribution of voxel values within an imaged volume, and provide biomarkers that try to represent the perceived texture of the volume similar to if one were to touch the object, i.e. does it appear smooth or rough, does it have a coarse or fine appearance, does it have a regular repeating pattern or is it irregular, and is there a directional or spatial bias.

Texture analysis as part of imaging processing has a long history and different authors have adapted its definition as per their field of application and there are multiple methods of generating biomarkers (152–166). A common thread throughout all these techniques is that the visual texture of a subject volume or region of interest is related to intensity variation, spatial organisation (e.g. is there a repeating pattern, are there edges, is the peak/minimum intensity centred) and directionality/isotropy/anisotropy (e.g. do the patterns repeat in a particular direction, are edges more defined in one direction than another, is there symmetry about some axis or not). The methods of parameter extraction can be loosely grouped into four (somewhat overlapping) groups: model-based, geometrical and structural, statistical and histogram metric, and signal processing (also known as transform or filtration) methods (163).

1.6.1 Model-Based Approaches

By modelling the region or volume of interest as a random distribution or other such model, biomarkers can be extracted that best describe this model. At the simplest

level, we can consider extracting the (first-order statistics) mean and standard deviation of the voxel intensities within a region of interest as attempting to loosely fit the distribution of the intensities (irrespective of location) to a normal distribution. More commonly, however, the models suggested will try to take account of the neighbourhoods of voxels. Common models include: autoregressive models (159, 163, 166), markov random field models or other random fields including Gibbs (159, 165), and Fractal models (159, 162, 164).

Autoregressive models treat the region of interest as a sequence of voxels where the probability that a voxel has some intensity is dependent on (some number of) the previous voxels in the sequence, usually in a linearly-dependent way. Autoregressive models may be further modified with a moving average component.

Markov random fields involve determining the probability that a voxel has a particular intensity as given the intensities of its neighbours (165). Gibbs random field models are similar but use a different sampling model, and with some caveats Gibbs random field models have corresponding Markov random field models, and vice versa. (See the Hammersley-Clifford theorem, also known as the Fundamental theorem of random fields.)

Fractal models most often use the box-counting (possibly cube-counting) algorithm to determine a measure of the fractal dimension across the region of interest. For a 2D ROI the value will be between 1 and 2, with higher values representing more coarseness and lower values more smoothness and self-similarity.

1.6.2 Geometrical and Structural Approaches

These approaches can be thought of a subset of the model-based approach.

The region of interest is considered to be constituted of repeating primitives which are laid out according to certain placement rules or other criteria. The layout pattern then gives a measure or description of the texture of the region, similar to the way tiles tessellate the plane. These approaches tend to only be appropriate for textures with a regular structure, and become non-optimal for images with irregular texture. However,

it is worth noting that techniques like this have been successful for assessing the texture of interstitial lung disease on diagnostic CT imaging (167).

1.6.3 Statistical and Histogram Metric Approaches

Statistical approaches to determining texture are based on the distribution and spatial orientation of grey-levels in images using various statistical computations. In general these characteristics can be further categorized in to first-order, second-order and higher-order statistics, depending on whether a statistic takes account of how a voxel's intensity relates to its neighbours (159). First-order statistics do not directly account for interactions between voxel intensity and neighbours: these include statistics and histogram metrics like the mean of the voxel intensities, standard deviation, skewness and entropy.

Second-order and higher-order statistics involve the creation of matrices that take account of the local environments of voxels such as a grey-level co-occurrence matrix (GLCM) (152, 155) or grey-level run-level matrix (GLRLM) amongst others (154, 156, 160, 163). Various statistics can be derived from these matrices including: contrast, correlation, energy, homogeneity, entropy (a different kind of entropy to above) and maximum probability (155).

Many of these approaches also involve some quantisation of the voxel intensities and have some inherent choice of directionality — in fact for GLCM and GLRLM methods, both quantisation into a number of grey-levels and a choice of direction is required. The $GLCM(g, d)$ for some number of grey-levels g and direction d is a 2D matrix (size $g \times g$) such that the value (i, j) is the probability (or number of times) that there is pair of adjacent voxels in the ROI in the d direction with the grey-levels (i, j) respectively. The $GLRLM(g, d)$ for some number of grey-levels g and direction d on a ROI with maximum width w in direction d is a 2D matrix (size $g \times w$) where value (i, j) is the probability of (or count of the number of times of) a run in direction d of adjacent voxels v_1, v_2, \dots, v_j all with the same intensity i . (The choice of whether these matrices use a probabilities or counts is dependent on implementation.)

Further, regions of interest may be pre-thresholded to remove or exclude too high or too low intensities preventing them from creating too much bias in the calculated biomarkers.

The number of options and choices here result in families of second-order statistics, and even first-order statistics, and can hinder reproducibility of results reported in papers.

1.6.4 Signal Processing (Transform and Filtration) Approaches

Using filters such as the Laplacian of Gaussian (band-pass filter) or Gaussian, discrete Fourier transformations, or wavelet filtering, one can transform the raw voxel intensities removing (possibly parts of) high or low frequency data, or, in the case of Fourier transformation transforming into frequency data. High-pass filters, such as the Laplacian, will tend to sharpen resulting images, enhancing edges and fine texture. Low-pass filters (such as the Gaussian) will tend to blur images smoothing out edges and thus highlighting rougher texture. Filters can be tuned to enhance or blur on different scales, with wider filters meaning that any particular transformed voxel intensity is affected by a larger number of its neighbours: thus a wider filter will necessarily tend to have a blurring effect, reducing higher frequency data and enhancing lower frequency data.

The resulting transformed intensity maps can then be further analysed with any of the above techniques, and in particular, any first-order statistic derived from these maps could be considered a second-order or higher-order statistic.

1.6.5 TexRAD: Combined Signal Processing (Filtration) and Statistical Approach

TexRAD (Feedback Medical Ltd., <https://fbkmed.com/textrad-landing-2/>, London/Cambridge, UK) is a proprietary clinical research texture analysis software platform which uses a combined filtration-histogram and statistical based approach.

Images are segmented on the platform manually or automatically, with voxels being further thresholded in a target dependent way. In lung CT, voxels within the ROI are thresholded by Hounsfield unit to avoid including air, calcification and bone. Images are passed through Laplacian of Gaussian spatial band-pass filters of varying radii as

represented by the spatial scale factor (SSF) and first-order statistics are then calculated for the ROI on these filtered images. By varying the radius of the filter from 2, 3, 4, 5, to 6mm, finer (higher frequency) to coarser (lower frequency) textural features are highlighted. A SSF radius of 0 is used to designate no filtering and statistics derived from the conventional image directly.

Texture biomarkers derived from this filtration-histogram and statistical approach used in TexRAD have been shown to be correlated with survival, response and histology in a number of cancers and have been shown to correlate with ^{18}F -FDG-PET SUV_{max} and CT Perfusion biomarkers (150, 161, 161, 161, 168–183).

2 Methodology

2.1 Introduction

The majority of this thesis (Chapters 3–6) investigates biomarkers in Lung Cancer. This chapter discusses the common methodology for these chapters. Chapter 7 will discuss its own methodology, but the ^{18}F -FDG-PET/CT imaging protocol and analysis is similar.

2.2 Lung Cancer Patient Population

This study was performed with the approval of the local medical ethics committee and all the enrolled patients gave their written informed consent to be in the study group after being apprised of the potential benefits and contraindications to CT perfusion and ^{18}F -FDG-PET/CT. 484 patients with suspected lung cancer were recruited to the study from August 2006 until December 2021. If a patient developed a metachronous lung cancer later only the initial lung cancer was considered. If a patient was considered for recruitment multiple times only the initial scan was considered.

Of these 484 patients, 475 patients ^{18}F -FDG-PET/CT imaging, the other nine patients were excluded.

Due to the inherent bias caused by pre-selecting patients who were thought likely to have non-small cell lung cancer, patients who were found not to have non-small cell lung cancer (NSCLC) on biopsy or on imaging were excluded from further analysis, leaving 293 patients.

2.3 ^{18}F -FDG-PET/CT Imaging Protocol

Patients were fasted for at least six hours and blood glucose levels were recorded prior to ^{18}F -FDG injection in all patients. Imaging was performed 60 minutes after intravenous injection of 5 MBq/Kg ^{18}F -FDG. Images were acquired from mid-thigh to the vertex of the skull, in the supine position with the arms raised above the head, using a GE Discovery 710 PET/CT scanner (GE Healthcare, Chicago, USA). A low-dose CT scan (120 kV, 30–200 mA modulated, and 0.8s rotation time and 40 collimation) was performed at the start of imaging to provide attenuation correction and an anatomical reference. PET data was in 3D mode with scan duration of two minutes per bed

position. A standard technique (random, scatter and attenuation) and an iterative reconstruction (matrix size 256x256, VUE Point FX 3D with two iterations, 24 subsets) corrected the emission data.

2.4 ¹⁸F-FDG-PET/CT Image Analysis

Images were processed using a standard protocol on a dedicated imaging workstation (Carestream Vue PACS Version 12.1.5.7014) and reviewed by two combined radiologist/nuclear medicine physicians in consensus. Both attenuation and non-attenuation corrected images were reviewed visually to determine the presence of attenuation corrected image artefacts from high density areas (48, 184). Staging was performed as per TNM8 guidelines (4) and it should be noted that it is this radiological staging that is used, rather than the formal multi-disciplinary team (MDT) or pathology derived staging as these staging determinations were not generally available. In addition, the following ¹⁸F-FDG-PET/CT biomarkers were then extracted:

2.4.1 Tumour SUV_{max}

The area of most intense pulmonary ¹⁸F-FDG uptake was identified and measured to obtain the maximum standardised uptake value (SUV_{max}).

2.4.2 Tumour SUV_{mean}

The lesion surrounding the most intense pulmonary was automatically segmented using a 40% threshold algorithm. The mean standardised uptake value (SUV_{mean}) was then extracted.

2.4.3 Tumour SUV_{min}

On the axial slice containing the SUV_{max} a region of interest (ROI) was drawn around the tumour and the minimum SUV found within that was used as the SUV_{min}.

2.4.4 Normal Vessel SUV_{max}

Using up to a 1cm diameter spherical volume of interest (VOI) the SUV_{max} of blood within the aorta or other normal vessel was measured to provide a normal background. The wall of the vessel was avoided.

2.4.5 Normal Lung SUV_{max}, SUV_{mean} and SUV_{min}

On axial slices at or near the level of the level of the carina, a 1cm diameter spherical VOI of morphologically normal lung parenchyma on the co-registered CT was selected. The SUV_{max} and SUV_{mean} were then measured and the SUV_{min} in a similar fashion to above.

2.4.6 Tumour Target-to-Background Ratio (TBR_{lung})

The lung target-to-background ratio (TBR_{lung}) was calculated as follows (TBR_{lung} = SUV_{max}/SUV_{min}) (48, 49).

2.4.7 Tumour Dimensions

The largest dimensions of the tumour in the axial plane were measured in centimetres.

2.5 CT Perfusion Population

Of the 293 patients with non-small cell cancer (NSCLC) who had ¹⁸F-FDG-PET/CT imaging described in Section 2.2, 131 patients had contraindications to CT perfusion or CT perfusion imaging failed. This left 162 patients who were eligible for study as part of the CT perfusion population.

2.6 CT Perfusion Imaging Protocol

All CT Perfusion scans were performed on an integrated PET/CT scanner combining PET with a 64-MDCT scanner (Discovery VCT, GE Healthcare). The ¹⁸F-FDG-PET/CT study was used to localize the lung tumour and perfusion CT was performed immediately after PET acquisition. The covered z-axis scan length was 4 cm to cover the whole tumour using the following acquisition parameters: 120 kV, 50 mAs, two second interval for 20 frames, and then a five second interval for 22 frames. The total imaging time was 150 seconds. The contrast media was injected into an antecubital vein by a dual head pump injection device (Stellant D, Medrad, USA). The CT perfusion study commenced immediately after IV administration of 50 ml of contrast agent (iohexol; 350 mg/mL iodine; Omnipaque, GE Healthcare) at 5 mL/s followed by a 50 mL saline chaser at 5 mL/s. All patients were instructed to breath shallowly and consistently in order to avoid excessive lung motion.

2.7 CT Perfusion Image Analysis

CT Perfusion Images were processed using a CT perfusion 4D software available on a dedicated imaging workstation (ADW volume 4.6 GE Healthcare, USA). Tumours were segmented and CT Perfusion analysis was performed by a radiographer with over 10 years' experience of tumour-segmentation and CT perfusion analysis. No automatic motion correction is performed by this software but images were reviewed for motion artefacts. CT perfusion 4D uses kinetic modelling is based on time-concentration curves from a reference arterial ROI and tissue VOI to calculate the impulse residue function (IRF) through deconvolution. The IRF represents the time-concentration curve that would have been obtained had there been a perfect injection of contrast agent with duration of one unit of time: also known as an *impulse*. This deconvolution method makes the assumption that the concentration of contrast material in the tissue is linearly dependent on the input arterial concentration when blood flow is constant. If this assumption holds then the $c(t)$, the concentration at time t within some tissue, is the result of the convolution of $a(t)$, the concentration within the artery at time t with the impulse residue function $IRF(t)$ (113, 185). The following biomarkers were extracted:

2.7.1 CTP4 Average

The CTP4 average is the average Hounsfield unit (HU) value of the volume of interest (VOI) across the study (185).

2.7.2 CTP4 Base

The CTP4 base is the average HU of the VOI in the base image (185).

2.7.3 CTP4 Time to Peak (TTP)

Time-to-peak is the time between the last image where there was no enhancement in the VOI and the image which has the maximal value before the first post-enhancement images. This uses the raw time curve data directly. TTP is computed and measured in seconds.

2.7.4 CTP4 Positive Enhancement Integral

The Positive Enhancement Integral is the sum of the difference between voxel HU value within the VOI at each time point and the voxel pre-enhancement HU value.

This measures the area under the time intensity curve giving a measurement of the degree of positive enhancement from the injection of the contrast.

2.7.5 CTP4 Mean Slope of Increase

The mean slope of increase is the average of the change in HU values of voxels in the VOI at each time-point (185).

2.7.6 CTP4 Blood Volume (BV)

The Blood Volume is computed as the product of the blood flow (BF) and the mean transit time (MTT). It estimates the volume of blood in ml per 100g of tissue (113, 185).

2.7.7 CTP4 Blood Flow (BF)

The Blood Flow corresponds to the blood flow entering and exiting a volume of tissue and is commonly known as perfusion. It is derived from the initial value of the impulse residue function and estimates the flow of blood in ml per 100g of tissue per minute (113, 185).

2.7.8 CTP4 Mean Transit Time (MTT)

Mean Transit Time estimates the average time of contrast agent residence in tissue, and thence the mean time taken by blood to pass through the capillary network. It is calculated as the first moment (equivalent to the mean) of the impulse residue function from the time of arrival. This is the mean time where the time is weighted by the impulse residue function (113, 185):

$$MTT = \frac{\sum_{t=0}^{\infty} (t - t_0) \times IRF(t)}{\sum_{t=0}^{\infty} IRF(t)}$$

2.7.9 CTP4 Time of Arrival (IRF(t₀))

The time of arrival is the time in seconds when contrast enhancement first occurs at the VOI.

2.7.10 CTP4 Time to Maximum (t_{Max})

The time to maximum reflects the delay between the contrast bolus arriving in the VOI from the referenced arterial ROI. It is calculated as the time to the maximum of the impulse residue function. Although this is similar to the time-to-peak (TTP), the TTP does not rely on the calculated impulse residue function.

2.7.11 CTP4 Permeability Surface Area Product (PS)

The permeability surface area product measures the leakage rate of contrast through the capillary walls into the interstitial space from the vascular space. It is computed from the IRF and is measured in ml per 100g of wet tissue per minute. (Assuming that there are no arterial-venous shunts.)

2.8 TexRAD Population

Of the 293 patients with non-small cell cancer (NSCLC) who had ^{18}F -FDG-PET/CT imaging described in Section 2.2, TexRAD features could not be extracted from three patients due to missing images, leaving 290 patients in the study.

2.9 TexRAD Image Analysis

Images were processed using TexRAD (Feedback Medical Ltd., <https://fbkmed.com/textrad-landing-2/>, London/Cambridge, UK), a proprietary clinical-research texture analysis software platform. Using the ^{18}F -FDG-PET and low-dose CT component together, a region of interest was drawn around the tumour at the most metabolically active slice on both the ^{18}F -FDG-PET images and the CT images. On the CT images, voxels within the region of interest were thresholded by Hounsfield Unit to exclude air ($< -50HU$) and exclude calcification and bone ($> 200HU$). PET and CT images were then passed through Laplacian of Gaussian spatial band-pass filters of varying radii as represented by the spatial scale factor (SSF), and first-order statistics and histogram metrics were calculated for the ROI on these filtered images. By varying the radius of the filter from 2, 3, 4, 5 to 6mm, finer (higher frequency) to coarser (lower frequency) textural features are highlighted. An SSF radius of 0 is used to designate no filtering, with statistics derived from the conventional image directly. All segmentation was performed by a radiologist with over 4 years' of experience with tumour

delineation. An initial 50 cases were discussed with the software vendor and the radiographer with over 10 years' of experience with tumour delineation using TexRAD.

The following biomarkers were extracted:

2.9.1 Mean intensity (mean)

The average brightness or intensity of the voxels in the ROI on the filtered/non-filtered image.

2.9.2 Standard Deviation (sd)

A measure of the variation in intensities from the mean intensity. If the intensities were plotted on frequency histogram, the standard deviation would be a kind of measurement of the width of the peak around the mean of that histogram. A higher standard deviation implies that there is a wider range of intensities and thus reflects heterogeneity.

2.9.3 Shannon Entropy (entropy)

TexRAD calculates the Shannon Entropy of the intensity histogram. This gives a measure of the randomness and inherent unpredictability of the intensity of a particular voxel in the ROI. A ROI that was homogeneous in intensity would have an entropy of 0, and entropy increases as the variability in intensity increases. It is thus another measure of heterogeneity, but whilst standard deviation is dependent on the magnitude of the difference to the mean, entropy is magnitude independent.

2.9.4 Mean of Positive Pixels (mpp)

This is the average intensity of positive intensity voxels in the ROI before and after filtering. In the unfiltered CT images this gives an impression of the average density of the solid component. In the filtered images it can be thought of providing a measure of the number of features in the ROI. This is because the Laplacian of Gaussian filter tends to convert edges in the unfiltered image to a positive and a negative component with magnitude related to how sharp that edge it, (the filter can be thought of as measuring the sum of the rate of change of the rate of change in the intensity in the unfiltered image). Thus the mean of positive pixels will measure the average "positive" edge in the ROI.

2.9.5 Histogram Skewness (skewness)

Skewness is a measure of the asymmetry of the intensity histogram about its mean. If one considers a normal distribution, the distribution is symmetrical about the mean, and thus a histogram that represents such a distribution or one that approaches a normal distribution will have a skewness that is zero or is close to zero. However, most distributions are non-normal and thus non-symmetrical about their means.

Distributions with a positive skew have a tail that is skewed to the right (and higher intensities), and negative to the left (and lower intensities.) In unimodal distributions, positive skew (tends to) translate to the mean being greater than the mode, with negative skew the mean being lower than the mode. Thus a positive skew reflects bright objects on a dark background and negative dark objects on a bright background. In plain CT images a positive skew could reflect sufficient denser tissue within fat, air or necrosis. In filtered images, the relationship and interpretation with the CT image is more difficult but a similar interpretation of the filtered images can be used.

2.9.6 Histogram Kurtosis (kurtosis)

In distribution terms kurtosis represents the weight of the tails of the distribution in comparison to the rest of the distribution. Often thought of as representing peakedness, higher kurtosis corresponds better to a greater extremity of outliers. Images with higher kurtosis will have increased tissue contrast whereas lower kurtosis will have reduced contrast.

2.10 Histology Population

Of the 293 patients with non-small cell cancer (NSCLC) who had ¹⁸F-FDG-PET/CT imaging described in Section 2.2, only patients who had surgery and immunohistochemistry staining were included. Results from mutation analysis, when successful, were also included.

2.11 Immunohistochemistry

Formalin-fixed paraffin-embedded (FFPE) tumour samples were obtained from the surgical specimens of those treatment-naïve patients who received primary surgery (i.e. without neoadjuvant therapies) after imaging was performed.

The FFPE specimens were cut at a thickness of 4 μm using Leica Microtome RM2235. Slides were stained on the Leica Bond Max Auto-stainer using Bond Polymer Refine Detection Kit. Epitopes for CA-IX were exposed by antigen retrieval solution ER1 (Leica) for 30 minutes. Epitopes for HIF-1 α and CD105 were exposed by antigen retrieval solution ER2 (Leica) for 20 minutes. Epitopes for VEGF were exposed by antigen retrieval solution ER2 for 20 minutes. GLUT1 did not require antigen retrieval.

Non-specific endogenous peroxidase activity was blocked by incubation with 3-4% hydrogen peroxide included in the kit.

Following this, antibodies were diluted in Leica Bond Diluent. Staining protocol of 15 minutes primary antibody, eight minutes post primary and eight minutes polymer was used for GLUT-1, VEGF, CD105 and CAIX. Staining protocol of 30 minutes primary antibody, 20 minutes post primary and 20 minutes polymer was used for HIF-1 α . Slides were incubated for 10 minutes in substrate chromogen, 3,3'-Diaminobenzidine tetrahydrochloride hydrate (DAB) and counterstained with haematoxylin for 2 minutes.

Afterwards, slides were removed from the Bond-max and rehydrated by immersion in increasing concentrations of ethanol (70%, 90% and 100%). Finally, slides were immersed in xylene three times prior to cover-slipping.

CD105 was used to quantify microvascular density. Under low magnification of CD-105 stained sections the four most vascular areas in each patient sample were identified.

In these areas, on a field of 0.62 mm^2 (200x on an Olympus microscope), vessels with a clearly defined lumen or with a well-defined linear vessel shape that was not a single endothelial cell were counted (186–188).

The presence and density of white cells was used to assess if there was inflammation present. Scores for other proteins were based on staining intensity and percentage of positively-stained cells. The intensity was score from 0–3 (no staining, weak, medium, strong), and the extent of staining was scored from 0–4 (<5%, 5–25%, 26–50%, 51–75%, >75%) (112).

2.12 Mutation Analysis

Additional FFPE samples were collected from the pathological specimens as above. DNA was extracted following the Standard Operating Procedure (SOP) for Qiagen QIAamp DNA FFPE Tissue kit. Quantification was performed using a Qubit dsDNA BR assay kit. Samples that had a concentration below the minimum concentration range for the Qubit dsDNA BR assay kit were run on a Qubit dsDNA HS assay kit.

Following quantification tests, samples were diluted in nuclease free water to 10ng.

Sequencing libraries were produced using a Fluidigm Access Array integrated fluidic circuit (IFC) chip. This allows multiplexing of up to 48 samples with 48 primer pairs into a single reaction.

Before samples were loaded on to the chip, a pre-amplification step was performed using a ROCHE fast-start high-fidelity polymerase chain reaction (PCR) kit. Primer mix was added to amplify the specific targets: this contained forward and reverse primer for each target at a concentration of 100pM.

Pre-amplification master mix was combined with 10ng of sample and run on a thermal cycler. Samples were then treated with Exosap-IT (Applied Biosystems) according to the manufacturer's SOP and protocol.

Samples were then loaded onto the Fluidigm IFC chip and processed. The samples were then tagged and barcoded using custom barcodes.

The barcoded samples were cleaned using AMPure XP beads (Beckman) and quantified with an Agilent High Sensitivity D1000 ScreenTape assay before being diluted to 100pM for sequencing.

Sequencing samples were loaded on to an Ion One Touch 2 Emulsion PCR machine as per manufacturer's SOPs and protocols. Quality control was performed using an Ion Sphere Quality Control kit to ensure that 10–30% of the spheres were loaded. Quality control results outside of this range required repeat loading.

Following sequencing, Binary sequencing Alignment Map and Index (BAM and BAI) files were downloaded from the sequencing server and loaded into the Integrative

Genomics Viewer (IGV) software. A Browser Extensible Data (BED) file was generated containing the location of the targeted regions that were sequenced. Mutations were manually called following assessment of sequencing depth, mutation frequency (with a minimum of 8%) and homopolymer association.

2.13 Statistics and Data Analysis

Patient demographic data was extracted and compared to look for statistical biases. ^{18}F -FDG-PET/CT, CT perfusion and TexRAD biomarkers were compared with Survival in univariate and multivariate Cox proportional hazards regressions using R 3.6.3 (189), and the survival package (190, 191). Graphs were created using ggplot2 package (192, p. 2). The tidyverse family of packages were used for general data analysis (193). Receiver operator curve analysis was performed using the survivalROC package (194). In chapter 6, statistical analysis was run on IBM SPSS Statistics Version 22.0 (Armonk, NY:IBM Corps) and R 3.6.3. Spearman's rank correlations and Mann Whitney tests were performed to assess for correlations between the immunohistochemical and mutation markers with imaging biomarkers. For each genetic mutation/wide-type subgroup (HER2, EGFR, KRAS, BRAF, any mutation); entropy_ct_ssf_2 & ^{18}F -FDG-PET SUV_{peak} , TBR_{lung} , SUV_{mean} , and SUV_{max} were compared with survival in univariate and multivariate Cox proportional hazards models to significantly stratify patients with good or poor prognosis. Difference in survival was assessed using the Log-rank test. Synergistic value of a combination of entropy_ct_ssf_2 and a ^{18}F -FDG uptake parameter was further evaluated as a prognostic marker within the different genetic subgroups.

2.14 List of total biomarkers studied

2.14.1 ^{18}F -FDG-PET quantitative biomarkers

- Tumour SUV_{max}
- Tumour SUV_{mean}
- Tumour SUV_{min}
- Normal Vessel SUV_{max}

- Normal Lung SUV_{max} , SUV_{mean} and SUV_{min}
- Tumour Target-to-Background Ratio (TBR_{lung})
- Tumour Dimensions

2.14.2 CT Perfusion quantitative biomarkers

- CTP4 Average
- CTP4 Base
- CTP4 Time to Peak (TTP)
- CTP4 Positive Enhancement Integral
- CTP4 Mean Slope of Increase
- CTP4 Blood Volume (BV)
- CTP4 Blood Flow (BF)
- CTP4 Mean Transit Time (MTT)
- CTP4 Time of Arrival (IRF(t_0))
- CTP4 Time to Maximum (t_{max})
- CTP4 Permeability Surface Area Product (PS)

2.14.3 TexRAD derived biomarkers

TexRAD analysis uses a combined filtration-histogram and statistical based approach. The PET and CT images are passed through Laplacian of Gaussian spatial band-pass filters of varying radii represented by the spatial scale factor (SSF) 0, 2, 3, 4, 5 or 6 and for both PET and CT images filtered each SSF the following first-order statistics are measured:

- Mean Intensity (mean)
- Standard Deviation (sd)
- Shannon Entropy (entropy)

- Mean of Positive Pixels (mpp)
- Histogram Skewness (skewness)
- Histogram Kurtosis (kurtosis)

Thus the list of TexRAD biomarkers considered is a cross product of the image type (PET or CT), the SSF, and a first-order statistic as listed above, e.g. entropy_ct_ssf_2.

3 ¹⁸F-FDG-PET Quantitative Biomarkers in Lung Cancer

3.1 Abstract

3.1.1 Purpose

To examine the correspondence between ¹⁸F-FDG-PET biomarkers and survival in non-small cell lung cancer (NSCLC).

3.1.2 Methods

484 patients with suspected lung cancer were recruited to the study. Only patients who had ¹⁸F-FDG-PET/CTs and were diagnosed with NSCLC were included.

Histology and Stage were noted and ¹⁸F-FDG-PET/CT biomarkers were analysed.

Kaplan-Meier and Cox proportional hazard survival analysis was performed. Analysis was performed using R.

3.1.3 Findings

3.1.3.1 Patient Demographics

Of the 484 patients in the study, 475 had ¹⁸F-FDG-PET/CTs. Of these 293 were determined to have NSCLC and 133 were determined to be benign.

Of these 293 patients 162 were Male and 131 were Female.

3.1.3.2 Age and Surgical Status

The median survival of the NSCLC patients was 901 days (731–1082 days 95% CI).

Survival was significantly (albeit weakly) negatively correlated with age at enrolment (HR 1.03, 1.01–1.04 95% CI, p=0.002).

Survival is strongly positively correlated with surgical status (HR 0.22, 0.16–0.31 95% CI, p<0.001.) Surgical status has a stronger correlation than age at enrolment in multivariate Cox regression where it remains statistically significant, unlike age at enrolment.

3.1.3.3 Disease Stage

Increasing disease stage was strongly negatively correlated with survival ($p < 0.001$) and multivariate Cox regression combining stage, age at enrolment and surgical status is statistically significant.

3.1.3.4 SUV_{max}

The mean SUV_{max} was 12.4 ± 7.2 . SUV_{max} was weakly negatively correlated with survival, (HR 1.03, 1.01–1.04 95% CI, $p = 0.002$).

In multivariate Cox regression analysis SUV_{max} appears independent of age of enrolment but not surgery or stage.

ROC analysis revealed an AUC of 67% revealing that this is poor predictor, however a cut-off of $SUV_{max} > 7.6$ derived from Youden's index is statistically significant (HR 1.88, 1.36–2.56 95% CI, $p < 0.001$).

This cut-off remains statistically significant in multivariate analysis with surgical status but not with stage.

3.1.3.5 TBR_{lung}

The mean TBR_{lung} was 46.5 ± 33.8 . Lower TBR_{lung} was also associated with survival (HR 1.01, 1.00–1.01 95% CI, $p = 0.001$). In multivariate Cox regression it remains statistically significant with age at enrolment but is not statistically significant when combined with surgery or stage.

ROC analysis revealed an AUC of 69% revealing that it is a poor predictor, however, a cut-off of $TBR_{lung} > 26.2$ is a statistically significant predictor of survival (HR 0.46, 0.33–0.63 95% CI, $p < 0.001$) and in multivariate Cox regression remains statistically significant when combined with surgery but not stage.

3.1.4 Conclusion

Both lower SUV_{max} and TBR_{lung} are statistically associated with survival but neither are independent of stage. Lower TBR_{lung} is more strongly associated with survival than SUV_{max} .

3.2 Introduction

Lung cancer is the leading cause of cancer-related death worldwide (6), and whilst there has been substantial improvement in one-year survival of non-small cell lung cancer from 16% in 1971–1972 to 32% in 2010–2011, long-term survival remains poor (2). Prognostication of survival is most often performed using staging with the Tumour-Node-Metastasis (TNM) system (4), however these stages are somewhat coarse and survival within these groups is heterogeneous. Curative surgery is often limited to the early stages of lung cancer, with chemotherapy and radiotherapy used in more advanced stages.

Although contrast-enhanced CT, MRI and EBUS play a significant role in the diagnosis, staging and restaging of lung cancer, the main modality used for the staging and restaging of non-small cell lung cancer is now ^{18}F -fluoro-2-deoxy-D-glucose positron emission tomography/computed tomography (^{18}F -FDG-PET/CT). ^{18}F -FDG-PET/CT provides superior assessment of nodal and extra-thoracic metastasis to that of CT and the helps guide EBUS targetting (195).

^{18}F -FDG-PET provides a measure of the glucose metabolism as it is actively transported in to cells through glucose transporters (GLUTs), and then phosphorylated by hexokinases to ^{18}F -FDG-6-phosphate. ^{18}F -FDG-6-phosphate will then accumulate in cells as it cannot be further metabolised until the ^{18}F decays into ^{18}O through emission of a positron or it is dephosphorylated by phosphatases (56, 60, 61). Metabolically active cells, often cancerous cells, will therefore accumulate ^{18}F -FDG. Although full metabolism of the glucose is an oxygen dependent process, the initial phosphorylation of glucose is not, and hypoxia induces cells to increase expression of GLUTs and thus uptake and accumulation of ^{18}F -FDG and ^{18}F -FDG-6-phosphate. In this way, ^{18}F -FDG uptake is increased in hypoxic and metabolically active cells (56, 62), however it is difficult to differentiate between the aerobic and anaerobic induced uptake, and tumours with low metabolic rates or low glucose uptake, e.g. mucinous adenocarcinomas, will have falsely reassuring low ^{18}F -FDG avidity (56).

The coarseness of the staging system coupled with the heterogeneous uptake of ^{18}F -FDG raises the question of whether semi-quantitative measures such as SUV_{max} and TBR_{lung} can be used to provide additional survival prognostication over that of the staging. The aim of this study is therefore to assess if there is a statistically significant relationship between ^{18}F -FDG biomarkers and, survival and histological subtype.

3.3 Materials and Methods

3.3.1 Patient Population

The population of patients is as described in detail in Section 2.2. There were a total of 293 patients with non-small cell cancer (NSCLC).

3.3.2 ^{18}F -FDG-PET/CT Imaging Protocol

The imaging protocol is described in detail in Section 2.3.

3.3.3 ^{18}F -FDG-PET/CT Image Analysis

The analysis protocol is described in detail in Section 2.4.

3.3.4 Statistics and Data Analysis

Statistical and data analysis is described in detail in Section 2.13.

3.4 Findings

3.4.1 Patient Demographics

Of the 484 patients, 475 patients had ^{18}F -FDG-PET/CT imaging and a total of 293 patients were determined to have NSCLC, (133 were determined to benign.)

Of these 293 patients 162 were male and 131 were female. The median age at enrolment was 69 years (range 63–75 years). 108 (37%) of these patients were Stage I, 53 (18%) Stage II, 92 (31%) Stage III and 40 (14%) Stage IV. There was no statistically significant difference between gender and age at enrolment, SUV_{max} , or TBR_{lung} . (See Table 1.)

3.4.2 Age and Surgical Status

The median survival of the NSCLC patients was 901 days (731–1082 days 95% CI). One-year survival was 74.9% and five-year survival was 34.2%. Survival was significantly (albeit weakly) negatively correlated with age at enrolment (HR 1.03, 1.01–1.04 95% CI, $p=0.002$).

Survival is strongly positively correlated with surgical status (HR 0.22, 0.16–0.31 95% CI, $p<0.001$.) Surgical status has a stronger correlation than age at enrolment in multivariate cox regression where it remains statistically significant unlike age at enrolment. (See Tables 2 and 3.)

When surgical status is compared with age at enrolment, stage, SUV_{max} and TBR_{lung} we can see that there is a statistically significant difference with all four factors in keeping with the decision to operate being a composite marker representing the clinical gestalt of patient fitness. (See Table 4.)

3.4.3 Disease Stage

Increasing disease stage was strongly negatively correlated with survival ($p<0.001$) and multivariate Cox regression combining stage, age at enrolment and surgical status is statistically significant. (See Table 5 and Table 6.)

3.4.4 SUV_{max}

The mean SUV_{max} was 12.4 +/- 7.2. Lower SUV_{max} was significantly but weakly correlated with survival, (HR 1.03, 1.01–1.04 95% CI, p=0.002). (See Table 7.) In multivariate regression analysis this correlation was stronger than that of Age of enrolment but not Surgery or Disease Stage. (See Table 8.)

Receiver operating characteristic curve analysis suggests that SUV_{max} has a poor accuracy for predicting survival with an area under the curve (AUC) of 66%, however a cut-value of SUV 7.6 derived from Youden's index is statistically significant (HR 1.88, 1.36–2.56 95% CI, p < 0.001) and, whilst this only has a specificity of 42.4% it has quite high sensitivity at 83.4%. (See Figure 1.) This cut-off is, however, only statistically significant when restricted to patients who had surgery (See Table 10 and Figure 2) and it is not independent of stage. (See Table 11.)

Given the significant survival differences between those treated with surgery it's worth considering SUV_{max} ROC analysis within the two sub-groups separately.

3.4.5 SUV_{max} in Non-Surgical Patients

In non-surgical patients ROC analysis suggests that SUV_{max} 8.9 represents the best cut-value for maximizing accuracy; however, the AUC is only 51% and the cut-value results in a sensitivity of 71.3% and specificity of 19.4%. Unsurprisingly, this does not produce a statistically significant difference in survival.

3.4.6 SUV_{max} in Surgical Patients

For surgical patients, ROC analysis suggests that SUV_{max} 7.4 represents the best cut-value for maximizing accuracy. This cut-off has a sensitivity of 72.8% and specificity of 50.0% at median survival. This is statistically significantly associated with survival but is not independent of stage.

3.4.7 SUV_{mean}

The mean SUV_{mean} was 7.8 +/- 4.7. Lower SUV_{mean} was significantly but weakly correlated with survival, (HR 1.04, 1.01–1.07 95% CI, p=0.004). In multivariate regression analysis this correlation was stronger than that of age of enrolment but not surgery or disease stage. ROC analysis revealed that SUV_{mean} 10.3 represents the best

cut-value for maximizing accuracy however the AUC is only 65% which has a sensitivity of only 41.7% and specificity of 81.8%. This is a statistically significant predictor of survival (HR 0.66, 0.49–0.88, $p=0.005$) but does not remain statistically significant in multivariate Cox regression with either surgical status or stage.

3.4.8 TBR_{lung}

The mean TBR_{lung} was 46.5 ± 33.8 . Lower TBR_{lung} was also weakly associated with survival (HR 1.01, 1.00–1.01 95% CI, $p=0.001$). (Table 12.) In multivariate Cox regression it remains statistically significant with age at enrolment but is not statistically significant when combined with surgery or stage. (Table 13)

ROC analysis revealed an AUC of 66% revealing that it is a poor predictor, (Figure 3) however, a cut-off of $TBR \leq 26.2$ is a statistically significant predictor of survival (HR 0.46, 0.33–0.63 95% CI, $p < 0.001$) and in multivariate Cox regression remains statistically significant when combined with surgery but not stage. (Table 15 and

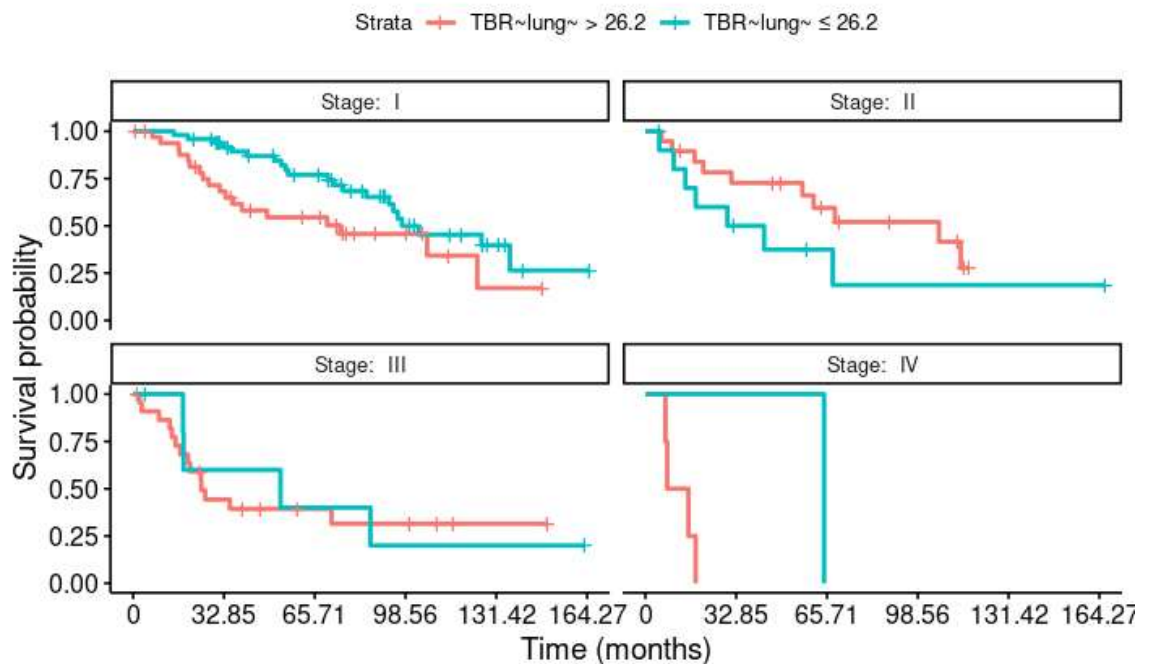


Figure 4.) When restricted to Stage I patients the cut-off remains a statistically significant prognosticator and is a stronger predictor than largest axial tumour size. Most interestingly the predicted cut-off appears to work in the opposite direction for Stage II patients in contrast to that of Stage I patients.

3.5 Discussion

This prospective study has demonstrated that ^{18}F -FDG SUV_{max} , ^{18}F -FDG SUV_{mean} and ^{18}F -FDG TBR_{lung} are predictive for survival, but they do not provide significant additional prognostication power over that of staging. A partition of $\text{TBR}_{\text{lung}} \leq 26.2$ does provide significant additional prognostication power over pure surgical status and does provide additional prognostication power in Stage I disease, but is not statistically significant for higher stage disease.

The poor additional prognostication for these measures in higher stage disease stands in contrast to the findings of other studies (69–72, 74–76, 78, 80, 82, 83, 94–96, 104, 196). The finding that $\text{SUV}_{\text{max}} \leq 7.4$ is a statistically significant predictor of survival for surgical patients does replicate the findings of other studies (70–72, 77, 82, 94), however it is worth noting that there has been no consistently recognised cut-off limit, with some of these papers suggesting various cut offs for SUV_{max} ranging from 5–7 or into quintile and quartile groups. Further, the biases inherent in our patient population due to recruitment factors may be a reason for the poor ability of SUV_{max} to predict survival in higher stages. Our study population is heavily weighted toward those with lower disease stage and likely operable tumours, with a bias towards surgically fit patients as compared to the normal population of the lung cancers. These biases mean that the survival of our population of Stage II–IV patients is likely to be artificially large — especially for the larger tumours. (For example, our one-year survival for all our patients and all Stage III patients was 74.9% and 63.4% respectively whereas the 2013–2017 age standardised one-year survival in the UK is only 40.6% and 48.1% respectively (3)). It may also artificially increase the difference in survival between those treated with Surgery versus those not, as non-surgical treatment may reflect worse non-tumoural prognostic factors, e.g. heart disease, fibrosis, and emphysema.

The lack of the inclusion of SUV_{max} in the grading guidelines for the 8th Edition of the TNM staging system does somewhat suggest that although SUV_{max} and other markers of glycolysis play a significant role in the decisions to stage tumours, their role in prognostication remains unproven.

TBR_{lung} , a synthetic biomarker combining tumour SUV_{max} and background lung SUV_{min} , provides a measurement which is highly correlated with the rate of transfer constant (K_i) that can be derived from kinetic analysis (197–199). This marker has been shown to be highly prognostic in diffuse lung disease (48–51) and demonstrates a sensitive marker for disease progression in COVID-19 (see Chapter 7), but pathology in cancer is very different from that in these disease. Our findings regarding the discovery of the significant cut-off for TBR_{lung} is the first time TBR_{lung} has been applied to lung cancer. In particular, the prognostic benefit of $TBR_{lung} \leq 26.2$ in Stage I disease is stronger than that of the benefit of sub-staging in Stage I disease. Why the TBR_{lung} should be such a strong predictor is uncertain, though it may be helping to highlight the inappropriately avid smaller lesions that are of more concern and downplay mildly avid slightly larger lesions.

3.6 Conclusion

Both lower SUV_{max} and TBR_{lung} are statistically associated with survival but neither are independent of stage. Lower TBR_{lung} is more strongly associated with survival than SUV_{max} .

3.7 Tables

Gender	Overall, N = 293	Female, N = 131	Male, N = 162	p-value ¹
Age at Enrolment				0.4
N	293.0	131.0	162.0	
Median (IQR)	69.0 (63.0, 75.0)	68.0 (62.0, 74.0)	70.5 (63.0, 75.0)	
Range	44.0, 96.0	44.0, 90.0	48.0, 96.0	
Surgery	148 (51%)	68 (52%)	80 (49%)	0.7
Radiological Stage				0.6
I	108 (37%)	53 (40%)	55 (34%)	
II	53 (18%)	22 (17%)	31 (19%)	
III	92 (31%)	41 (31%)	51 (31%)	
IV	40 (14%)	15 (11%)	25 (15%)	
SUV_{max}				0.4
Median (IQR)	11.8 (6.7, 17.2)	11.5 (5.6, 17.2)	12.0 (7.0, 17.4)	
Range	0.5, 40.0	0.5, 33.6	0.8, 40.0	
TBR_{lung}				0.026
Median (IQR)	41.3 (22.3, 59.0)	35.2 (17.7, 54.8)	43.9 (24.7, 62.5)	
Range	1.6, 210.2	1.6, 173.0	2.7, 210.2	

¹Wilcoxon rank sum test; Pearson's Chi-squared test

Table 1: Patient demographics as compared to gender

Characteristic	HR	95% CI	p-value
Surgery			
No	—	—	
Yes	0.22	0.16, 0.31	<0.001

Table 2: Univariate Cox regression of survival versus surgical status

Characteristic	HR	95% CI	p-value
Age at Enrolment	1.01	1.00, 1.03	0.093
Surgery			
No	—	—	
Yes	0.23	0.17, 0.32	<0.001

Table 3: Multivariate Cox regression of survival versus surgical status and age at enrolment

Surgical Status	Overall, N = 293	No, N = 145	Yes, N = 148	p-value ²
Age at Enrolment				0.006
Median (IQR)	69.0 (63.0, 75.0)	71.0 (64.0, 77.0)	67.0 (62.0, 73.2)	
Range	44.0, 96.0	44.0, 96.0	48.0, 90.0	
Gender				0.7
F	131 (45%)	63 (43%)	68 (46%)	
M	162 (55%)	82 (57%)	80 (54%)	
Radiological Stage				<0.001
I	108 (37%)	24 (17%)	84 (57%)	
II	53 (18%)	23 (16%)	30 (20%)	
III	92 (31%)	63 (43%)	29 (20%)	
IV	40 (14%)	35 (24%)	5 (3.4%)	
SUV_{max}				<0.001
Median (IQR)	11.8 (6.7, 17.2)	13.9 (9.3, 18.3)	10.1 (5.2, 14.4)	
Range	0.5, 40.0	0.5, 40.0	0.5, 37.9	
TBR_{lung}				<0.001
Median (IQR)	41.3 (22.3, 59.0)	47.4 (32.0, 70.9)	32.2 (16.5, 52.7)	
Range	1.6, 210.2	2.5, 210.2	1.6, 171.7	

¹Wilcoxon rank sum test; Pearson's Chi-squared test

Table 4: Biomarkers as compared to surgical status

Radiological Stage	Overall, N = 293 ¹	Stage I, N = 108	Stage II, N = 53	Stage III, N = 92	Stage IV, N = 40	p-value
Age at Enrolment						0.089
Median (IQR)	69.0 (63.0, 75.0)	69.0 (63.0, 76.0)	69.0 (63.0, 76.0)	71.0 (64.0, 74.2)	66.0 (57.8, 72.0)	
Range	44.0, 96.0	49.0, 96.0	52.0, 90.0	44.0, 88.0	47.0, 80.0	
Gender						0.6
F	131 (45%)	53 (49%)	22 (42%)	41 (45%)	15 (38%)	
M	162 (55%)	55 (51%)	31 (58%)	51 (55%)	25 (62%)	
Surgery	148 (51%)	84 (78%)	30 (57%)	29 (32%)	5 (12%)	<0.001
SUV_{max}						<0.001
Median (IQR)	11.8 (6.7, 17.2)	7.1 (4.0, 11.7)	13.1 (6.5, 17.2)	14.6 (11.2, 18.7)	13.4 (10.5, 19.3)	
Range	0.5, 40.0	0.5, 37.9	2.9, 26.2	3.4, 33.6	1.9, 40.0	
TBR_{lung}						<0.001
Median (IQR)	41.3 (22.3, 59.0)	24.2 (13.4, 45.7)	38.3 (20.8, 57.5)	50.4 (37.7, 71.0)	49.4 (36.0, 73.4)	
Range	1.6, 210.2	1.6, 171.7	8.5, 115.0	11.0, 173.0	9.5, 210.2	

Table 5: Biomarkers as compared to radiological disease stage

Characteristic	HR	95% CI	p-value
Radiological Stage			
I	—	—	
II	1.86	1.22, 2.82	0.004
III	2.61	1.78, 3.82	<0.001
IV	3.97	2.47, 6.38	<0.001
Age at Enrolment	1.03	1.01, 1.04	0.005
Surgery			
No	—	—	
Yes	0.35	0.25, 0.50	<0.001

Table 6: Multivariate Cox-regression of survival with radiological stage, age and surgical status

Characteristic	HR	95% CI	p-value
SUV_{max}	1.03	1.01, 1.04	0.002

Table 7: Univariate Cox regression of survival versus SUV_{max}

Characteristic	HR	95% CI	p-value
SUV_{max}	1.02	1.00, 1.03	0.11
Age at Enrolment	1.02	1.00, 1.03	0.061
Surgery			
No	—	—	
Yes	0.24	0.18, 0.33	<0.001

Table 8: Multivariate Cox regression of survival versus SUV_{max}, age at enrolment and surgical status

Characteristic	HR	95% CI	p-value
SUV_{max}			
SUV _{max} > 7.6	—	—	
SUV _{max} ≤ 7.6	0.53	0.39, 0.73	<0.001

Table 9: Univariate Cox regression of Survival versus SUV_{max} > 7.6

Characteristic	HR	95% CI	p-value
Surgery			
No	—	—	
Yes	0.24	0.17, 0.33	<0.001
SUV_{max}			
SUV _{max} > 7.6	—	—	
SUV _{max} ≤ 7.6	0.71	0.51, 0.98	0.037

Table 10: Multivariate Cox regression of survival versus SUV_{max} > 7.6 and surgical status

Characteristic	HR	95% CI	p-value
SUV_{max}			
SUV _{max} > 7.6	—	—	
SUV _{max} ≤ 7.6	1.04	0.71, 1.52	0.8
Radiological Stage			
I	—	—	
II	2.19	1.41, 3.39	<0.001
III	3.50	2.31, 5.32	<0.001
IV	6.41	4.01, 10.2	<0.001

Table 11: Multivariate Cox regression of survival versus SUV_{max} > 7.6 and radiological stage

Characteristic	HR	95% CI	p-value
TBR_{lung}	1.01	1.00, 1.01	0.001

Table 12: Univariate Cox regression of survival versus TBR_{lung}

Characteristic	HR	95% CI	p-value
TBR_{lung}	1.00	1.00, 1.01	0.093
Surgery			
No	—	—	
Yes	0.24	0.18, 0.33	<0.001
Age at Enrolment	1.02	1.00, 1.03	0.069

Table 13: Multivariate Cox regression of survival versus TBR_{lung}, age at enrolment and surgical status

Characteristic	HR	95% CI	p-value
TBR_{lung}			
TBR _{lung} > 26.2	—	—	
TBR _{lung} ≤ 26.2	0.46	0.33, 0.63	<0.001

Table 14: Univariate Cox regression of survival versus TBR_{lung} > 26.2

Characteristic	HR	95% CI	p-value
Surgery			
No	—	—	
Yes	0.25	0.18, 0.34	<0.001
TBR_{lung}			
TBR _{lung} > 26.2	—	—	
TBR _{lung} ≤ 26.2	0.63	0.45, 0.88	0.007

Table 15: Multivariate Cox regression of survival versus TBR_{lung} > 26.2 and surgical status

3.8 Figures

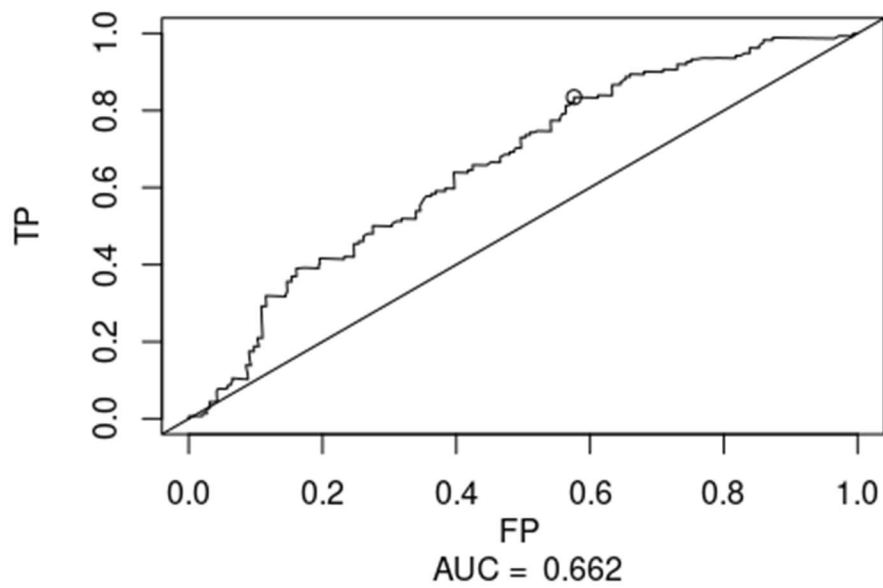


Figure 1: Receiver operating characteristic curve for survival vs. $SUV_{max} > 7.6$

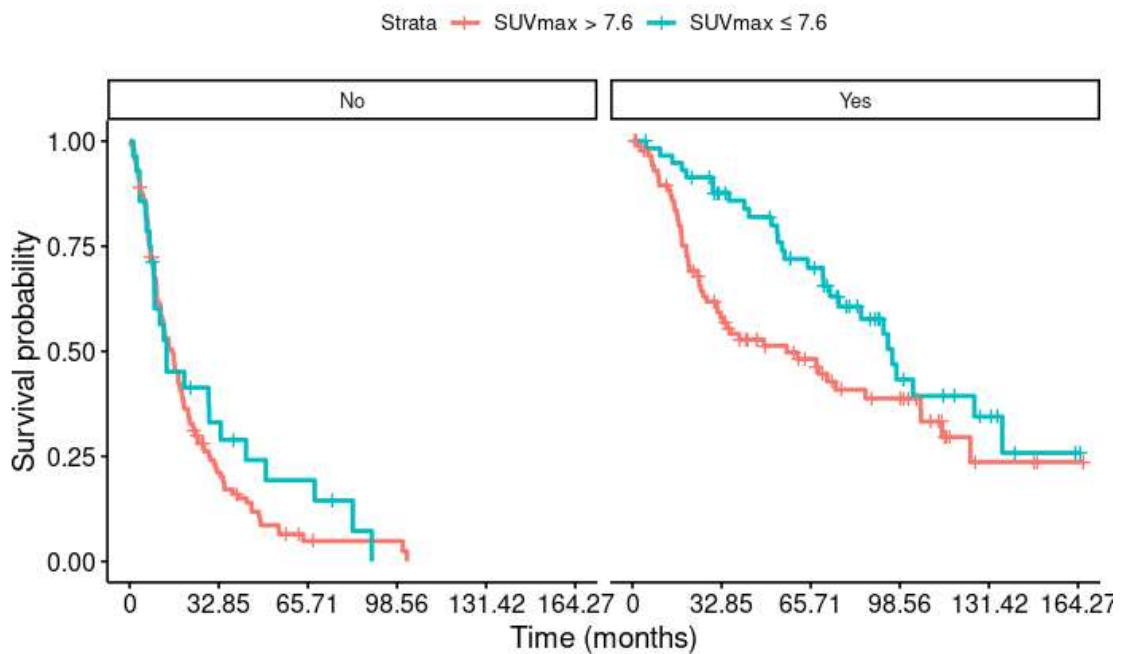


Figure 2: Kaplan-Meier Survival Curves stratified by $SUV_{max} > 7.6$ faceted by surgical status

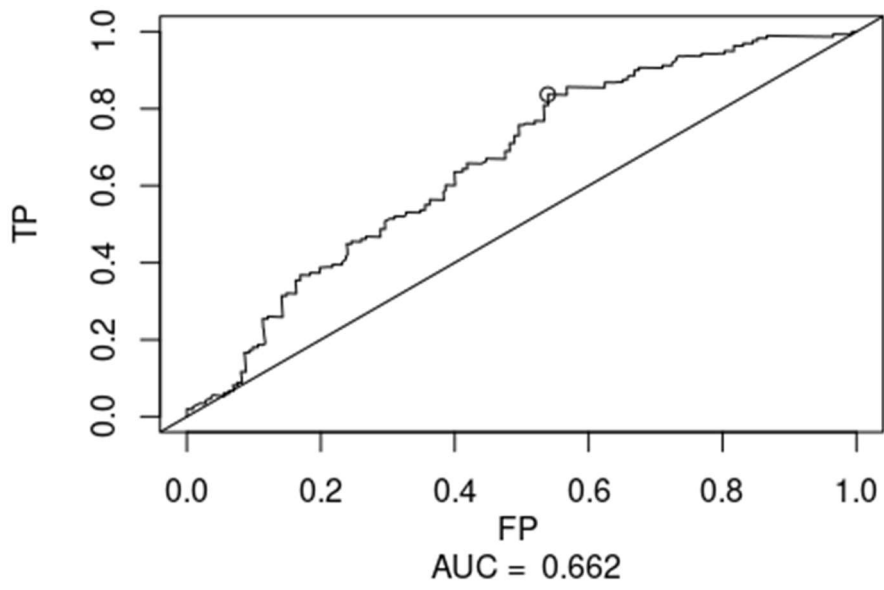


Figure 3: Receiver operating characteristic curve for survival vs. $TBR_{lung} > 26.2$

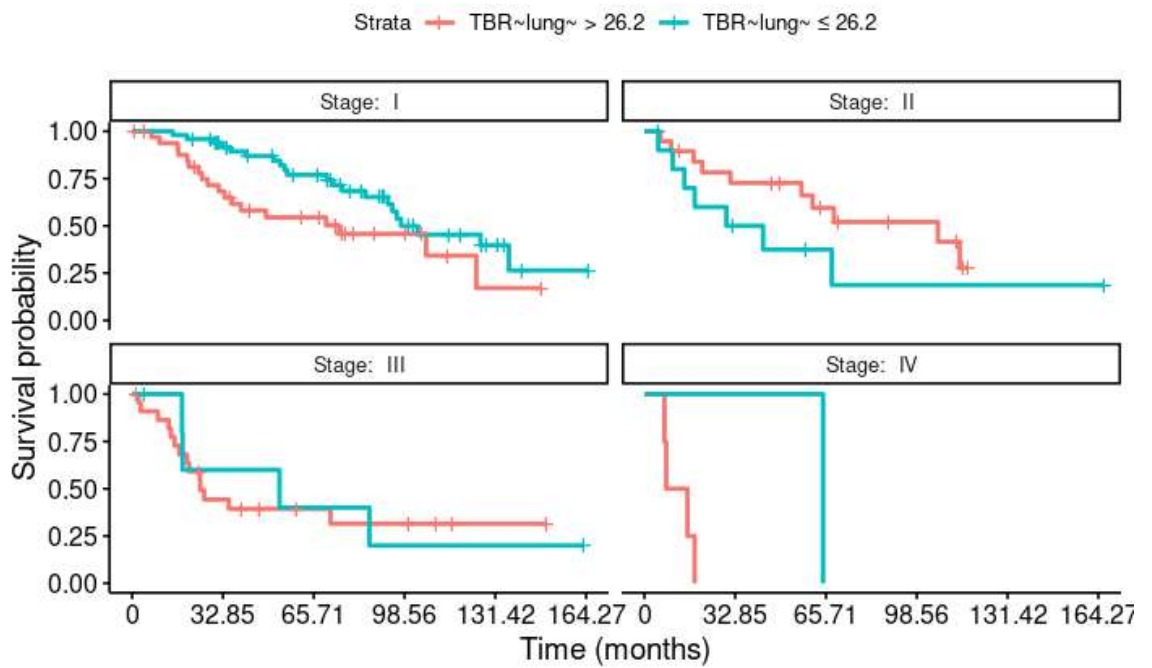


Figure 4: Kaplan-Meier Survival Curves stratified by $TBR_{lung} > 26.2$ faceted by radiological stage

4 CT Perfusion in Lung Cancer

4.1 Abstract

4.1.1 Purpose

To examine the correspondence between CT perfusion (CTP) & ^{18}F -FDG-PET/CT biomarkers and survival in non-small cell lung cancer (NSCLC).

4.1.2 Methods

484 patients with suspected lung cancer were recruited to the study. Only patients who had both a ^{18}F -FDG-PET/CT study and a CT Perfusion study, and who were subsequently diagnosed with NSCLC, were included.

Histology and stage were noted and ^{18}F -FDG-PET/CT and CT perfusion biomarkers were analysed using Advantage Workstation (ADW) for Diagnostic Imaging (GE Healthcare) CT Perfusion 4D (CTP4).

Kaplan-Meier and Cox proportional hazard survival analysis was performed. Analysis was performed using R.

4.1.3 Findings

4.1.3.1 Patient Demographics

Of the 484 patients in the study, 475 had ^{18}F -FDG-PET/CTs. Of these 293 were determined to have NSCLC and 133 were determined to be benign. Of the NSCLC patients, 162 patients had CT perfusion (CTP) analysis performed.

Of these 162 patients, 95 were male and 67 were female, with median age 71 years (range 44–96 years). 56 (35%) of these patients were Stage I, 29 (18%) Stage II, 56 (35%) Stage III and 21 (13%) Stage IV. The median survival of the patients was 903 days (721–1198 days 95% CI). The mean SUV_{max} was 12.4 +/- 6.8.

4.1.3.2 CT Perfusion and Survival

Correlation analysis demonstrates that the 11 CT Perfusion biomarkers are highly correlated with each other, but that they have poor individual correlation with ^{18}F -FDG biomarkers, surgical status, stage, and raw survival time, and indicates that there is no

statistically significant survival relationship between any of these with survival, nor is there any linear combination of these which demonstrates a statistically significant relationship with survival.

However, when considering only the patients who did not have surgery, there is a statistically significant relationship between mean transit time and survival ($p=0.013$).

4.1.3.3 CT Perfusion and SUV_{max}

A statistically significant linear model predicting SUV_{max} is possible when combining time-to-peak, blood volume and CTP4 base. ($p=0.005$, $p<0.001$ and $p<0.001$ respectively). This linear model has an AIC of 1050 but when looking at the residuals there is a linear relationship suggesting that this is still incomplete.

The results of this prediction are statistically significantly correlated with survival, however, the p-value is larger than that obtained from using SUV_{max} alone.

4.1.3.4 CT Perfusion and Surgery

A statistically significant multivariate logistic model predicting surgery is possible but has overall accuracy of only 66%.

The results of this prediction are statistically significantly correlated with survival ($p=0.03$) but are not independent of SUV_{max} or stage.

4.1.3.5 CT Perfusion and Nodal Status

A statistically significant multivariate logistic model of CTP4 base and positive enhancement integral predicts nodal status with a 72% accuracy. The prediction score is significantly correlated with survival ($p=0.03$). This prediction is not independent of SUV_{max} or surgery but is independent of stage; however, this is not as strong as using nodal status directly and it is notable that the full dataset does not demonstrate survival benefit.

4.1.4 Conclusion

There is no definite clear correlation with CT perfusion biomarkers and survival, and there is no clear added benefit to CT perfusion over that ^{18}F -FDG based staging and surgery.

4.2 Introduction

As discussed in Section 3.2, lung cancer is the leading cause of cancer-related death worldwide (6), and long-term survival remains poor (2). Prognostication of survival using staging with the Tumour-Node-Metastasis (TNM) system (4) is non-ideal as stages are somewhat coarse and survival within these groups is heterogeneous.

Amongst the key factors of tumour growth, evolution and metastatic spread, necrosis, angiogenesis and the response to hypoxia are vital (62). Whilst angiogenesis can be assessed histopathologically through assessment of the microvascular density and immunohistochemistry markers such as hypoxia-inducible factor (HIF) (62, 135), non-invasive *in vivo* assessment of tumour vascularity with CT-perfusion (CTP) has the potential to predict response to anti-angiogenesis therapy and thence survival independently, although results so far have been mixed (140, 142, 145, 147, 151).

^{18}F -FDG-PET/CT, although, able to assess response to therapy and stage patients, cannot provide a direct measure of tumour perfusion, however, the relationship between CT perfusion biomarkers, tumour size, stage, location, histological subtype, ^{18}F -FDG biomarkers and the immunohistochemistry markers is unclear. Whether CTP can provide additional survival prognostication over that of ^{18}F -FDG-PET/CT and the stage derived from it is also unknown. The aim of this study is therefore to assess if there is a statistically significant relationship between CT perfusion biomarkers and survival and histological subtype. Additionally, previous studies have shown that CT perfusion biomarkers can predict survival in non-surgical higher stage disease (142): we will also review if our study can replicate these findings.

4.3 Materials and Methods

4.3.1 Patient Population

The population of patients is as described in detail in Section 2.2 and Section 2.5. There were a total of 162 patients with non-small cell cancer (NSCLC) who had CT perfusion imaging and ^{18}F -FDG-PET/CT imaging.

4.3.2 ^{18}F -FDG-PET/CT Imaging Protocol

The ^{18}F -FDG-PET/CT imaging protocol is described in detail in Section 2.3.

4.3.3 CT Perfusion Imaging Protocol

The CT perfusion imaging protocol is described in detail in Section 2.6.

4.3.4 ^{18}F -FDG-PET/CT Image Analysis

The ^{18}F -FDG-PET/CT image analysis protocol is described in detail in Section 2.4.

4.3.5 CT Perfusion Image Analysis

The CT perfusion image analysis protocol is described in detail in Section 2.7.

4.3.6 Statistics and Data Analysis

Statistical and data analysis is described in detail in Section 2.13.

4.4 Findings

4.4.1 Patient Demographics

Of the 484 patients in the study, 475 had ^{18}F -FDG-PET/CTs. Of these 293 were determined to have NSCLC and 133 were determined to be benign. Of the NSCLC patients 162 patients had CT Perfusion (CTP) analysis performed.

Of these 162 patients 95 were Male and 67 were Female with median age at enrolment of 71 years (range 44–96 years). 56 (35%) of these patients were Stage I, 29 (18%) Stage II, 56 (35%) Stage III and 21 (13%) Stage IV. There was no statistically significant difference between gender and Age at Enrolment, Stage, SUV_{max} , or the CT Perfusion measures. (See Table 16.)

4.4.2 Age and Surgical Status

The median survival of the NSCLC CTP patients was 903 days (721–1214 days 95% CI). This is slightly longer than the full PET dataset but is not statistically significantly different. Survival remained significantly albeit weakly negatively correlated with age at enrolment (HR=1.03 (1.00–1.05 95% CI), $p=0.031$) and strongly positively correlated with surgical status (HR=0.27 (0.17–0.41 95 %CI), $p<0.001$.)

However, in multivariate Cox regression analysis these correlations were not independent and surgical status has a stronger correlation.

4.4.3 Disease Stage

Increasing disease was strongly negatively correlated with survival with increasing hazard ratio as stage increased and is independent of surgery in multivariate analysis, (See Table 6 & Table 18.)

4.4.4 SUV_{max}

The mean SUV_{max} was 12.4 +/- 6.8. This is similar to the main dataset. Lower SUV_{max} was significantly correlated with survival, (HR=1.02 (1.02–1.08 95%CI) $p<0.001$). In multivariate analysis this correlation was stronger than that of age at enrolment but was not independent or stronger than surgical status or disease stage.

Receiver operating characteristic curve analysis suggests that SUV_{max} has a fair accuracy for predicting survival with an area under the curve of 71%, with a cut-value of $SUV_{11.5}$ maximizing accuracy but only has a specificity of 72% and a sensitivity of 65%. (See Figure 5.) This cut-off is, however, only statistically significant when restricted to patients who had surgery (See Figure 6) and it is not independent of stage.

4.4.5 Correlation Between Non-Deconvolution and Deconvolution Dependent Biomarkers

The deconvolution dependent biomarkers of blood flow, blood volume and permeability surface area product are well correlated with the non-deconvolution dependent biomarkers: positive enhancement integral and mean slope of increase. The remaining deconvolution dependent biomarkers — mean transit time, $IRF(t_0)$, and t_{max} — are very well correlated with each other but do not demonstrate good correlation with other non-deconvolution dependent biomarkers. (See Figure 7.)

4.4.6 CT Perfusion Measures Against Survival

The values of the CT perfusion measures are highly correlated with each other but appear poorly correlated with survival. (See Figure 7.)

Univariate survival analysis thus revealed no statistically significant linear relationship between any of these characteristics and survival. (See Table 19.)

Multivariate analysis was also unable to find a statistically significant model against survival.

When patients were studied in subgroups by stage, CTP4 average was borderline statistically significant (HR=0.98, 0.96–1.00 95% CI, $p=0.048$). Subgroup analysis by T-stage was unable to find a statistically significant linear relationship.

4.4.7 Can CT Perfusion Predict SUV_{max} ?

Previous studies have suggested that SUV_{max} can be predicted using CT perfusion. A multivariate linear regression model was possible combining CTP4 time to peak, blood volume and base (p -values 0.005, <0.001 and <0.001 respectively.) However, there was poor prediction of higher SUV_{max} with this model showing significant heteroscedasticity. When the predicted SUV_{max} was used to predict survival there was a

statistically significant correlation, but this was weaker than that of SUV_{max} alone and was not independent of surgery or stage.

4.4.8 Can CT Perfusion Predict Surgery?

Similarly a statistically significant multivariate model predicting surgery was possible. However, this model required 5 variables combining CTP4 base, blood volume, blood flow, mean transit time and t_{Max}, (AIC of 201.75) and although its values were also statistically significantly correlated with survival (p=0.03) it was not independent of SUV_{max} or stage. The overall accuracy was poor at only 66%.

4.4.9 Can CT Perfusion Predict Nodal Status?

A statistically significant multivariate logistic model of CTP4 base and positive enhancement integral predicts nodal status with a 72% accuracy.

The prediction score is significantly correlated with survival with (p=0.03) and is independent of surgery and stage; however it has a poor AUC on ROC analysis of only 64%, and the cut-value behaves poorly in subgroup analysis.

4.4.10 Can CT Perfusion Predict Metastatic Status?

No statistically significant univariate or multivariate logistic model of CT perfusion biomarkers was able to predict metastases within our dataset.

4.4.11 Can CT Perfusion Predict Survival in Non-Surgical Higher Stage Disease Treated with Chemotherapy?

Of the 162 NSCLC patients that had CT Perfusion (CTP) analysis performed, 42 patients (25.9%) had higher stage non-surgical disease treated with chemotherapy.

Univariate analysis of the CT perfusion biomarkers revealed that CTP average, base, blood flow, mean transit time and t_{max} were all significantly associated with survival at p<0.05.

Receiver operating characteristic curve analysis of t_{max} and survival demonstrated an AUC of 66% indicating t_{max} has poor accuracy. A cut-value of t_{max} < 4.79 is however significantly correlated with poor survival, (HR=2.43, 1.18–5.01 95%CI, p=0.016).

4.4.12 Can CT Perfusion Predict Histological Subtype?

Univariate analysis of the CT perfusion biomarkers reveals statistically significant relationships between CTP4 average, base and IRF(t_0) and histological subtype, with odds ratios of 1.02 (1.01–1.04 95% CI) $p=0.014$, 1.05 (1.02–1.08 95%CI) $p=0.002$, and 1.23 (1.04–1.55 95%CI) $p=0.038$ respectively. These had an AUC on ROC analysis of 62.4%, 65.5% and 57.0% respectively indicating they were poor predictors and are less than that for TBR_{lung} (67.8%).

A statistically significant multivariate model was found using CTP4 average and IRF(t_0). However, this model only predicted SCC with an accuracy of 64.6% and an AUC of 59% on ROC analysis.

4.5 Discussion

This study has shown that there is no simple correlation between any of the CT perfusion metrics and survival, and that although multivariate predictors for SUV_{max} and surgery can be created, accuracy is poor and none of these have been shown to provide significant additional prognostication power over that of staging or that of ^{18}F -FDG-derived measures.

The failure of these techniques to provide a statistically significant predictor is disappointing and contradicts previous studies (97, 128, 130, 140, 200). This may relate to problems of our analysis and data-acquisition. The software used in this project, CT Perfusion 4D for lung lesions, is limited to a single arterial input; however, as discussed in the introductory chapter, lung lesions can have dual arterial supply from the bronchial and the pulmonary arteries (117, 118, 122, 200, 201). In lesions where such a dual-arterial supply was present, the biomarkers calculated using a single arterial input function derived from the aorta could be a poor estimate of the true CT perfusion biomarkers (119, 121, 148, 200). Several papers propose using the same dual-perfusion analysis software used for hepatic lesions with regions of interest placed on the pulmonary artery and on the aorta. This would allow for the bronchial and pulmonary arterial flow to be estimated and accounted for; however, it would also increase the number of biomarkers to be estimated leading to increased noise and increased effect from movement and other error inducing problems. The data from this study is also not suitable for this analysis as in many cases the pulmonary artery is not within the scanned volume. Other papers suggest alternative calculation methods, for example, slope-intercept analysis and simple enhancement differences (143, 202). However, it is worth noting that only six of the 11 biomarkers provided by CT Perfusion 4D are dependent on deconvolution using the arterial input function. The remaining 5 are slope and graph biomarkers and there is a high correlation between 3 of the deconvolution dependent biomarkers and the non-deconvolution dependent biomarkers.

Similarly the software used in this project does not perform breath or motion correction. Several previous authors have suggested that motion correction would be helpful; however, this functionality was not available to the authors of this study.

Another potential issue is related to patient selection. The study population is a subset of the larger ^{18}F -FDG-PET/CT population, and has the same biases inherent its patient population due to recruitment factors. The study population is heavily weighted toward those with lower disease stage and likely operable tumours, with a bias towards surgically fit patients as compared to the normal population of the lung cancer patients. These biases mean that the survival of our population of Stage II–IV patients is likely to be artificially long — especially for the larger tumours. It may also artificially increase the difference in survival between those treated with surgery versus those not, as non-surgical treatment may be reflecting worse non-tumoural prognostic factors, e.g. heart disease, fibrosis, and emphysema. Further, the lower stage means that the tumours are smaller, and thus more susceptible to partial volume effects, breath motion and other motion artefacts.

Previous papers have suggested that CT perfusion biomarkers are important for survival in larger non-surgical tumours (121, 139–141, 203). When the study population is restricted to these patients, we do find that markers of increased angiogenesis are correlated with poorer survival. The inability to detect a similar effect across the whole of our cohort suggests that these features may only be helpful in larger tumours or may be quantifying a risk that can be determined qualitatively by expert reviewers.

4.6 Conclusion

There is no definite clear correlation with CT perfusion biomarkers and survival, and there is no clear added benefit to CT perfusion over that ^{18}F -FDG based staging and surgery. In subgroup analysis restricted to the higher stage patients treated with chemotherapy there are statistically significant correlations between survival and the CT perfusion biomarkers; however, caution should be taken when interpreting these as the numbers of patients in this group are small. Importantly we were unable to create a multivariate linear regression model model to predict SUV_{max} using parameters obtained from CT perfusion suggesting that CT perfusion cannot replace ^{18}F -FDG PET/CT imaging.

4.7 Tables

Gender	Overall, N = 162	Female, N = 67	Male, N = 95	p-value ¹
Age at Enrolment				>0.9
N	162.0	67.0	95.0	
Median (IQR)	71.0 (63.0, 75.0)	69.0 (62.5, 77.0)	71.0 (63.0, 75.0)	
Range	44.0, 96.0	44.0, 88.0	49.0, 96.0	
Radiological Stage				0.7
I	56 (35%)	23 (34%)	33 (35%)	
II	29 (18%)	11 (16%)	18 (19%)	
III	56 (35%)	26 (39%)	30 (32%)	
IV	21 (13%)	7 (10%)	14 (15%)	
Surgery	76 (47%)	30 (45%)	46 (48%)	0.6
SUV_{max}				0.7
Median (IQR)	11.8 (7.0, 16.6)	11.5 (7.0, 16.3)	12.0 (6.9, 16.9)	
Range	0.5, 40.0	0.5, 33.6	1.4, 40.0	
CTP4 average				0.2
Median (IQR)	24.0 (8.4, 39.8)	27.3 (10.1, 39.9)	21.7 (8.1, 39.2)	
Range	0.0, 325.1	0.0, 62.0	0.0, 325.1	
CTP4 base				0.9
Median (IQR)	16.4 (5.7, 27.4)	16.5 (5.4, 27.2)	16.0 (6.0, 27.3)	
Range	0.0, 94.1	0.0, 37.6	0.0, 94.1	
CTP4 time to peak				>0.9
Median (IQR)	37.6 (29.4, 45.9)	37.6 (29.3, 44.2)	37.6 (29.4, 45.9)	
Range	2.9, 88.3	14.1, 69.1	2.9, 88.3	
CTP4 positive enhancement integral				0.8
Median (IQR)	0.3 (0.2, 0.3)	0.3 (0.2, 0.3)	0.2 (0.2, 0.3)	
Range	0.0, 4.1	0.0, 0.8	0.0, 4.1	
CTP4 mean slope of increase				0.5

Gender	Overall, N = 162	Female, N = 67	Male, N = 95	p-value ¹
Median (IQR)	4.1 (2.8, 6.2)	4.2 (2.9, 6.5)	4.0 (2.8, 6.1)	
Range	0.9, 40.9	1.3, 20.5	0.9, 40.9	
CTP4 blood volume				>0.9
Median (IQR)	6.6 (4.7, 8.9)	6.6 (4.9, 8.7)	6.8 (4.5, 9.2)	
Range	0.0, 146.3	0.5, 17.3	0.0, 146.3	
CTP4 blood flow				0.2
Median (IQR)	74.8 (52.1, 128.3)	69.3 (52.0, 108.5)	80.8 (53.9, 146.3)	
Range	0.0, 818.8	5.1, 373.9	0.0, 818.8	
CTP4 mean transit time				0.057
Median (IQR)	8.2 (5.3, 9.9)	8.9 (5.5, 11.1)	7.5 (5.3, 9.4)	
Range	0.0, 25.1	2.1, 23.8	0.0, 25.1	
CTP4 IRF(t₀)				0.4
Median (IQR)	0.6 (0.2, 1.1)	0.6 (0.2, 1.1)	0.5 (0.2, 1.0)	
Range	0.0, 16.2	0.0, 8.2	0.0, 16.2	
CTP4 t_{Max}				0.081
Median (IQR)	4.8 (3.2, 6.2)	5.3 (3.6, 6.6)	4.6 (3.1, 5.7)	
Range	0.0, 27.8	1.5, 12.0	0.0, 27.8	
CTP4 ps				0.2
Median (IQR)	10.5 (6.8, 14.9)	10.9 (7.8, 14.9)	9.7 (5.8, 14.8)	
Range	0.0, 281.8	0.6, 55.1	0.0, 281.8	

¹Wilcoxon rank sum test; Pearson's Chi-squared test

Table 16: Patient demographics as compared to gender

Survival	HR ¹	95% CI ¹	p-value
Radiological Stage			
I	—	—	
II	3.55	1.92, 6.57	<0.001
III	4.30	2.50, 7.39	<0.001
IV	6.61	3.53, 12.4	<0.001

¹HR = Hazard Ratio, CI = Confidence Interval

Table 17: Univariate Cox regression of survival versus radiological stage

Multivariate Regression	HR ¹	95% CI ¹	p-value
Radiological Stage			
I	—	—	
II	3.24	1.74, 6.04	<0.001
III	3.01	1.70, 5.33	<0.001
IV	3.66	1.85, 7.23	<0.001
Surgery			
No	—	—	
Yes	0.39	0.24, 0.63	<0.001

¹HR = Hazard Ratio, CI = Confidence Interval

Table 18: Multivariate Cox regression of survival versus radiological stage and surgical status

Univariate Regressions	HR ¹	95% CI ¹	p-value
CTP4 average	1.00	1.00, 1.01	0.9
CTP4 base	1.01	0.99, 1.02	0.3
CTP4 time to peak	1.00	0.98, 1.01	0.7
CTP4 positive enh. integral	0.65	0.35, 1.23	0.2
CTP4 mean slope of increase	0.96	0.92, 1.01	0.081
CTP4 blood volume	0.99	0.96, 1.01	0.3
CTP4 blood flow	1.00	1.00, 1.00	0.5
CTP4 mean transit time	0.99	0.95, 1.04	0.7
CTP4 irf to	0.95	0.85, 1.06	0.4
CTP4 tMax	0.97	0.91, 1.04	0.4
CTP4 ps	0.99	0.98, 1.00	0.2

¹HR = Hazard Ratio, CI = Confidence Interval

Table 19: Univariate regressions of survival against CT perfusion measurements

4.8 Figures

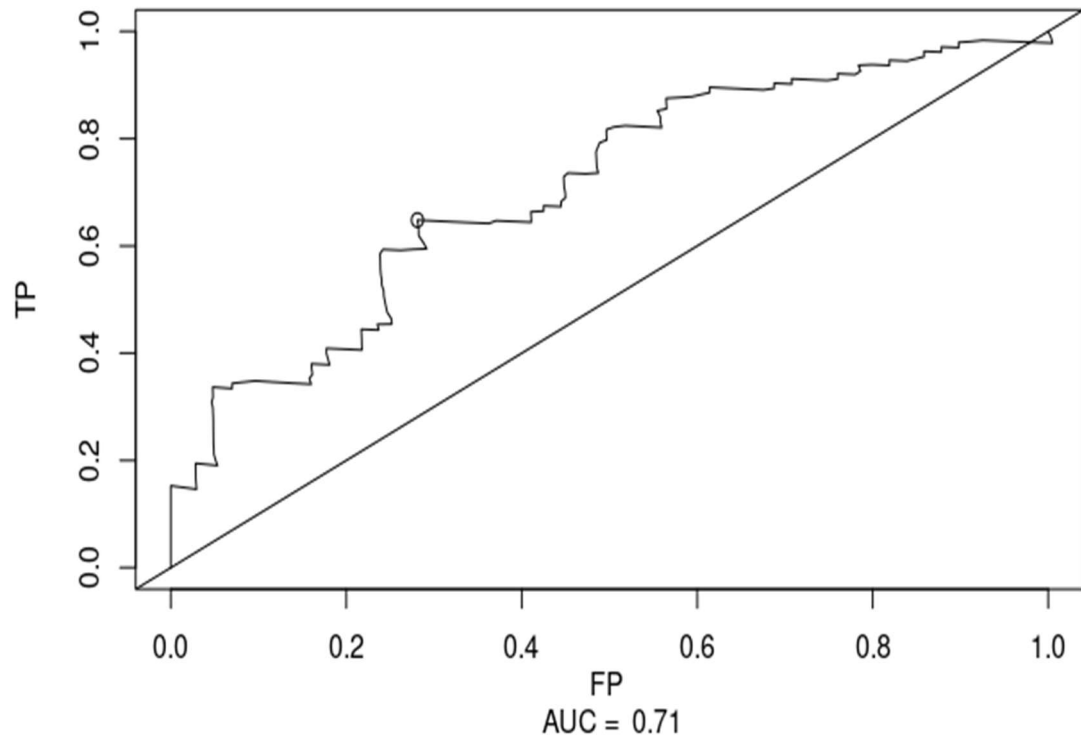


Figure 5: ROC curve for survival against $SUV_{max} > 11.52$

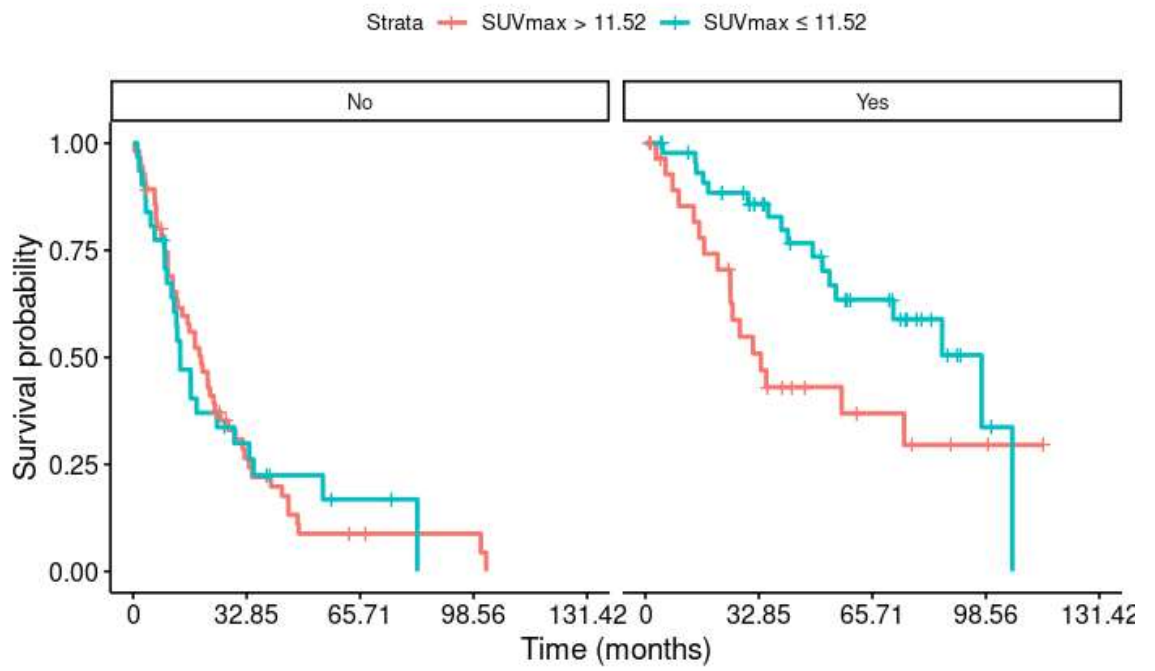


Figure 6: Survival vs $SUV_{max} > 11.52$ faceted by surgery

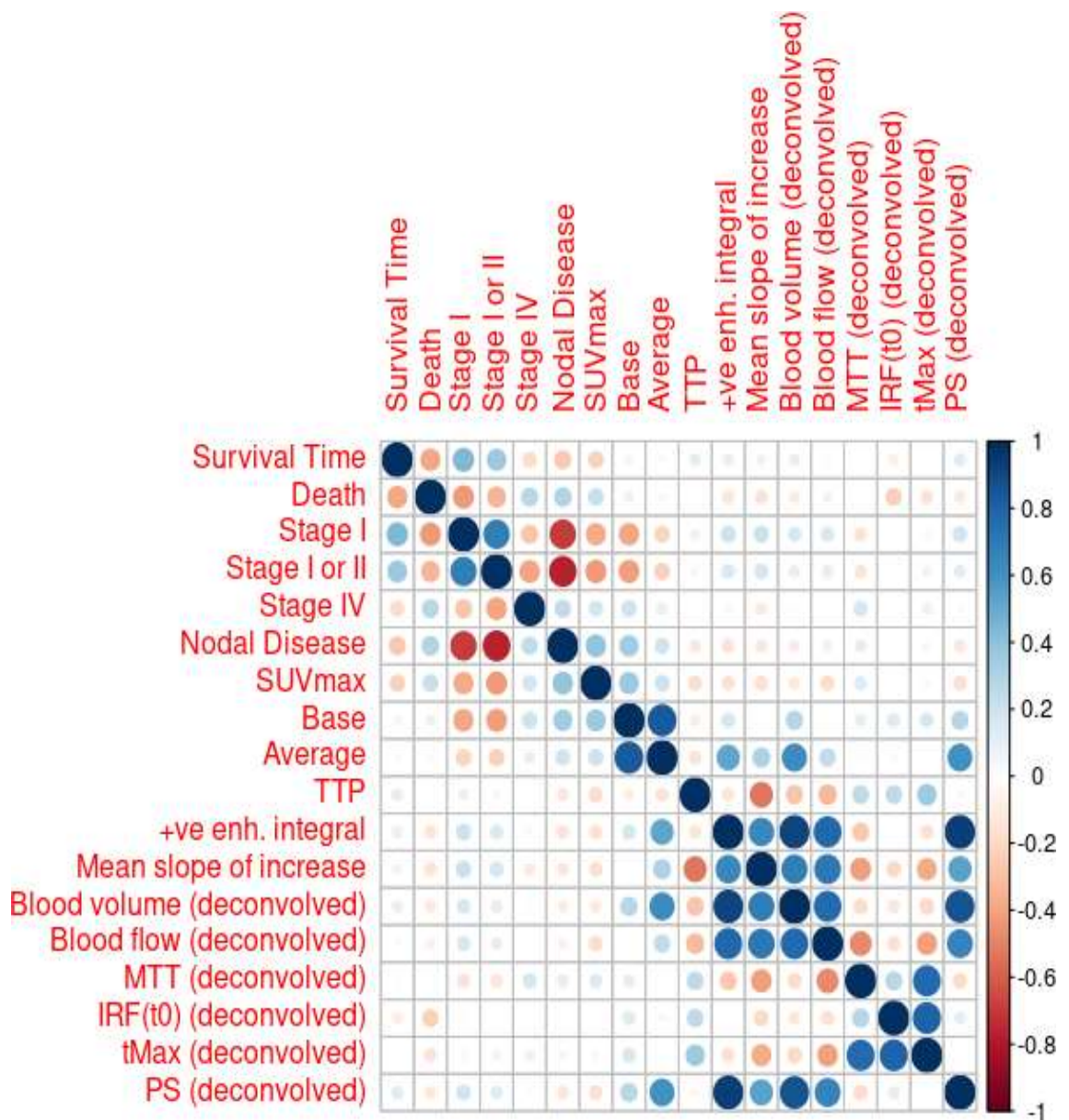


Figure 7: Correlation between CT perfusion biomarkers

5 Texture Analysis with TexRAD in Lung Cancer

5.1 Abstract

5.1.1 Purpose

To examine the correspondence between CT and PET textural biomarkers and survival in NSCLC.

5.1.2 Methods

484 patients with suspected lung cancer were recruited in to the study. Only patients who had ¹⁸F-FDG-PET/CTs, were diagnosed with NSCLC lung cancer and where TexRAD extraction was possible were included.

Histology and stage were noted, CT and PET textural features were extracted using TexRAD software.

Kaplan-Meier and Cox proportional hazard survival analysis was performed.

Adjustments for multiple comparisons were made, as per Benjamini and Hochberg as appropriate. Analysis was performed using R.

5.1.3 Findings

5.1.3.1 Patient Demographics

Of the 484 patients in the study, 475 had ¹⁸F-FDG-PET/CTs. Of these, 293 were determined to have NSCLC and 133 were determined to be benign. 290 of these NSCLC patients had successful extraction of TexRAD features.

Of these 290 NSCLC patients 161 were male and 129 were female. The median survival was 901 days (710–1082 days 95% CI).

5.1.3.2 Individual TexRAD Biomarkers at Median Cut-Point Across the Whole Cohort

Univariate analysis of the whole dataset reveals 29 biomarkers that when cut at the median point are statistically correlated with survival in univariate analysis at $p < 0.05$ when adjusted for multiple comparisons as per Benjamini and Hochberg. However,

none of these cut-points remain statistically significant when compared with surgery and staging.

5.1.3.3 Individual TexRAD Biomarkers at Optimal Cut-point for Stage I Across the Whole Cohort

Univariate analysis of the whole dataset reveals 34 biomarkers that when cut at the optimal cut-off point for stage I are statistically correlated with survival in univariate analysis at $p < 0.05$ when adjusted for multiple comparisons, as per Benjamini and Hochberg. 11 of these remain statistically significant when combined with surgery and staging.

5.2 Introduction

Although contrast-enhanced CT and ^{18}F -FDG-PET/CT are established in the diagnosis, staging and thence prognostication of non-small cell lung cancer (NSCLC) there has been considerable interest in the application of imaging analysis techniques to further improve prognostication through the recognition of and quantification of features associated with adverse biological characteristics, or potentially directly associated with worsened prognosis. Intratumoural necrosis, haemorrhage and myxoid change are all known to cause low attenuation on CT and low ^{18}F -FDG uptake, whereas hypoxia is known to be associated with high ^{18}F -FDG uptake.

Texture analysis methods may provide a mechanism for detecting tumours that contain such areas of low attenuation or altered uptake through the recognition and quantification of variations of intensity within pulmonary lesions. The biomarkers extracted would then be correlated with these already recognised biological risk factors and could hence provide an additional risk stratification method for the prognostication of NSCLC.

There are multiple methods for texture analysis, however, in this chapter we will use TexRAD (Feedback Medical Ltd., <https://fbkmed.com/textrad-landing-2/>, London/Cambridge, UK), a proprietary clinical-research texture analysis software platform. Texture biomarkers derived from the filtration-histogram and statistical approach used in TexRAD have been shown to be correlated with survival, response and histology in a number of cancers and have been shown to correlate with ^{18}F -FDG-PET SUV_{max} and CT perfusion biomarkers (150, 161, 161, 161, 168–183).

The aim of this study is therefore to assess if there is a statistically significant relationship between biomarkers derived from TexRAD and survival and histological subtype in NSCLC in the dataset.

5.3 Materials and Methods

5.3.1 Patient Population

The population of patients is as described in detail in Section 2.2 and Section 2.8.

There were a total of 290 patients with non-small cell cancer (NSCLC) who had TexRAD analysis and ^{18}F -FDG-PET/CT imaging.

5.3.2 ^{18}F -FDG-PET/CT Imaging Protocol

The imaging protocol is described in detail in Section 2.3.

5.3.3 ^{18}F -FDG-PET/CT Image Analysis

The ^{18}F -FDG-PET/CT image analysis protocol is described in detail in Section 2.4.

5.3.4 TexRAD Image Analysis

The TexRAD analysis protocol is described in detail in Section 2.4.

5.3.5 Statistics and Data Analysis

Statistical and data analysis is described in detail in Section 2.13.

5.4 Findings

5.4.1 Individual TexRAD Biomarkers at Median Cut-Point Across the Whole Cohort

Univariate analysis of the whole dataset reveals 29 biomarkers that, when cut at the median point are significant correlated with survival in univariate analysis with $p < 0.05$ when adjusted for multiple comparisons as per Benjamini and Hochberg. (See Table 20.) However, none of these cut-points remain statistically significant when combined with Surgery and Staging in multivariate analysis.

5.4.2 Individual TexRAD Biomarkers at Optimal Cut-Point for Stage I Across the Whole Cohort

When looking at our patient cohort, we note that the largest subgroup of patients are Stage I patients. We therefore performed a maximal logrank survival test against each of the biomarkers for the Stage I patients. We then performed univariate analysis of the whole dataset for these biomarkers at this optimal cut-point.

This univariate analysis of the whole dataset reveals 34 biomarkers which are statistically correlated with survival at $p < 0.05$ when adjusted for multiple comparisons as per Benjamini and Hochberg. (See Table 21.) We then performed multivariate survival analysis against surgery and survival for these biomarkers revealing eight of these remain statistically significant when combined with surgery and staging, with a decrease in the Akaike Information Criterion (AIC) of more than two. (See Table 22.)

5.4.3 Training and Testing Cohort Analysis

Following random sampling the patient cohort was divided into two approximately equal groups. (145 training and 147 testing).

Out of 145 patients in the training cohort, 103 died, with a median survival of 888 days (621–1102 days 95% CI). Statistical analysis reveals that CT entropy and CT kurtosis at various spatial scale filters are significant predictors of overall survival. In particular, at the fine texture scale (SSF=2mm), median cut-offs (derived from the whole population) for CT entropy ($\text{entropy_ct_ssf_2} \geq 5.19$) and kurtosis ($\text{kurtosis_ct_ssf_2} \geq 0.42$) and at the medium texture scale (SSF=3mm), median cut-off for kurtosis ($\text{kurtosis_ct_ssf_3} \geq$

0.42) identified patients with poor prognosis ($p = 0.008$, 0.011 and 0.011 respectively). A high CT kurtosis value without filtration (SSF=0) also identified patients with poor prognosis ($\text{kurtosis_ct_ssf}_0 \geq 0.12$, $p=0.008$) as did high ^{18}F -FDG-PET entropy without filtration ($\text{entropy_pet_ssf}_0 \geq 4.55$, $p=0.001$).

The testing cohort consisted of 147 patients, 104 of whom died, with a median survival of 901 days (656–1474 days 95% CI). Of the above significant markers in the training cohort, only CT entropy at fine texture scale ($\text{entropy_ct_ssf}_2 \geq 5.19$, HR 2.5, 1.7–3.7 95% CI, $p<0.001$,

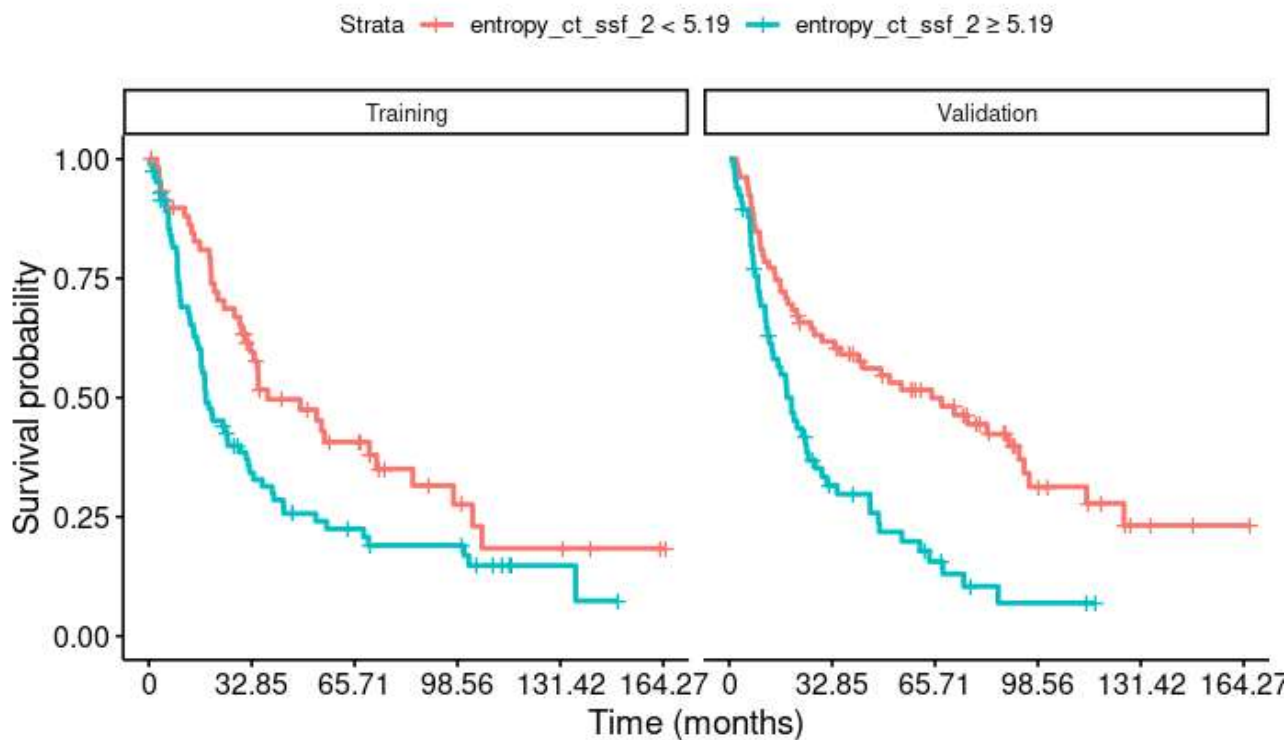


Figure 8), CT kurtosis at medium texture scale ($\text{kurtosis_ct_ssf}_3 \geq 0.42$, HR 2.0, 1.3–3.0 95% CI, $p=0.002$, Figure 9) and ^{18}F -FDG-PET entropy without filtration ($\text{entropy_pet_ssf}_0 \geq 4.55$, HR 2.1, 1.4–3.2 95% CI, $p<0.001$,

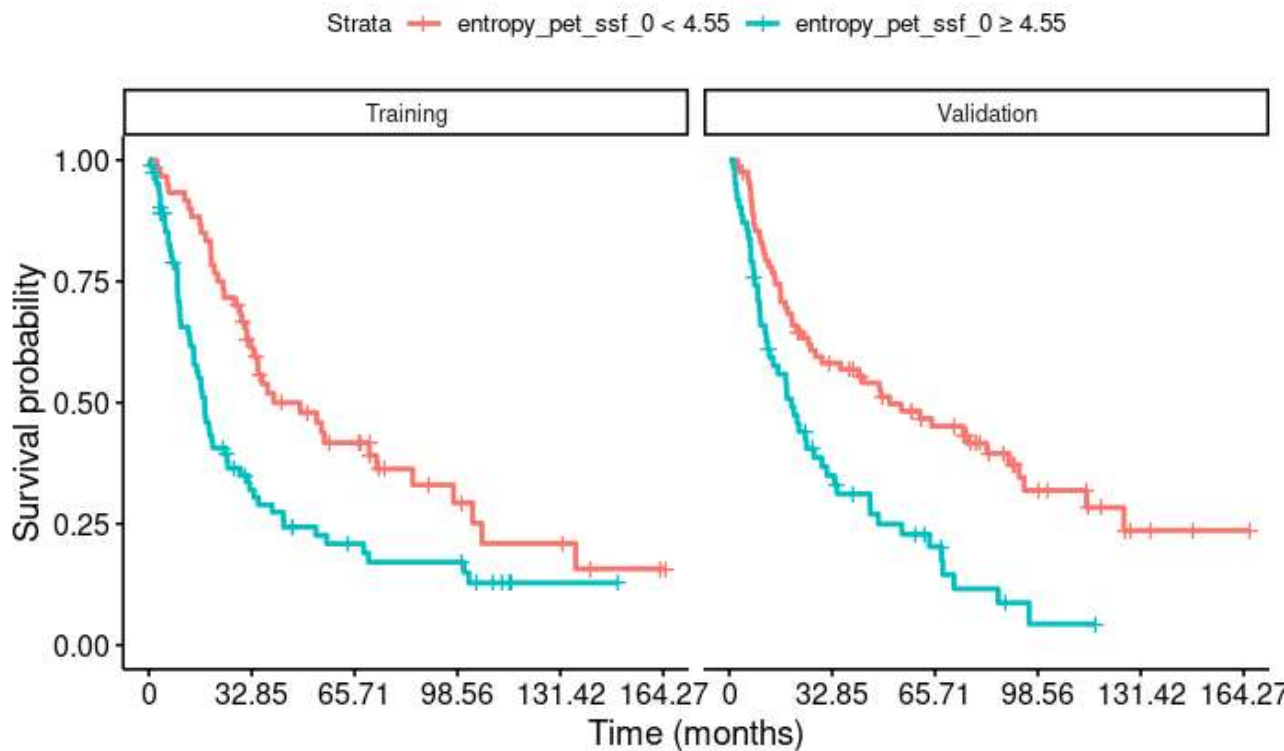


Figure 10) remained significant.

A multivariate Cox regression model comprising of the above three significant and validated markers along with their interactions demonstrated that CT entropy at fine texture ($\text{entropy_ct_ssf_2} \geq 5.19$) is the only independent predictor of survival ($p < 0.001$). This is significant in combination with Stage but it does not remain significant in combination with surgery and staging.

5.4.4 Correlation Between TexRAD Biomarkers

A simple correlation plot reveals that there is considerable correlation between the entropy biomarkers at all SSF levels and there is some correlation between ^{18}F -FDG PET and CT image derived entropy. Mean and standard deviation biomarkers are well correlated and this is likely to represent the effect of intensity magnitude on standard deviation. Within the ^{18}F -FDG PET derived biomarkers, there is good to excellent correlation between kurtosis and skewness across SSF levels. (See

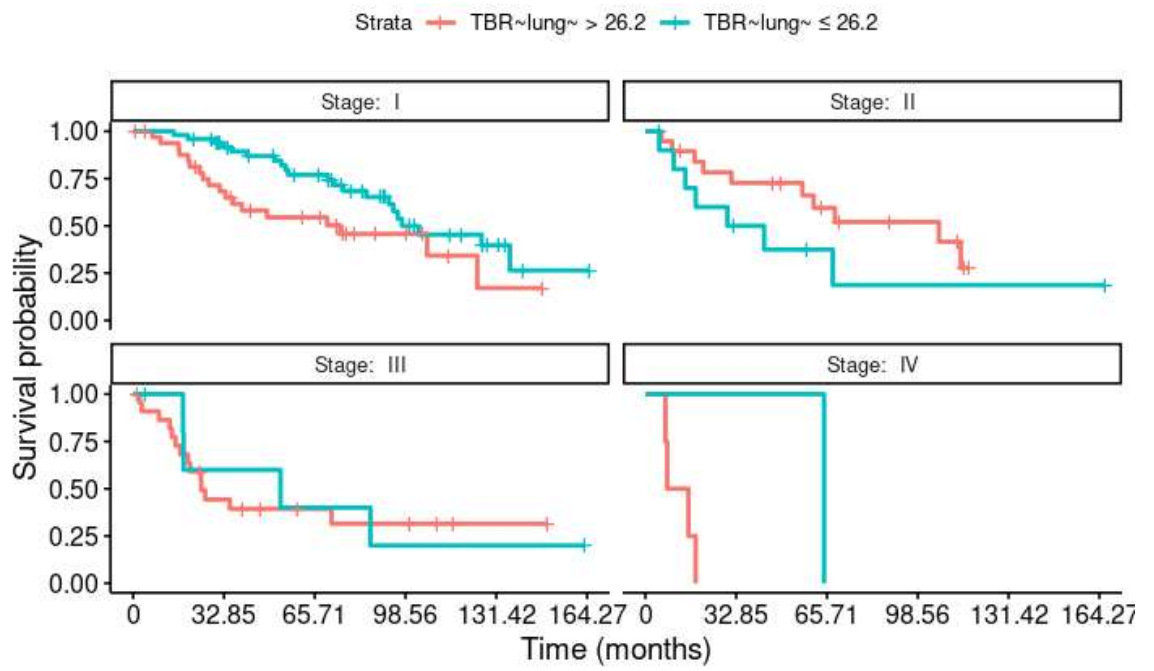


Figure 4.)

5.5 Discussion

This study has shown that multiple CT and PET textural features are statistically significantly related to survival, and in particular CT entropy at fine texture (SSF=2mm) is statistically significantly related to survival when combined with surgery and staging, and remains statistically significant when the whole treatment group is split into training and validation sets.

Entropy is a measure of tumour heterogeneity which is a recognized feature of malignancy. Malignant tumours contain areas of necrosis, high cell density, haemorrhage, scarring and myxoid change (62, 204, 205). It is not hard to see that these areas will have differing tissue densities and thus CT attenuation, and similarly, differing ^{18}F -FDG uptake. Thus this biological heterogeneity can be reflected in imaging as image heterogeneity and image texture. However, it should be recognised that normal tissues also display a degree of heterogeneity, and thus the relationships between heterogeneity, diagnosis and survival can be complex. A potential method to help differentiate between abnormal and pathological heterogeneity, versus the normal heterogeneity that would be expected, is through recognition that the scales on which normal and abnormal heterogeneity are apparent can differ. TexRAD uses image filtration with Laplacian of Gaussian filters which highlight textural features at different scales and we have found that the filtration fine and medium textural features most strongly correlate with survival. However, our study has also shown that CT entropy is relatively strongly correlated with itself at different texture scales.

Many biomarkers derived from texture analysis provide some measurement of heterogeneity: entropy is an intensity magnitude independent measure of heterogeneity and is related to the average uncertainty in the intensity across the ROI. CT entropy appears to be poorly correlated with standard deviation (a different measure of heterogeneity) and most mean biomarkers — but there is a weak correlation between these biomarkers and unfiltered mean. This correlation may reflect the way that whilst the Laplacian of Gaussian filter highlights features at some frequencies, it blurs features at others. This blurring involves pushing the intensity closer to the mean intensity for those non-highlighted frequencies.

The finding that $\text{entropy_ct_ssf_2} > 4.81$ remains statistically significant in a combined model with staging and surgical status across the whole dataset suggests that TexRAD can be used to provide additional stratification over that of staging and surgical status alone. The technique for ROI selection used in the study is quick and simple, many other studies have relied on segmenting the whole tumour often using a separate diagnostic CT. In this study, the ROI was chosen from a single slice at the level of the SUV_{max} . This was further coupled with CT thresholding, allowing one to draw more generous borders around tumours centred within the lung but still resulting in the same ROI. These techniques makes ROI segmentation quicker, more repeatable and easier.

A limitation of our study is the relative small number of patients and the biases inherent its patient population due to recruitment factors. The study population is heavily weighted toward those with lower disease stage and likely operable tumours, with a bias towards surgically fit patients as compared to the normal population of patients with lung cancer. These biases mean that the survival of our population of Stage II–IV patients is likely to be artificially large — especially for the larger tumours. It may also artificially increase the difference in survival between those treated with surgery versus those not, as non-surgical treatment may be reflecting worse non-tumoural prognostic factors, e.g. heart disease, fibrosis, and emphysema. Further, the lower stage means that the tumours are smaller, and thus more susceptible to partial volume effects, breath motion and other motion artefacts. The small number of patients means that we cannot check if the proposed cut off remains statistically significant when combined to full staging (i.e. Stage Ia, Ib, Ic, IIa etc. vs Stage I, II, III and IV). Similarly, the biases within the dataset mean that there are likely other significant markers that have been hidden by the significant survival benefit from the surgery. These factors mean that the discovery that $\text{entropy_ct_ssf_2} > 4.81$ is still a significant predictor of worse survival even in combination with surgery and staging is more significant.

5.6 Conclusion

Multiple CT and PET textural features are statistically significantly related to survival and in particular CT entropy at fine texture (SSF=2mm) is statistically significantly related to survival when combined with surgery and staging, and remains statistically significant when the whole treatment group is split into training and validation sets.

5.7 Tables

Characteristic	HR (CI) ¹	p-value	adjusted p-value
entropy_pet_ssf_2 ≤ 4.55	0.51 (0.38 to 0.67)	<0.001	<0.001
entropy_pet_ssf_4 ≤ 4.555	0.50 (0.38 to 0.66)	<0.001	<0.001
entropy_pet_ssf_6 ≤ 4.55	0.51 (0.38 to 0.67)	<0.001	<0.001
entropy_pet_ssf_0 ≤ 4.555	0.50 (0.38 to 0.66)	<0.001	<0.001
entropy_pet_ssf_3 ≤ 4.55	0.50 (0.38 to 0.66)	<0.001	<0.001
entropy_pet_ssf_5 ≤ 4.56	0.51 (0.38 to 0.67)	<0.001	<0.001
entropy_ct_ssf_2 ≤ 5.195	0.51 (0.39 to 0.68)	<0.001	<0.001
entropy_ct_ssf_5 ≤ 4.92	0.57 (0.43 to 0.75)	<0.001	<0.001
kurtosis_ct_ssf_3 ≤ 0.43	0.57 (0.43 to 0.75)	<0.001	<0.001
entropy_ct_ssf_6 ≤ 4.88	0.57 (0.43 to 0.76)	<0.001	<0.001
entropy_ct_ssf_3 ≤ 5.055	0.58 (0.44 to 0.76)	<0.001	<0.001
entropy_ct_ssf_0 ≤ 4.52	0.59 (0.45 to 0.78)	<0.001	0.001
kurtosis_ct_ssf_5 ≤ -0.135	0.62 (0.47 to 0.82)	<0.001	0.004
entropy_ct_ssf_4 ≤ 4.99	0.62 (0.47 to 0.82)	<0.001	0.004
kurtosis_ct_ssf_6 ≤ -0.3	0.63 (0.48 to 0.83)	0.001	0.005
mean_ct_ssf_0 ≤ 18.13	0.64 (0.48 to 0.84)	0.001	0.005
kurtosis_ct_ssf_4 ≤ 0.065	0.64 (0.48 to 0.84)	0.001	0.005
kurtosis_ct_ssf_0 ≤ 0.12	0.65 (0.49 to 0.85)	0.002	0.007
sd_pet_ssf_0 ≤ 7378.315	0.65 (0.49 to 0.85)	0.002	0.007
skewness_pet_ssf_5 ≤ 1.58	1.52 (1.15 to 2.01)	0.003	0.010
kurtosis_ct_ssf_2 ≤ 0.435	0.67 (0.51 to 0.88)	0.004	0.014
mean_pet_ssf_6 ≤ 875.095	1.49 (1.13 to 1.96)	0.005	0.016
kurtosis_pet_ssf_0 ≤ 0.715	1.46 (1.11 to 1.93)	0.007	0.021
skewness_pet_ssf_6 ≤ 1.535	1.45 (1.10 to 1.91)	0.008	0.025
mean_ct_ssf_4 ≤ 1.89	1.44 (1.09 to 1.89)	0.010	0.029
skewness_pet_ssf_4 ≤ 1.66	1.42 (1.08 to 1.88)	0.012	0.033
mean_pet_ssf_5 ≤ 488.73	1.39 (1.06 to 1.84)	0.019	0.049
skewness_pet_ssf_2 ≤ 1.635	1.39 (1.05 to 1.82)	0.020	0.050

skewness_pet_ssf_3 ≤ 1.68	1.39 (1.05 to 1.83)	0.019	0.050
---------------------------	---------------------	-------	-------

¹HR = Hazard Ratio, CI = Confidence Interval

Table 20: TexRAD biomarkers in univariate analysis against survival with median cut-off with p<0.05 as adjusted by Benjamini and Hochberg

Characteristic	HR (CI) ¹	p-value	adjusted p-value
entropy_ct_ssf_2 ≤ 4.81	0.37 (0.26 to 0.53)	<0.001	<0.001
entropy_ct_ssf_3 ≤ 4.86	0.41 (0.29 to 0.56)	<0.001	<0.001
entropy_pet_ssf_2 ≤ 4.16	0.42 (0.30 to 0.58)	<0.001	<0.001
entropy_pet_ssf_4 ≤ 4.16	0.42 (0.30 to 0.58)	<0.001	<0.001
entropy_pet_ssf_6 ≤ 4.16	0.42 (0.30 to 0.58)	<0.001	<0.001
entropy_pet_ssf_0 ≤ 4.16	0.42 (0.30 to 0.58)	<0.001	<0.001
entropy_pet_ssf_3 ≤ 4.16	0.42 (0.30 to 0.58)	<0.001	<0.001
entropy_pet_ssf_5 ≤ 4.16	0.42 (0.30 to 0.58)	<0.001	<0.001
entropy_ct_ssf_4 ≤ 4.78	0.43 (0.31 to 0.59)	<0.001	<0.001
entropy_ct_ssf_0 ≤ 4.36	0.43 (0.31 to 0.60)	<0.001	<0.001
entropy_ct_ssf_6 ≤ 4.69	0.46 (0.34 to 0.62)	<0.001	<0.001
entropy_ct_ssf_5 ≤ 4.76	0.49 (0.36 to 0.67)	<0.001	<0.001
kurtosis_ct_ssf_2 ≤ 0.88	0.57 (0.43 to 0.76)	<0.001	<0.001
kurtosis_ct_ssf_3 ≤ 0.07	0.58 (0.44 to 0.78)	<0.001	<0.001
sd_pet_ssf_0 ≤ 2565.16	0.25 (0.09 to 0.66)	<0.001	0.002
mean_ct_ssf_0 ≤ 17.9	0.61 (0.46 to 0.81)	<0.001	0.002
skewness_pet_ssf_0 ≤ 2	2.05 (1.29 to 3.25)	<0.001	0.003
kurtosis_ct_ssf_0 ≤ -0.98	0.30 (0.12 to 0.72)	0.001	0.004
mpp_ct_ssf_2 ≤ 65.86	1.91 (1.25 to 2.93)	0.001	0.005
mean_ct_ssf_2 ≤ 9.7	2.97 (1.32 to 6.71)	0.002	0.006
mean_ct_ssf_3 ≤ 10.71	2.29 (1.24 to 4.20)	0.003	0.009
sd_pet_ssf_6 ≤ 7538.82	0.36 (0.16 to 0.82)	0.004	0.012
mpp_pet_ssf_5 ≤ 5947.88	0.37 (0.16 to 0.84)	0.005	0.016
mean_pet_ssf_4 ≤ 335.13	1.48 (1.11 to 1.98)	0.007	0.019
sd_pet_ssf_4 ≤ 6124.9	0.46 (0.24 to 0.87)	0.007	0.019
sd_pet_ssf_5 ≤ 7157.2	0.40 (0.19 to 0.86)	0.007	0.019
mpp_pet_ssf_6 ≤ 7096.73	0.42 (0.21 to 0.86)	0.007	0.019

Characteristic	HR (CI) ¹	p-value	adjusted p-value
sd_ct_ssf_2 ≤ 88.19	1.93 (1.12 to 3.33)	0.009	0.023
mean_pet_ssf_0 ≤ 6871.69	0.57 (0.36 to 0.90)	0.009	0.023
mpp_pet_ssf_0 ≤ 6871.69	0.57 (0.36 to 0.90)	0.009	0.023
mpp_ct_ssf_3 ≤ 34.58	1.45 (1.09 to 1.93)	0.014	0.032
mean_pet_ssf_6 ≤ 1259.75	1.46 (1.06 to 1.99)	0.016	0.036
mean_pet_ssf_3 ≤ 168.1	1.41 (1.06 to 1.88)	0.018	0.039
mean_pet_ssf_5 ≤ 368.53	1.40 (1.06 to 1.85)	0.018	0.039

¹HR = Hazard Ratio, CI = Confidence Interval

Table 21: TexRAD biomarkers in univariate analysis against survival with optimal cut-off in radiological stage I with $p < 0.05$ as adjusted by Benjamini and Hochberg

Characteristic	Coefficient HR (CI) ¹	Coefficient p-value	AIC ²	Δ AIC ³
entropy_ct_ssf_2 ≤ 4.81	0.60 (0.40 to 0.91)	0.016	1,914.59	-4.09
kurtosis_ct_ssf_2 ≤ 0.88	0.71 (0.53 to 0.95)	0.022	1,915.55	-3.13
entropy_pet_ssf_2 ≤ 4.16	0.67 (0.46 to 0.97)	0.032	1,915.89	-2.79
entropy_pet_ssf_4 ≤ 4.16	0.67 (0.46 to 0.97)	0.032	1,915.89	-2.79
entropy_pet_ssf_6 ≤ 4.16	0.67 (0.46 to 0.97)	0.032	1,915.89	-2.79
entropy_pet_ssf_0 ≤ 4.16	0.67 (0.46 to 0.97)	0.032	1,915.89	-2.79
entropy_pet_ssf_3 ≤ 4.16	0.67 (0.46 to 0.97)	0.032	1,915.89	-2.79
entropy_pet_ssf_5 ≤ 4.16	0.67 (0.46 to 0.97)	0.032	1,915.89	-2.79

¹HR = Hazard Ratio, CI = Confidence Interval for the coefficient of the characteristic in the multivariate model

²AIC = Akaike Information Criterion for the multivariate model

³ Δ AIC = The difference in the Akaike Information Criterion for the multivariate model as compared to the multivariate model consisting of Surgical status and Stage which has an AIC of 1918.68

Table 22: Statistically significant multivariate models versus survival with cut-offs as above

Variables in the Equation (final-step)	HR	CI	p-value
entropy_ct_ssf_2 ≥ 5.19	2.5	1.7 to 3.7	< 0.001

Variables not in the Equation (final-step)	Score	df	p-value
kurtosis_ct_ssf_3 ≥ 0.42	2.900	1	0.089
entropy_pet_ssf_0 ≥ 4.55	2.976	1	0.085
entropy_ct_ssf_2 ≥ 5.19 * kurtosis_ct_ssf_3 ≥ 0.42	0.002	1	0.964
entropy_ct_ssf_2 ≥ 5.19 * entropy_pet_ssf_0 ≥ 4.55	1.634	1	0.201
entropy_pet_ssf_0 ≥ 4.55 * kurtosis_ct_ssf_3 ≥ 0.42	0.480	1	0.488

*Table 23: Multivariate step-wise (Forward-Wald) Cox regression analysis comprising of significant and validated CTTA (entropy at fine-texture and kurtosis at medium-texture) and PETTA (entropy without filtration) along with their interaction. HR = hazard ratio, df - degrees of freedom, * - interaction between the two variables*

5.8 Figures

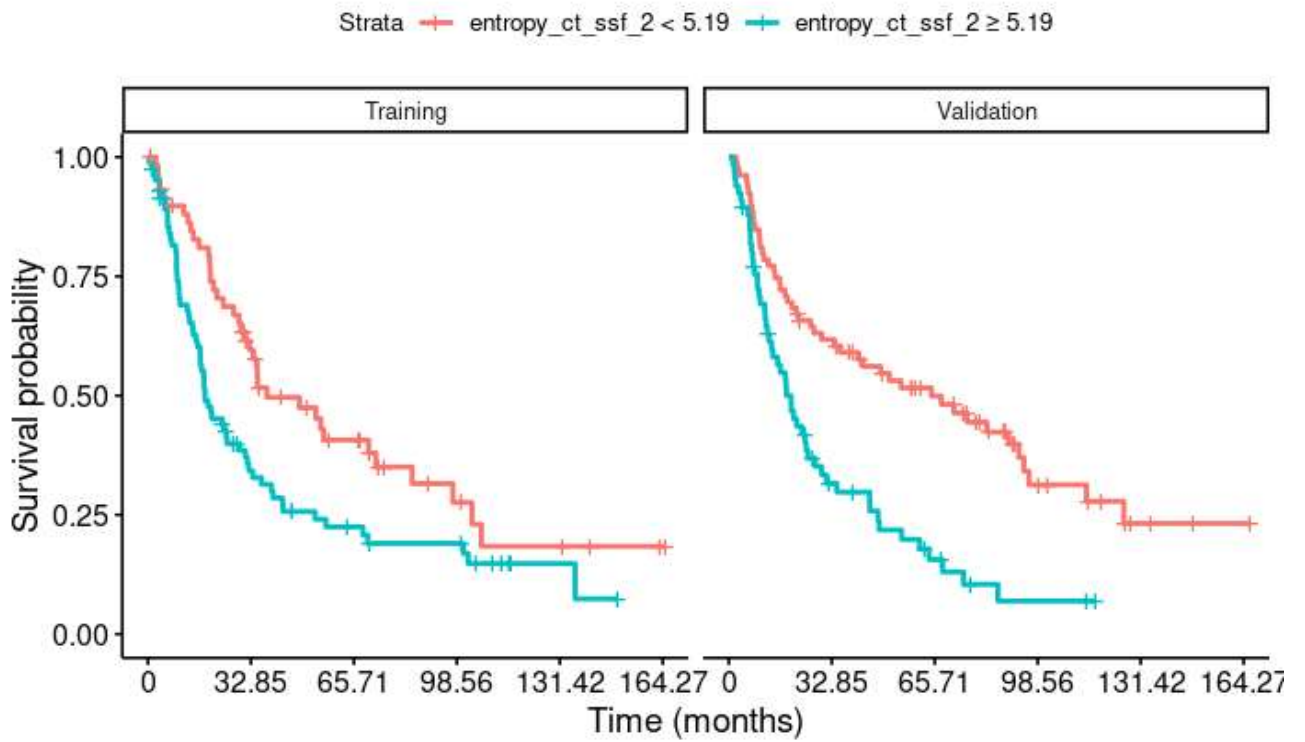


Figure 8: Survival analysis for entropy_ct_ssf_2 in training, $p=0.008$ & validation, $p<0.001$ cohorts

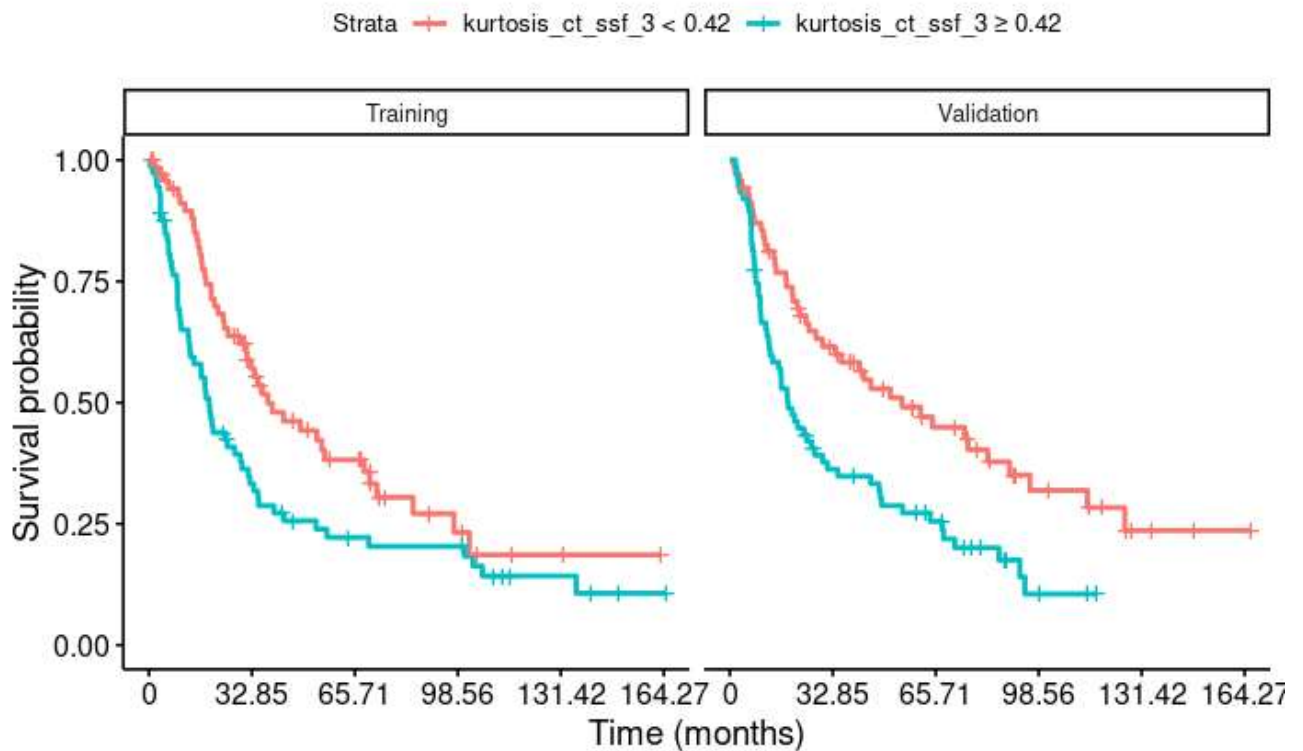


Figure 9: Survival analysis for kurtosis_ct_ssf_3 in training, $p=0.012$ & validation, $p=0.002$ cohorts

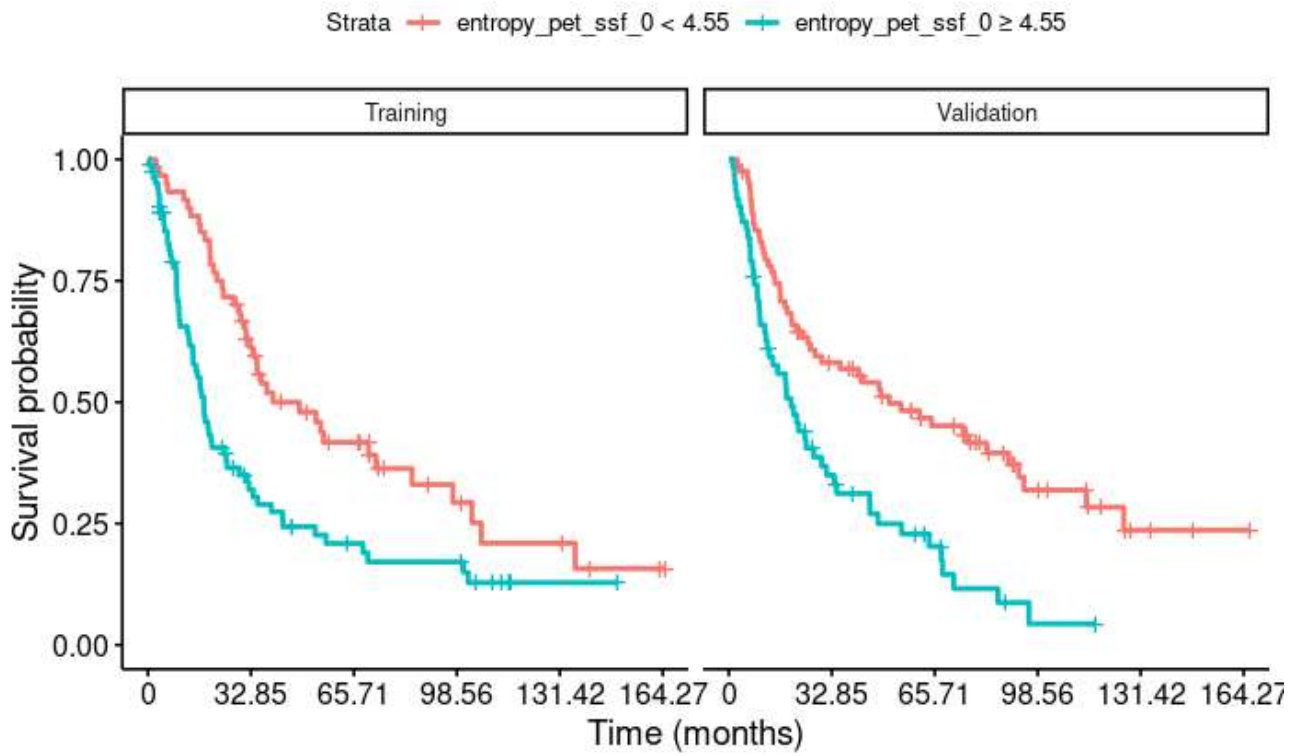


Figure 10: Survival analysis for entropy_pet_ssf_0 in training, $p=0.001$ & validation, $p<0.001$ cohorts

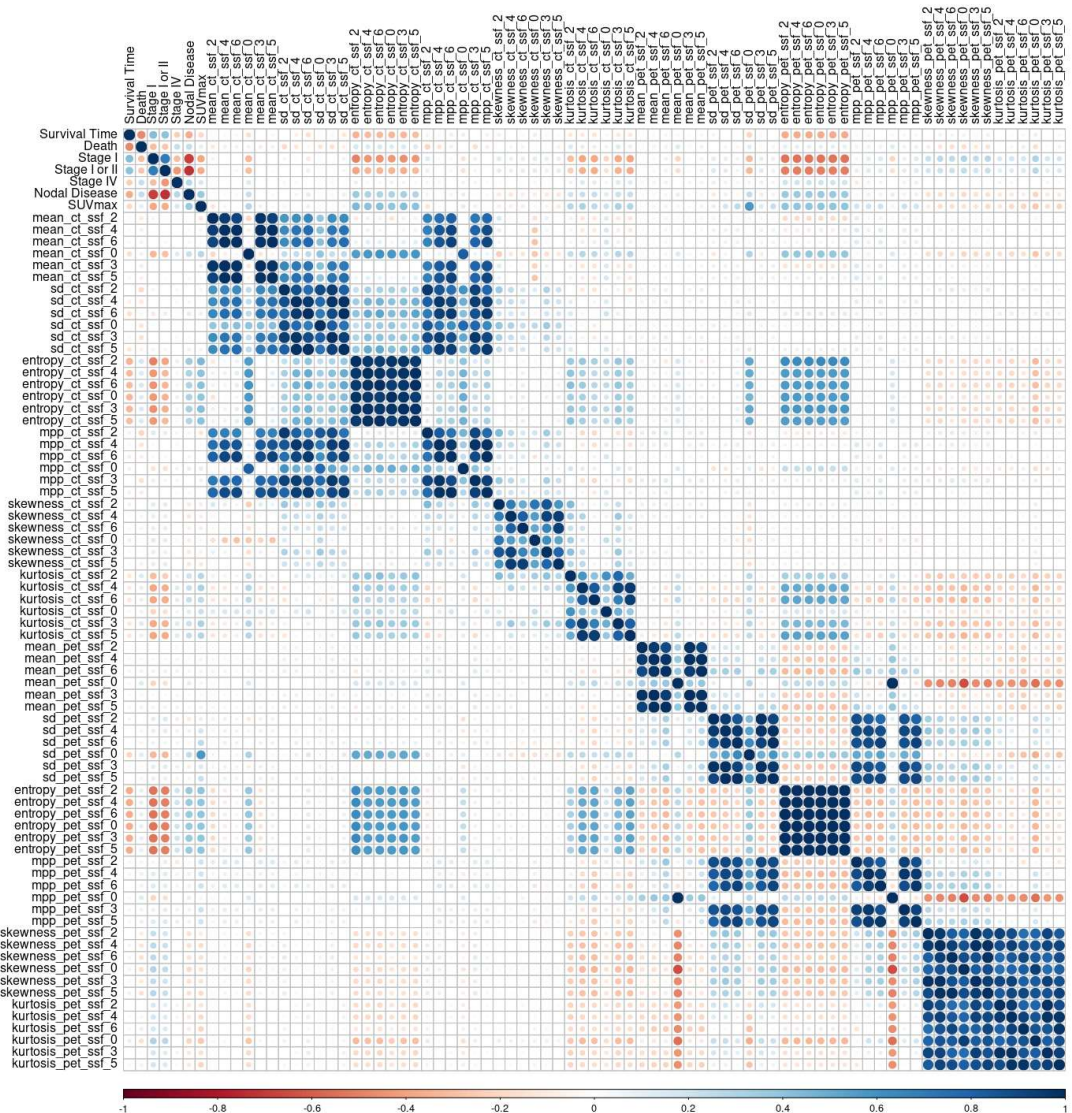


Figure 11: Correlation of Texrad derived biomarkers

6 Correlation Between Immunohistochemistry and Mutation and Imaging Biomarkers

6.1 Abstract

6.1.1 Purpose

To examine the association between imaging biomarker biomarkers and immunohistochemistry and mutation analysis in NSCLC.

6.1.2 Methods

484 patients with suspected lung cancer were recruited to the study. In this part of the investigation, we only selected patients with NSCLC who underwent surgery and had tissue data for analysis.

Histology and Stage were noted and ¹⁸F-FDG-PET/CT, textural analysis and CT perfusion biomarkers were analysed.

Kaplan-Meier and Cox proportional hazard survival analysis was performed. Univariate and multivariate analysis was performed using R and SPSS.

6.1.3 Results

Of the 484 patients, immunohistochemistry results were available for 147 patients and genomic analysis was available for 96 patients.

The most significant result was moderate correlation between the SUV biomarkers and GLUT1 (e.g. SUV_{max} $r=0.441$, $p<0.001$). There was a significant weak correlation between SUV biomarkers (e.g. SUV_{peak} $r=0.318$, $p=0.026$), some textural biomarkers (e.g. kurtosis_{ct_ssf_3} $r=0.356$, $p=0.012$) and CD105.

A significant moderate correlation was demonstrated between Inflammation and CTP4 mean slope of increase ($r=-0.442$, $p=0.021$) with a few other weaker correlations with textural biomarkers. HIF-1 α demonstrated significant weak correlations between CTP4 time-to-peak ($r=-0.312$, $p=0.023$) and entropy_{pet_ssf_3} ($r=0.344$, $p=0.015$) amongst others. PIK3CA mutation similarly demonstrated significant weak correlations between CTP4 average ($r=-0.358$, $p=0.008$) and kurtosis_{ct_ssf_4} ($r=-0.263$, $p=0.010$).

Multivariate analysis showed that entropy_ct_ssf_2 coupled with SUV biomarkers stratifies survival when there are mutations present.

6.1.4 Conclusion

The findings suggest that there are complex relationships between the imaging biomarkers and the pathological markers, however, they are interesting and suggest targetted studies with a larger population may be successful in demonstrating multivariate predictors.

6.2 Introduction

Lung cancers are classified histopathologically by cellular and molecular subtypes using the 2021 World Health Organization (WHO) classification system (15). The three main subtypes of non-small cell lung cancer are: adenocarcinoma (40%), squamous-cell carcinoma (25%) and large cell carcinoma (10%). Subtypes are determined using cytology and immunohistochemistry staining, with immunohistochemistry staining playing a pivotal role in most classifications (9, 15).

Immunohistochemical staining, however, is not limited to subtype classification, as assays can be used to detect pharmaceutical targetable mutations or evaluate the cellular localisation and the context of tumour structures. These assays can then inform prognosis and treatment. Nevertheless, not all mutations can be detected reliably through staining, and molecular testing with mutation analysis sequencing may be required.

The most common mutations in non-small cell lung cancer have been shown to be EGFR, KRAS and FGFR1 however expression of mutations differs by subtype (206–208). Whilst not all mutations have targeted therapy, several mutations do have and therefore guidelines exist for the molecular testing of lung cancers (207, 208). These guidelines suggest a molecular testing approach that is supported by studies in to tyrosine-kinase inhibitor effectiveness and immunomodulator effectiveness. This of course means that mutations which are associated with poor prognosis but do not have effective targeted treatments are not recommended by this guideline and as a result these guidelines make no recommendation for mutation analysis of squamous cell carcinomas. It also means that mutations are not analysed when the treatments have not shown to be effective.

The lack of a current effective treatment does not imply that there will never be an effective treatment. Nor does it imply that treatments could not be effective in subsets of patients, or become effective if other treatments change. Thus highly targeted guidelines to only test for markers with effective treatments may prevent recognition of subsets of patients in whom treatments would be or could be effective. Meanwhile,

these tests are expensive and require acquisition of tissues, most often from biopsies, and if they do not provide benefit for the patients themselves it is questionable if they should be performed.

Mutation analysis and immunohistochemical staining can only be performed on a small sample of the tumour, either from a biopsy or from whole resected sample. Tumour heterogeneity raises questions about the generalisability of the results from these samples (209–211), and it should also be noted that there is a risk of biopsy tract metastasis (212).

In the midst of this diagnostic dilemma, it is reasonable to ask if there would be a way in which mutations could be detected without the need for biopsy and expensive immunohistochemical marking and mutation analysis.

Further, if these mutations are associated with prognosis, it would be reasonable to investigate whether they cause structural changes that could be assessed on imaging: indeed, such changes may perhaps be expected. If there exists a characteristic signature that would suggest specific mutations or collections of mutations, that would allow one to target additional mutation analysis to these patients. In fact, several studies have suggested that relationships like this do appear; however, repeatability of these studies appears poor (211, 213–216).

In this chapter, the following immunohistochemical biomarkers were assessed: Inflammation, CA-IX (hypoxia), CD105 (vasculature), GLUT1 (glucose metabolism/hypoxia), HIF-1 α (hypoxia), MCM2 (genetic stability), and VEGF (vasculature). The following tumour promoting oncogenes were also assessed: BRAF, EGFR, HER2, KRAS, and PI3KCA.

6.2.1 Inflammation

A tumour's micro-environment plays an important role in tumour growth, invasion and metastasis. In particular, a close relationship has been shown between inflammation and lung cancer, and some reports suggest intervention in the inflammatory micro-environment can reduce the development of lung cancer (217–219).

6.2.2 CA-IX

Carbonic anhydrase IX (CA-IX) is a surface-expressed enzyme upregulated by hypoxia during tumour development and progression. The enzyme catalyses the hydration of cell-generated carbon dioxide into hydrogen and bicarbonate ions. This helps tumour cells to survive hypoxia (220).

6.2.3 CD105

CD105, also known as endoglin, is a cell-surface glycoprotein, involved in the development of blood vessels and represents a specific neovascularization marker indicating proliferation of human endothelial cells. It is a receptor for transforming growth factor TGF- β 1 and TGF- β 3, modulating TGF- β signalling by interacting with TGF- β R-I and/or -II (187, 221–223).

6.2.4 GLUT1

Although there are multiple types of transmembrane glucose transporters, the type-1 transporter (GLUT1) is the main glucose transporter implicated in lung cancer. Its overexpression has been associated with poor prognosis and is thought to help promote glycolysis, especially that associated with the Warburg effect, thence promote tumourigenesis and progression (224).

6.2.5 HIF-1 α

Hypoxia-inducible factor (HIF)-1 is a transcription factor consisting of two subunits: α and β . The HIF-1 α subunit is rapidly degraded in the presence of Oxygen and thus acts as the regulatory subunit. HIF-1 causes the transcription of a number of genes including Erythropoietin, CA-IX and GLUT-1. HIF-1 α has been found to be widely expressed in solid tumours and associated with both improved and worsened prognosis (225–227).

6.2.6 MCM2

MCM2 is a member of the minichromosome maintenance protein family. These proteins are essential components for DNA replication regulating transcription, chromatin remodelling and checkpoint responses. Various studies have shown that MCM proteins can act as markers of dysplasia and malignancy, and be prognostic

markers. In particular increased MCM2 expression has previously been shown to be associated with an increased risk of death in lung cancer (228–230).

6.2.7 VEGF

Vascular Endothelial Growth Factor (VEGF) plays a central role in angiogenesis and promotes endothelial cell proliferation, migration and invasion. Additionally, it increases vascular permeability and extravasation, and some evidence suggests that it can directly induce tumour cell growth and metastasis alongside that of the angiogenesis effect (231, 232). Overexpression and high serum levels of VEGF have been reported in lung cancer and are associated with poor prognosis. However, although drugs targeting VEGF and its receptors have been approved, these have only shown modest improvements in survival (232).

6.2.8 BRAF

The BRAF (B-Rapidly Accelerated Fibrosarcoma) gene is on chromosome 7 and encodes for the B-Raf (B-Rapidly Accelerated Fibrosarcoma) protein. The B-Raf protein is a member of the Raf (Rapidly Accelerated Fibrosarcoma) kinase family of growth signal transduction protein kinases and plays a role in regulating the MAPK/ERKs (Mitogen-activated Protein Kinase/Extracellular signal-related Protein Kinase) signalling pathway. Thus, it regulates cell division, differentiation and secretion. Mutations in this gene can lead to permanent activation or upregulated activation of the protein and hence unregulated cell growth and division. Mutations in BRAF have been widely observed across multiple cancers but has been seen in up to 3% of lung cancer (14, 210, 233).

6.2.9 EGFR

The EGFR gene is also on chromosome 7 and encodes for the epidermal growth factor receptor (EGFR) protein. This protein is a transmembrane protein acting as a receptor tyrosine-kinase for members of the epidermal growth factor family of ligands. When activated, EGFR causes activation of a number of signalling cascades including the MAPK/ERKs pathway and the PI3K/AKT (Phosphatidylinositol 3-Kinase/Ak strain transforming also known as Protein kinase B) pathway. Mutations within the gene can lead to permanent activation of the receptor and hence unregulated growth driven by

multiple cascades. In lung cancer, patients with EGFR mutations may benefit from treatment with EGFR antagonists such as erlotinib or gefitinib (14, 207, 208).

6.2.10 HER2

The HER2 (Human Epidermal Growth Factor Receptor 2) gene on chromosome 17 similarly encodes for a transmembrane receptor tyrosine-kinase, this receptor binds epidermal growth factor ligands and activates a number signalling cascades. Mutations within the gene can similarly lead to permanent activation of the receptor and upregulation of the downstream signalling pathways. Although HER2 mutations are most commonly associated with breast cancer and treatments have been approved there, HER2 mutations has been reported in up to 4% lung cancer cases (210, 233).

6.2.11 KRAS

The KRAS (Kirsten Rat Sarcoma Virus) gene encodes for the K-Ras (Kirsten Rat Sarcoma Virus) protein, which is a part of the RAS/MAPK (Rat Sarcoma Virus protein/Mitogen-activated protein kinase) signalling pathway. Mutations within the gene can lead to permanent activation of the protein and hence unregulated growth driven by this pathway. In lung cancer, mutations in KRAS and EGFR are generally mutually exclusive and so a mutation in KRAS predicts poor response to EGFR antagonists such as erlotinib or gefitinib (14, 208, 233).

6.2.12 PI3KCA

The PIK3CA (Phosphatidylinositol-4,5-bisphosphate 3-kinase catalytic subunit alpha) gene on chromosome 3 encodes for a catalytic subunit of the Phosphatidylinositol 3-kinase (PI3K) protein. A mutation in PIK3CA that causes permanent or increased activation of the catalytic protein will lead to upregulated and unregulated signalling on the PI3K/Akt pathway, leading to increased cellular proliferation and survival. Mutations in this gene have been found in around 4% of lung cancer cases, and can co-occur with mutations in EGFR and KRAS amongst others (15, 206–208, 210, 216).

The aim of this study is therefore to assess if there are statistically significant relationships, and the strength of these relationships, between imaging biomarkers and

selected immunohistochemical markers and mutations in NSCLC in the dataset. Multivariate survival analysis was performed with mutation status and imaging biomarkers to suggest prognostic associations with tissue biomarkers.

6.3 Materials and Methods

6.3.1 Patient Population

The population of patients is as described in detail in Section 2.2 and Section 2.10.

6.3.2 ^{18}F -FDG-PET/CT Imaging Protocol

The ^{18}F -FDG-PET/CT imaging protocol is described in detail in Section 2.3.

6.3.3 ^{18}F -FDG-PET/CT Image Analysis

The ^{18}F -FDG-PET/CT image analysis protocol is described in detail in Section 2.4.

6.3.4 Textural Analysis

The TexRAD image analysis protocol is described in detail in Section 2.9.

6.3.5 CT Perfusion Imaging Protocol

The CT perfusion imaging protocol is described in detail in Section 2.6.

6.3.6 CT Perfusion Image Analysis

The CT perfusion image analysis protocol is described in detail in Section 2.7.

6.3.7 Immunohistochemistry

The immunohistochemistry protocol is described in detail in Section 2.11.

6.3.8 Mutation Analysis

The mutation analysis protocol is described in detail in Section 2.12.

6.3.9 Statistical Analysis

Statistical and data analysis is described in detail in Section 2.13.

6.4 Results

6.4.1 Patient Demographics

Of the 484 patients, 475 patients had ^{18}F -FDG-PET/CT imaging and a total of 293 patients were determined to have NSCLC, (133 were determined to benign.)

Of these 293 patients 147 went on to have surgery and 96 of these patients went on to have successful mutation analysis performed. 54 of these patients were male and 42 were female. The median age at enrolment was 68 years (interquartile range 61–74 years). 58 (60%) of these patients were Stage I, 16 (17%) Stage II, 19 (20%) Stage III and 3 (3.1%) Stage IV.

SUV_{max} , SUV_{peak} , and TBR_{lung} were all statistically significantly different between male and female patients which may relate to the statistically significant higher rates of Squamous-cell carcinoma (SCC) within the male group. (21 male patients (39%) versus 8 female patients (19%), $p=0.036$). (See Table 24.)

6.4.2 Inflammation

Of the 90 biomarkers looked at, four were statistically significantly correlated with Inflammation at $p<0.05$ with 2 at $p<0.01$. CTP4 mean slope of increase was negatively correlated with Inflammation ($r=-0.442$, $p=0.021$) and sd_ct_ssf_0 was statistically correlated with Inflammation ($r=0.361$, $p=0.007$). (See Table 25, Figure 12 and 13.)

6.4.3 CA-IX

There were 4 biomarkers that were statistically significantly correlated with CA-IX expression at $p<0.05$. The most significant result was a negative correlation with CTP4 PS ($r=-0.350$, $p=0.01$). (See Table 26, Figure 12 and 13.)

6.4.4 CD105

There were 12 biomarkers that were statistically significantly correlated with CD105 expression at $p<0.05$. kurtosis_ct_ssf_3 was the most significant correlation ($r=0.356$, $p=0.012$). (See Table 27, Figure 12 and 13.)

6.4.5 GLUT1

Thirty biomarkers were statistically significantly correlated with GLUT1 expression at $p < 0.05$ with 15 of these at $p < 0.001$. (See Table 29, Figure 12 and 13.) All of the SUV measures and TBR_{lung} demonstrated moderate ($0.400 \leq r < 0.600$) positive correlations with GLUT1 expression and there were weak ($0.200 \leq r < 0.400$) positive correlations with the textural entropy measures.

6.4.6 HIF-1 α

Nine biomarkers were statistically significantly correlated with HIF-1 α expression at $p < 0.05$. (See Table 28, Figure 12 and 13.) Of these, the most significant was a negative correlation with CTP4 time to peak ($r = -0.312$, $p = 0.023$).

6.4.7 MCM2

Twelve biomarkers were statistically significantly correlated with MCM2 expression at $p < 0.05$ with five at $p < 0.001$. (See Table 30, Figure 12 and 13.) Of these, the most significant was a moderate correlation with SUV_{min} ($r = 0.403$, $p < 0.01$) but there were significant correlations with the other SUV biomarkers.

6.4.8 VEGF

There were no statistically significant correlations with VEGF expression.

6.4.9 BRAF

Ten biomarkers were statistically significant correlated with BRAF mutations at $p < 0.05$. (See Table 31, Figure 12 and 13.) There were negative correlations with textural entropy scores: the most significant was entropy_ct_ssf_2 ($r = -0.220$, $p = 0.032$).

6.4.10 EGFR

Twenty biomarkers were statistically significant correlated with EGFR mutations at $p < 0.05$. (See Table 32, Figure 12 and 13.) The were most significant were negative correlations with textural kurtosis_ct_ssf_2 ($r = -0.293$, $p = 0.004$), kurtosis_pet_ssf_5 ($r = -0.293$, $p = 0.004$) and kurtosis_pet_ssf_6 ($r = -0.289$, $p = 0.004$).

6.4.11 HER2

Three biomarkers were statistically significant correlated with HER2 mutations at $p < 0.05$. (See Table 33, Figure 12 and 13.) There were negative correlations with textural skewness_ct_ssf_4 ($r = -0.216$, $p = 0.034$), skewness_ct_ssf_3 ($r = -0.256$, $p = 0.012$) and skewness_pet_ssf_0 ($r = -0.209$, $p = 0.041$).

6.4.12 KRAS

Four biomarkers were statistically significant correlated with KRAS mutations at $p < 0.05$. (See Table 34, Figure 12 and 13.) There were negative correlations with textural skewness_pet_ssf_3 ($r = -0.205$, $p = 0.045$), kurtosis_pet_ssf_2 ($r = -0.240$, $p = 0.018$), kurtosis_pet_ssf_4 ($r = -0.222$, $p = 0.029$) and kurtosis_pet_ssf_3 ($r = -0.245$, $p = 0.016$).

6.4.13 PI3KCA

Six biomarkers were statistically significant correlated with PI3KCA mutations at $p < 0.05$. (See Table 35, Figure 12 and 13.) The most significant was a negative correlation with CTP4 average ($r = -0.256$, $p = 0.008$).

6.4.14 No Mutation Detected

There were no statistically significant correlations.

6.4.15 Multivariate and Univariate Survival Analysis

For most mutations, entropy_ct_ssf_2 & SUV_{peak} worked synergistically to stratify patients into low, medium and high risk groups. In patients who had no mutation detected, only $SUV_{mean} > 7.2$ acted as a statistically significant prognosticator. (See Table 36.)

6.5 Discussion

This prospective study has demonstrated a number of statistically significant associations between immunohistochemical/mutation status and imaging biomarkers. Investigating associations between imaging features and imaging biomarkers, and mutations and immunohistochemical expression, is a critical step in radiogenomics (234). Recognising the effect that mutations and immunohistochemical markers have on the imaging phenotype helps further understanding of the role of these factors and could provide impetus to suggest repeated biopsy or even that biopsies should be avoided in the case of a non-response to therapy or non-phenotypic appearance.

The most significant and strongest association we have found is a moderate correlation between SUV and SUV dependent markers and the GLUT1 immunohistochemical marker. This replicates the findings of a previous cross-tumour study in 2019 (235), and the correlation found is not significantly different from those findings. This may suggest that GLUT1 hyperexpression is important component of glucose hypermetabolism and the Warburg effect in lung cancer, whilst not completely explaining glucose hypermetabolism. The moderate association is stronger than that recently demonstrated in breast cancer and suggests that GLUT1 hyperexpression plays a greater role in lung cancer than in breast cancer (186).

The correlations between the SUV biomarkers, some textural biomarkers and CD105 are similar to but slightly weaker than those found recently in breast cancer (186). This relatively reduced correlation raises the possibility that lung cancer may respond differently to hypoxia than breast cancer, preferring GLUT1 hyperexpression and the Warburg effect to increase metabolism.

If GLUT1 hyperexpression were as a consequence of hypoxia, HIF-1 α could help demonstrate that. HIF-1 α is an important upregulator of GLUT1 expression and a marker of hypoxia. Although there was a weak relationship between the textural entropy biomarkers and HIF-1 α and GLUT1, there is not a significant relation between the SUV biomarkers and HIF-1 α . It should also be noted that HIF-1 α is highly unstable and thus levels of HIF-1 α detected in our samples may be artificially low. The error this

instability causes in our measurements of HIF-1 α may be related to both age of sample and the amount of HIF-1 α in the sample, and therefore may represent a non-constant non-linear error making it difficult to interpret our results.

Another possible interpretation for the difference in the strength of the correlations between CD105 and SUV versus GLUT1 and SUV is that our tumours are less affected by hypoxia than the tumours in the breast study. As a consequence of the biases within the dataset, our tumours tend to be relatively small tumours, and on account of the anatomy are likely to have a relatively good blood supply (likely even a dual blood supply). Assuming that this is the case, the tumours may be not be particularly hypoxic and hence there would be a reduced evolutionary drive towards angiogenesis. These tumour cells may be hyperexpressing GLUT1 and undergoing the Warburg effect in a non-hypoxia dependent fashion as a way of increasing metabolism if the Krebs cycle is saturated. In such an environment, tumour cells with higher GLUT1 expression would likely be more evolutionarily fit and then form the majority of the tumour.

Minichromosome maintenance complex component 2 (MCM2) is involved in the initiation of eukaryotic genome replication and thus is a marker of cell replication. The statistically significant correlations found between the SUV biomarkers suggest that higher SUV is at least partially associated with increased cell-replication.

The significant but weak-to-moderate negative association between the CTP4 average measure and PI3KCA implies that, of the surgical cases that had CT Perfusion performed, those that were denser and enhanced more over the study were less likely to have PI3KCA mutation. It is difficult to tease out the effect of contrast enhancement versus higher overall attenuation here but it is likely that this is more likely to represent contrast enhancement. This is an interesting finding and it raises the question of if the findings could be replicated on standard contrast-enhanced CT images and whether this may indicate that PI3KCA mutations result in tumours which demonstrate lower enhancement and hence are less likely to demonstrate angiogenesis. There are several PIK/Akt/mTOR inhibitor therapy drug candidates and clinical trials (236, 237): if there were an imaging biomarker that could predict the presence of PI3KCA mutations, the

effectiveness of these therapies could be monitored by the change on the tumour imaging signature.

The weak negative correlations found for the rest of tumour mutations markers suggests the radiologic-pathologic correspondence for these is complex 2014 — most of the associated imaging biomarkers here were also related to survival, suggesting that these may be survival correlates rather than correlates with the mutation per se. It should also be noted that many of the mutations considered here upregulate similar downstream pathways, so the correlations may be indirect and represent correlations between the imaging biomarkers and the upregulated pathways. Whilst such a correlation would not necessarily be as helpful as the ability to detect specific mutations, such a biomarker could still help monitor therapy or help target mutation and immunohistochemical analysis. It could also help further elucidate how mutations and receptor upregulation affect these pathways *in vivo* as opposed to *in vitro*.

The correlations discussed above are of interest; however, the use of multiple imaging biomarkers together has the potential to investigate imaging histological relationships further. Previous studies have suggested that imaging biomarkers could be combined to predict KRAS mutation status in colorectal cancer and in lung cancer using a decision tree analysis (238–240). An alternative is to investigate how histology can be combined with imaging biomarkers to stratify in to risk groups for survival prognostication. This study has shown that entropy_ct_ssf_2 can be combined with several ¹⁸F-FDG uptake measurements to further stratify patients with mutations in to at-risk groups.

The population of this study is biased by the requirement for surgical pathology. Even within a large population of recruited lung cancer patients such as this in this study, only a relatively small population of patients go on to have surgery and thence available tissue. Thus, compared to pathology only studies our population size is limited and there is less statistical power available to tease out correlations.

Nonetheless, by imaging tissue standards, this is a relatively large cohort with a long follow-up. As such it provides an original dataset. Higher numbers of patients may be achieved by using biopsy specimens rather than surgical specimens. Other limitations

related to imaging parameter extraction as discussed in other chapters e.g. respiratory motion still apply.

Only one example of multivariate analysis was performed as an example. In reality there are many combinations that could be explored. An artificial intelligence methodology could be explored here but is beyond the scope of this theses. This could be a topic of research to be taken forward into the future.

6.6 Conclusion

This study has demonstrated that there some correlations between imaging biomarkers and the immunohistochemical and mutation biomarkers, some of which were highly significant. In particular, the correlations found between imaging biomarkers and GLUT1 and CD105 give potentially tantalising *in vivo* insights into tumour metabolism, hypoxia and vascularity. These techniques have significant prognostic and predictive potential and further large studies applied to lung-cancer treatment studies may prove this.

6.7 Tables

Gender	Overall, N = 96	Female, N = 42	Male, N = 54	p-value ¹
Age at Enrolment				0.14
N	96.0	42.0	54.0	
Median (IQR)	68.0 (61.0, 74.0)	66.0 (60.0, 73.0)	70.0 (63.0, 75.0)	
Range	49.0, 90.0	49.0, 88.0	51.0, 90.0	
Radiological Stage, n (%)				>0.99
I	58 (60)	26 (62)	32 (59)	
II	16 (17)	7 (17)	9 (17)	
III	19 (20)	8 (19)	11 (20)	
IV	3 (3.1)	1 (2.4)	2 (3.7)	
SUV_{max}				0.024
N	96.0	42.0	54.0	
Median (IQR)	8.7 (4.7, 14.2)	7.1 (4.0, 12.3)	11.2 (6.6, 15.5)	
Range	0.8, 37.9	1.0, 27.0	0.8, 37.9	
TBR_{lung}				0.003
N	96.0	42.0	54.0	
Median (IQR)	27.9 (15.6, 47.5)	20.4 (12.3, 37.5)	40.4 (19.7, 55.8)	
Range	2.7, 139.0	2.8, 135.0	2.7, 139.0	
SUV_{mean}				0.033
N	96.0	42.0	54.0	
Median (IQR)	5.2 (2.8, 8.7)	4.2 (2.4, 7.5)	6.8 (4.0, 9.5)	
Range	0.6, 24.1	0.8, 16.3	0.6, 24.1	
SUV_{peak}				0.028
N	96.0	42.0	54.0	
Median (IQR)	7.2 (3.5, 11.9)	5.2 (2.8, 9.4)	9.1 (5.1, 12.0)	

Gender	Overall, N = 96	Female, N = 42	Male, N = 54	p-value ¹
Range	0.7, 32.7	0.9, 24.1	0.7, 32.7	
TLG				0.050
N	96.0	42.0	54.0	
Median (IQR)	24,511.1 (9,859.3, 92,357.7)	14,754.3 (5,311.7, 109,469.7)	32,926.6 (15,123.7, 87,968.6)	
Range	829.6, 1,822,757.4	829.6, 392,145.4	1,899.6, 1,822,757.4	
SCC, n (%)	29 (30)	8 (19)	21 (39)	0.036

¹Wilcoxon rank sum test; Fisher's exact test; Pearson's Chi-squared test

Table 24: Patient demographics as compared to gender

Inflammation	Spearman's Rho ¹	p-value
CTP4 mean slope of increase	-0.442	0.021
sd_ct_ssf_2	0.355	0.008
sd_ct_ssf_0	0.361	0.007
mpp_ct_ssf_2	0.310	0.022

¹Spearman's rank correlation rho with pairwise complete observations

Table 25: Significant correlations with inflammation

CA-IX	Spearman's Rho ¹	p-value
CTP4 positive enh. integral	-0.301	0.028
CTP4 ps	-0.350	0.010
mpp_pet_ssf_2	-0.221	0.035
mpp_pet_ssf_3	-0.229	0.028

¹Spearman's rank correlation rho with pairwise complete observations

Table 26: Significant correlations with CA-IX

CD105	Spearman's Rho ¹	p-value
SUV_{max}	0.308	0.032
SUV_{min}	0.305	0.033
SUV_{mean}	0.298	0.037
SUV_{peak}	0.318	0.026
kurtosis_ct_ssf_4	0.287	0.045
kurtosis_ct_ssf_3	0.356	0.012
entropy_pet_ssf_2	0.345	0.015
entropy_pet_ssf_4	0.343	0.016
entropy_pet_ssf_6	0.346	0.015
entropy_pet_ssf_0	0.347	0.015
entropy_pet_ssf_3	0.344	0.015
entropy_pet_ssf_5	0.344	0.016

¹Spearman's rank correlation rho with pairwise complete observations

Table 27: Significant correlations with CD105

HIF-1 α	Spearman's Rho ¹	p-value
CTP4 time to peak	-0.312	0.023
CTP4 mean slope of increase	0.302	0.028
skewness_ct_ssf_3	0.224	0.034
entropy_pet_ssf_2	0.231	0.029
entropy_pet_ssf_4	0.223	0.035
entropy_pet_ssf_6	0.226	0.032
entropy_pet_ssf_0	0.224	0.034
entropy_pet_ssf_3	0.220	0.037
entropy_pet_ssf_5	0.220	0.037
entropy_pet_ssf_3	0.344	0.015

¹Spearman's rank correlation rho with pairwise complete observations

Table 28: Significant correlations with HIF-1 α

GLUT1	Spearman's Rho ¹	p-value
SUV _{max}	0.441	<0.001
SUV _{min}	0.436	<0.001
SUV _{mean}	0.429	<0.001
SUV _{peak}	0.440	<0.001
TBR _{lung}	0.471	<0.001
TLG	0.365	<0.001
mean_ct_ssf_2	-0.224	0.031
mean_ct_ssf_4	-0.254	0.014
mean_ct_ssf_6	-0.229	0.028
mean_ct_ssf_3	-0.266	0.010
mean_ct_ssf_5	-0.260	0.012
entropy_ct_ssf_2	0.380	<0.001
entropy_ct_ssf_4	0.336	0.001
entropy_ct_ssf_6	0.349	0.001
entropy_ct_ssf_0	0.301	0.003
entropy_ct_ssf_3	0.357	<0.001
entropy_ct_ssf_5	0.361	<0.001
kurtosis_ct_ssf_2	0.264	0.011
kurtosis_ct_ssf_4	0.207	0.047
kurtosis_ct_ssf_0	0.213	0.040
kurtosis_ct_ssf_3	0.278	0.007
mean_pet_ssf_0	-0.220	0.034
sd_pet_ssf_0	0.215	0.039
entropy_pet_ssf_2	0.388	<0.001
entropy_pet_ssf_4	0.393	<0.001
entropy_pet_ssf_6	0.390	<0.001
entropy_pet_ssf_0	0.390	<0.001
entropy_pet_ssf_3	0.388	<0.001
entropy_pet_ssf_5	0.389	<0.001

GLUT1	Spearman's Rho ¹	p-value
mpp_pet_ssf_0	-0.220	0.034

¹Spearman's rank correlation rho with pairwise complete observations

Table 29: Significant correlations with GLUT1

MCM2	Spearman's Rho ¹	p-value
SUV_{max}	0.399	<0.001
SUV_{min}	0.403	<0.001
SUV_{mean}	0.392	<0.001
SUV_{peak}	0.362	<0.001
TBR_{lung}	0.376	<0.001
TLG	0.231	0.025
CTP4 average	0.324	0.018
mean_pet_ssf_0	-0.286	0.005
mpp_pet_ssf_0	-0.286	0.005
mpp_pet_ssf_3	0.212	0.040
kurtosis_pet_ssf_2	0.257	0.012
kurtosis_pet_ssf_3	0.219	0.034
kurtosis_pet_ssf_3	0.219	0.034

¹Spearman's rank correlation rho with pairwise complete observations

Table 30: Significant correlations with MCM2

BRAF	Spearman's Rho ¹	p-value
entropy_ct_ssf_2	-0.220	0.032
entropy_ct_ssf_6	-0.211	0.039
entropy_ct_ssf_0	-0.219	0.032
entropy_ct_ssf_5	-0.212	0.038
entropy_pet_ssf_2	-0.217	0.034
entropy_pet_ssf_4	-0.215	0.035
entropy_pet_ssf_6	-0.215	0.036
entropy_pet_ssf_0	-0.215	0.036
entropy_pet_ssf_3	-0.215	0.036
entropy_pet_ssf_5	-0.215	0.036

¹Spearman's rank correlation rho with pairwise complete observations

Table 31: Significant correlations with BRAF mutation status

EGFR	Spearman's Rho ¹	p-value
mean_ct_ssf_0	-0.202	0.048
kurtosis_ct_ssf_2	-0.293	0.004
kurtosis_ct_ssf_4	-0.225	0.028
kurtosis_ct_ssf_0	-0.246	0.016
kurtosis_ct_ssf_3	-0.208	0.042
kurtosis_ct_ssf_5	-0.239	0.019
entropy_pet_ssf_2	-0.255	0.012
entropy_pet_ssf_4	-0.257	0.012
entropy_pet_ssf_6	-0.260	0.011
entropy_pet_ssf_0	-0.256	0.012
entropy_pet_ssf_3	-0.257	0.012
entropy_pet_ssf_5	-0.256	0.012
skewness_pet_ssf_4	-0.208	0.042
skewness_pet_ssf_6	-0.226	0.027
skewness_pet_ssf_5	-0.229	0.025
kurtosis_pet_ssf_2	-0.203	0.047
kurtosis_pet_ssf_4	-0.255	0.012
kurtosis_pet_ssf_6	-0.289	0.004
kurtosis_pet_ssf_3	-0.229	0.025
kurtosis_pet_ssf_5	-0.293	0.004

¹Spearman's rank correlation rho with pairwise complete observations

Table 32: Significant Correlations with EGFR mutation

HER2	Spearman's Rho ¹	p-value
skewness_ct_ssf_4	-0.216	0.034
skewness_ct_ssf_3	-0.256	0.012
skewness_pet_ssf_0	-0.209	0.041

¹Spearman's rank correlation rho with pairwise complete observations

Table 33: Significant Correlations with HER2 mutation

KRAS	Spearman's Rho ¹	p-value
skewness_pet_ssf_3	-0.205	0.045
kurtosis_pet_ssf_2	-0.240	0.018
kurtosis_pet_ssf_4	-0.222	0.029
kurtosis_pet_ssf_3	-0.245	0.016

¹Spearman's rank correlation rho with pairwise complete observations

Table 34: Significant Correlations with KRAS mutation

PI3KCA	Spearman's Rho ¹	p-value
CTP4 average	-0.358	0.008
kurtosis_ct_ssf_4	-0.263	0.010
kurtosis_ct_ssf_3	-0.236	0.021
kurtosis_ct_ssf_5	-0.228	0.025
sd_pet_ssf_0	-0.261	0.010
mpp_pet_ssf_2	-0.213	0.037

¹Spearman's rank correlation rho with pairwise complete observations

Table 35: Significant Correlations with PIK3CA mutation

<i>p-value</i>	HER2 WT	HER2 mutation	EGFR mutation	EGFR WT	KRAS mutation	BRAF WT	Any Mutation	All WT
Univariate								
CT Entropy SSF2 (Median value 5.19 as cut-off)	0.034				0.022			
PET SUV Peak (Median value 9.65 as cut-off)			0.007		0.033		0.024	
PET TBR (Median value 41.5833 as cut-off)		0.010	0.007		0.023		0.003	
PET SUV Avg (Median value 7.2 as cut-off)			0.007		0.033			0.033
PET SUV Max (Median value 12 as cut-off)			0.007		0.033			
Combination								
CT Entropy SSF2 + PET SUV Peak	0.029		0.018	0.021	0.011	0.018	0.010	
CT Entropy SSF2 + PET TBR	0.018		0.018			0.033		
CT Entropy SSF2 + PET SUV Avg		0.024	0.018		0.011		<0.001	
CT Entropy SSF2 + PET SUV Max		0.024	0.018		0.011		<0.001	

Table 36: p-values from Kaplan Meier survival analysis demonstrating the ability of CT entropy and PET uptake biomarkers to stratify patients by prognosis

6.8 Figures

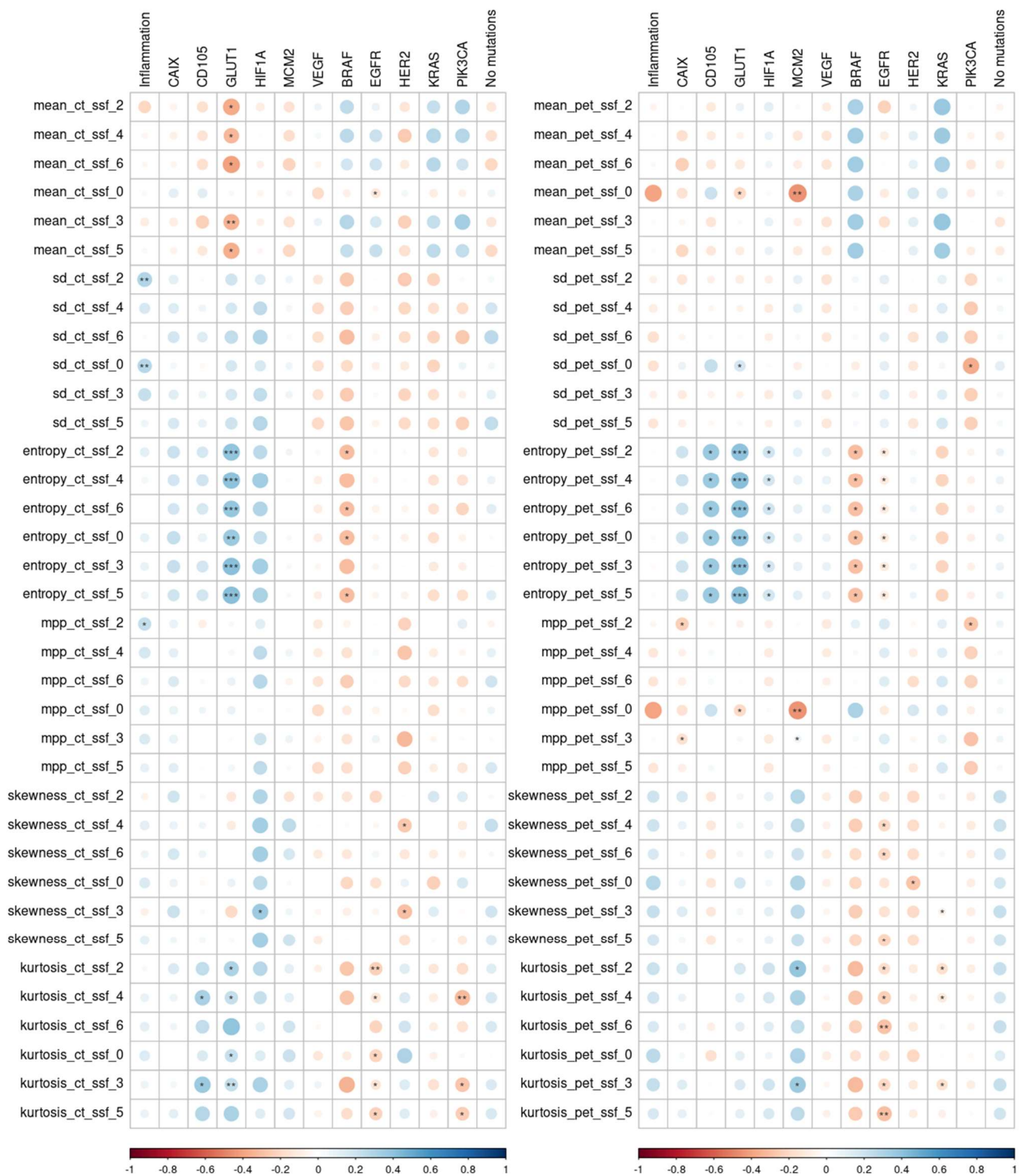


Figure 12: Correlations between TexRAD biomarkers, Immunohistochemistry and mutation analysis

*, **, *** denotes significance at $p=0.05$, 0.01 , and 0.001 respectively

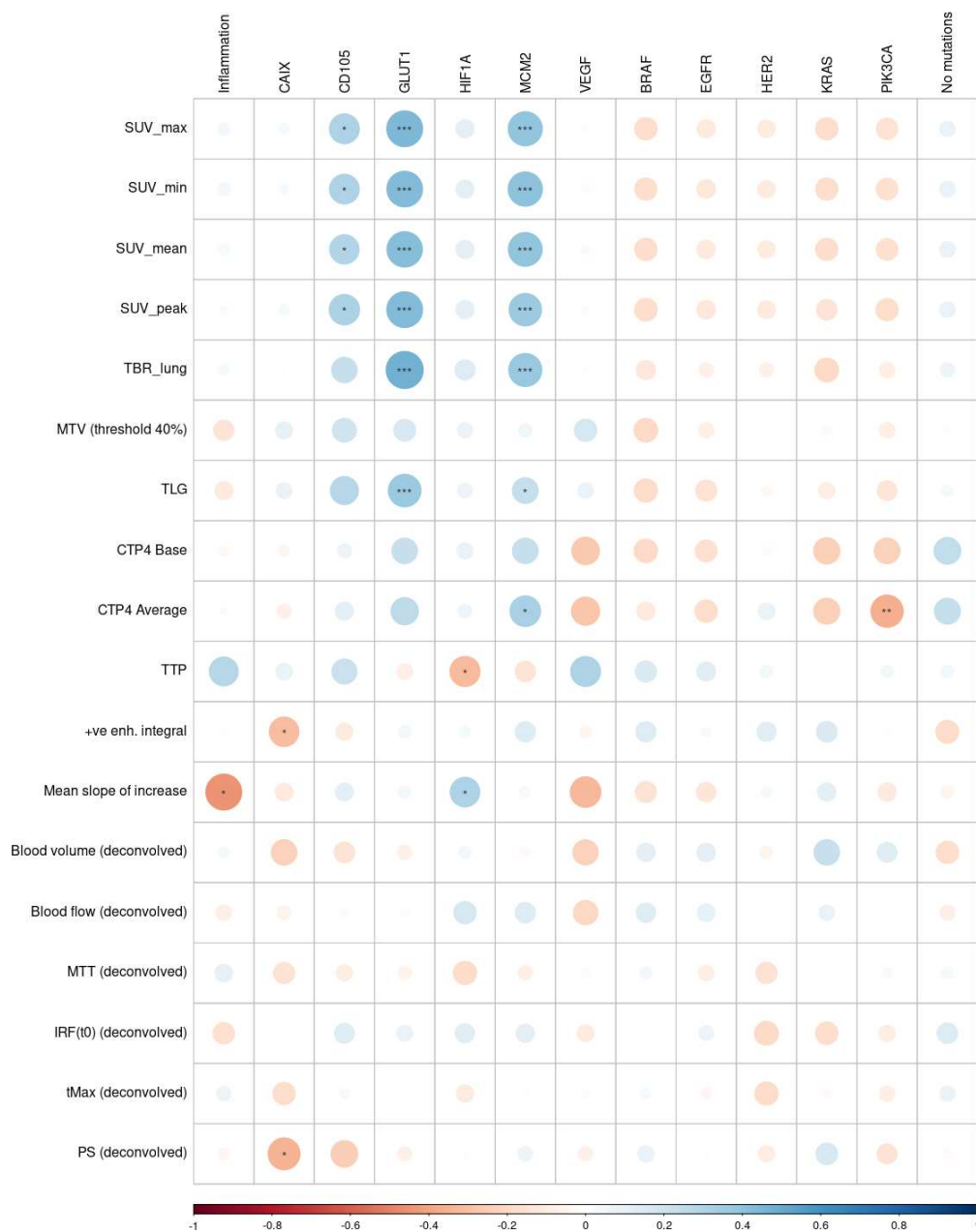


Figure 13: Correlations between PET and CTP4 biomarkers and Immunohistochemistry and mutation analysis.

*, **, *** denotes significance at $p=0.05$, 0.01 , and 0.001 respectively

7 Evolution of ^{18}F -FDG-PET/CT Findings in Patients Following COVID-19: An Initial Investigation

7.1 Abstract

7.1.1 Purpose

The aim of this chapter was to study the temporal-evolution of pulmonary ^{18}F -FDG-uptake in patients with Coronavirus Disease (COVID-19) and in Post-COVID-19 Lung-Disease (PCLD).

7.1.2 Methods

Using our hospital's clinical electronic records we retrospectively identified 23 Acute COVID-19, 18 PCLD and 9 completely recovered ^{18}F -FDG-PET/CT studies during the two peaks of UK pandemic. Pulmonary ^{18}F -FDG-uptake was measured as a Target-to-Background Ratio ($\text{TBR}_{\text{lung}} = \text{SUV}_{\text{max}} / \text{SUV}_{\text{min}}$) and compared to temporal stage.

7.1.3 Results

In acute COVID-19, less than three weeks after infection, TBR_{lung} was strongly correlated with time after infection ($r_s = 0.81$, $p < 0.001$) and was significantly higher in late-stage than early-stage ($p = 0.001$). In PCLD TBR_{lung} was lower in patients treated with high-dose steroids ($p = 0.003$) and asymptomatic patients ($p < 0.001$).

7.1.4 Conclusion

Pulmonary ^{18}F -FDG-uptake in COVID-19 increases with time after infection. In PCLD pulmonary ^{18}F -FDG-uptake rises despite viral clearance suggesting on-going inflammation. There was lower pulmonary ^{18}F -FDG-uptake in PCLD patients treated with steroids.

7.2 Introduction

During late February–Early March 2020, SARS-CoV-2 and its associated disease Coronavirus Disease 2019 (COVID-19) began spreading rapidly throughout London and the rest of the UK (25, 241, 242), following its emergence in December 2019 in Wuhan, China (23, 243). Although COVID-19 can remain essentially asymptomatic or have a large variety of clinical symptoms, COVID-19 is typically characterised by a bilateral interstitial pneumonia/viral pneumonitis of varying severity. Its severity may progressively worsen with symptoms of dyspnoea, tachypnoea, hypoxia and hypercapnia and the development acute respiratory distress syndrome (23, 26–35, 46, 244–246).

The median time from symptom-onset to intensive-care admission is 10 days, although only 5% of patients are admitted (23, 34–36, 247–250). The protracted clinical course, in contrast to the rapid course usually expected of viral diseases (35, 37, 249), and the timing at the peak of anti-viral response, suggests that the acute lung changes and damage may be a consequence of inflammation from the adaptive immune response rather than from the virus itself (35, 38).

On CT imaging, COVID-19 typically presents with ground-glass opacities (GGOs) and/or bilateral pulmonary consolidation in multiple segmental and subsegmental regions (26–33, 46, 244). In early stages, changes are often limited to peripheral GGOs and bronchovascular thickening. Consolidation and spread to the centre of the lungs happens later (26, 27, 30–33, 244, 246) with sub-pleural sparing and development of organising pneumonia occurring even later (26–28, 30–33, 244). Many other signs such as interlobular septal thickening and crazy paving have also been demonstrated (33, 39, 46) however, other typical pulmonary infection features — enlarged lymphadenopathy, pulmonary nodules, pleural effusions and cavitation — are not commonly demonstrated, except as features of other intercurrent disease e.g. heart failure (26). Lymphadenopathy, although not a common feature may be associated with prognosis (34). The findings are similar to those described with MERS-CoV and SARS-CoV-1 (26, 30, 47, 251).

Appearances in recovery are varied (39); however, persistent respiratory symptoms affect at least one-third of hospitalized patients, some of whom will have Post-COVID-19 Lung-Disease (PCLD) (42).

Steroids are critical in reducing mortality from COVID-19 but their role in PCLD is less clear and identifying those that might benefit may be difficult.

Currently, ^{18}F -Fluoro-2-deoxy-D-glucose (^{18}F -FDG) Positron Emission Tomography/Computed Tomography (PET/CT) has no role in the management of patients with COVID-19 (252) and there has been little investigation into the quantification and evolution of ^{18}F -FDG-uptake in COVID-19 (See Table 37). Given the growing role of ^{18}F -FDG-PET/CT in Interstitial Lung Diseases (ILD), the primary aim of this chapter was to assess the temporal-evolution of ^{18}F -FDG uptake in COVID-19, and correlate to clinical progression and recovery. A secondary aim was to investigate if steroids could alter this evolution.

7.3 Materials and Methods

7.3.1 Ethics

The Institutional Review Board approved this retrospective study and waived the requirement to obtain informed consent. The challenges of the pandemic constrained the methodological design necessitating a retrospective approach.

7.3.2 Patient Selection

All studies performed in the department over the first UK peak of the coronavirus pandemic (March–April 2020) and from September 2020–February 2021 (second-peak) were assessed for acute COVID-19 by following the British Society of Thoracic Imaging guidelines and/or a confirmed history of COVID-19 on the Electronic Health-Record System (EHRS) (29). This included some patients without positive Polymerase Chain Reaction (PCR) test results due to the poor availability of PCR tests in the early period. In addition, studies performed for persistent (symptoms persisting for greater than or equal to 4 weeks) respiratory symptoms, in keeping with PCLD, and those who had recovered from COVID-19 after the initial period were also included. Ongoing treatment with steroids and other immunosuppression was recorded. Formal lung function tests were not performed due to infection risks. Acute studies between May and September 2020 were not examined due to the low prevalence and incidence of COVID-19 in London during that time. (See Figure 17 and Table 38.)

7.3.3 ^{18}F -FDG-PET/CT Imaging Protocol

Patients were fasted for at least six hours and blood glucose levels were recorded prior to injection of 400MBq ^{18}F -FDG adjusted for weight in keeping with Administration of Radioactive Substances Advisory Committee guidelines (253). After an uptake time of 63.1 ± 10.9 minutes whole-body PET scans were acquired in a supine position with the arms above the head with two minutes per bed position using a General Electric (GE) Discovery-710 PET/CT scanner. A non-enhanced low-dose CT scan was acquired for anatomic co-registration and attenuation correction. Images were reconstructed using a resolution recovery iterative algorithm.

All images were reviewed by at least one dual accredited radiologist nuclear medicine physician. Quantification was performed by investigators with at least 10-years' experience of quantifying PET/CT images in diffuse lung disease. PET analysis was performed blind of clinical history and the CT analysis.

7.3.4 Determination of Temporal Stage

After radiological and EHRS review, the acute COVID-19 cases were assigned to two temporal groups: 'Early' or 'Late', following review of the available clinical history coupled with assessment of the CT components as per well-established findings (30): Early COVID-19 (approximately equating to ≤ 1 week after onset of disease) is defined as predominantly ground-glass opacities with or without associated interlobular thickening this progresses to Late COVID-19 (> 1 week after onset of disease to ≤ 4 weeks), with increasing consolidation and signs of resolution being marked by sub-pleural sparing, development of a fibrous-stripe and crescentic consolidation or reversed halo/atoll sign. Patients who were asymptomatic after 28 days were classed as recovered patients. In addition, patients who were imaged due to persistent symptoms after 28 days were described as having PCLD. The CT component was correlated with other cross-sectional imaging to reduce the likelihood of error of incorrect classification due to breathing artefact. Using this and clinical information from EHRS the number of days since disease onset was estimated.

7.3.5 Quantitative ^{18}F -FDG-PET Analysis

All images were processed using a standard protocol on a dedicated imaging workstation (ADW-volume-4.6 GE-Healthcare) calculated the lung Target-to-Background Ratio ($\text{TBR}_{\text{lung}} = \text{SUV}_{\text{max}} / \text{SUV}_{\text{min}}$) following the methods described previously (48, 49, 254).

7.3.6 Statistics

The difference in ^{18}F -FDG-PET uptake measures within the lung against temporal staging and pre-treatment with steroids were assessed using non-parametric Mann-Whitney test. Results were visualized using Box-and-Whisker plots. All statistical analyses were performed using SPSS-25.0.

7.4 Results

Of the 3112 ^{18}F -FDG-PET/CT studies screened 50 met the criteria for study entry, including 18 cases referred for ^{18}F -FDG-PET/CT for investigation of PCLD. Of the 50 cases (median age 61 range 18–87 years), 32 were male (64%), 27 patients were of ethnic minority background (54%): 23 (46%) cases were found to demonstrate acute COVID-19. None of these were intentionally imaged for COVID-19. 9 cases demonstrated asymptomatic recovered COVID-19 confirmed on the EHRS. (See Table 39–40.)

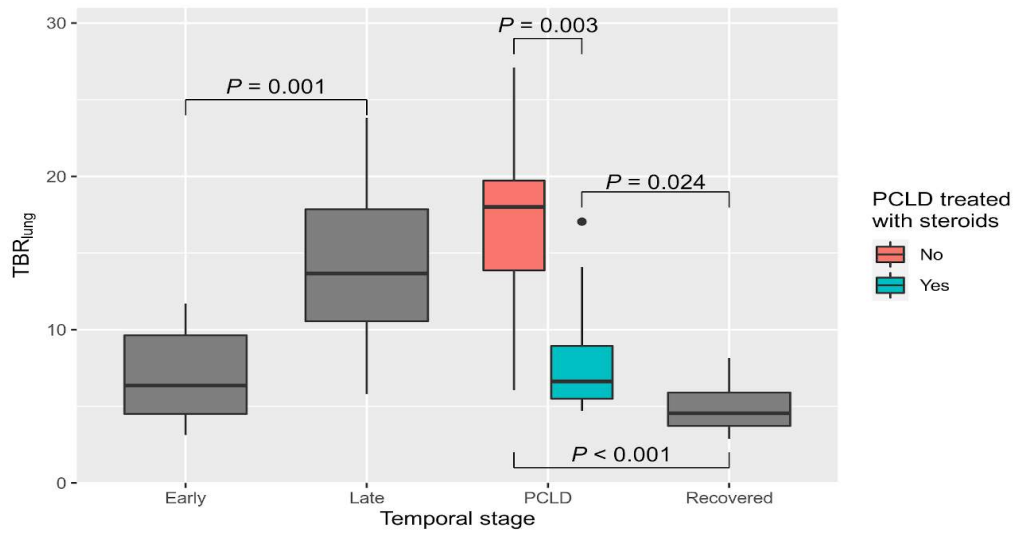
In the other 18 of the 50 cases imaging was performed because of persistent shortness of breath and respiratory symptoms in keeping with PCLD — all 18 had been admitted to hospital requiring oxygen. 15 of these patients previously had positive PCR tests and COVID-19 was clinically diagnosed in the others. 9 had ongoing treatment with steroids for PCLD, the other 9 were not receiving treatment for their PCLD. All PCLD patients had been re-swabbed prior to PET imaging and confirmed as PCR negative. (See Table 41.)

7.4.1 Temporal Stage

Following review of the attached CT component (lung windows) and available clinical history, of the 23 acute COVID-19 patients: 8 (35%) were determined to represent early COVID-19 and 15 (65%) late. (See Figure 12 and Table 41)

7.4.2 Association of Pulmonary ^{18}F -FDG-Uptake with Temporal-staging in Early & Late Stage Disease

^{18}F -FDG-uptake analysis of the lung lesions in the acute patients demonstrated increasing TBR_{lung} over time with the progression from low avidity ground-glass change to avid consolidation during the late phase (Median Early-stage: SUV_{max} 1.6, TBR_{lung} 6.4; Late-stage: SUV_{max} 4.0, TBR_{lung} 13.7). In the acute patients, TBR_{lung} was significantly different for late-stage patients having a higher TBR_{lung} than early stage patients ($p=0.001$, See



Figure

15.). Amongst these patients, a significant positive correlation was observed between TBR_{lung} and estimated time since onset, ($r_s=0.60$, $p=0.003$, See

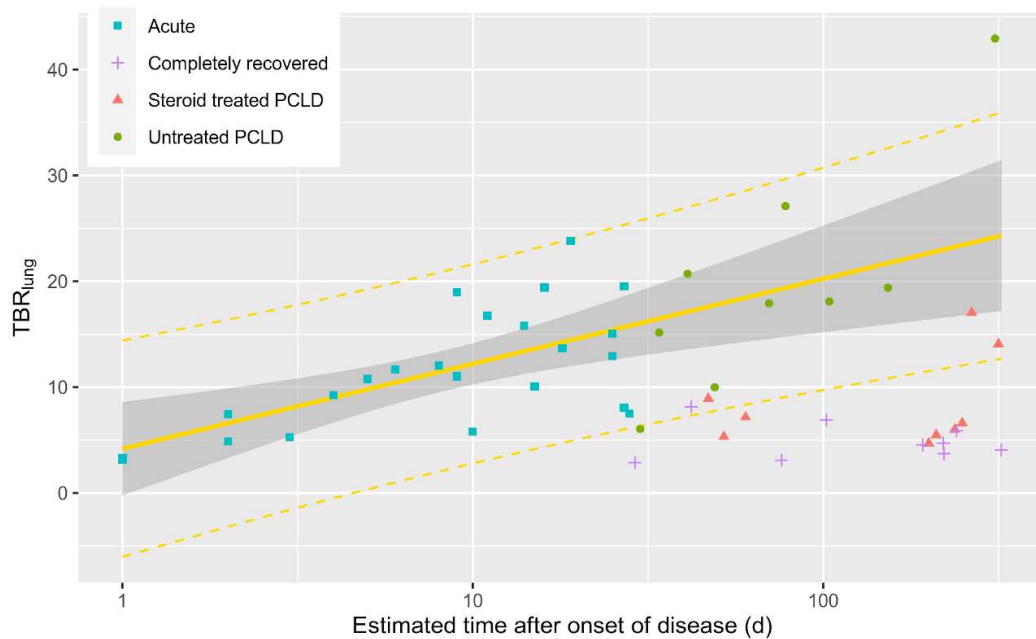
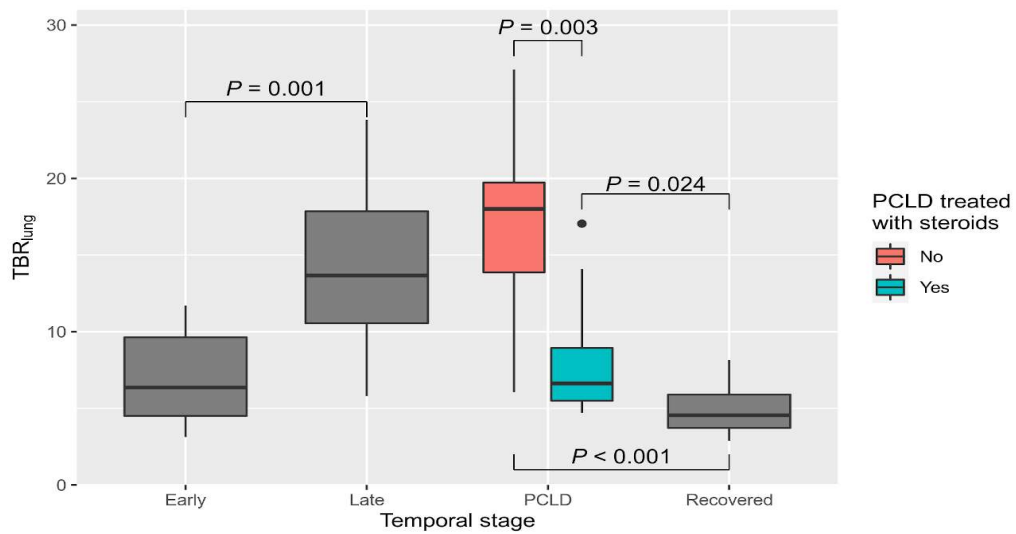


Figure 16.), this was stronger when limited to acute patients estimated to be in the first three weeks of infection ($n=18$, $r_s=0.81$, $p<0.001$).

7.4.3 Pulmonary ¹⁸F-FDG-Uptake in PCLD

There was lower TBR_{lung} in patients who had received treatment with high-dose steroids ($p=0.003$) (See



Figure

15.) (Median steroid-treated: SUV_{max} 2.4, TBR_{lung} 6.62; untreated: SUV_{max} 5.8, TBR_{lung} 18.1)

TBR_{lung} was lower in asymptotically recovered patients (median SUV_{max} 1.2, TBR_{lung} 4.6) than both untreated PCLD patients and those treated with steroids. ($p < 0.001$ and $p = 0.020$ respectively, Kruskal-Wallis for all 3 groups $p < 0.001$).

7.5 Discussion

This chapter represents the first attempt to characterise the evolution of pulmonary ^{18}F -FDG-uptake in a reasonably large cohort of patients with COVID-19 assigned a temporal stage (Early-to-Late-to-PCLD) based on clinical context and CT findings.

The increase of lung avidity with time suggests increasing lung inflammation (35, 255) in acute COVID-19. In most cases, ^{18}F -FDG uptake would then be expected to decrease with viral clearance and establishment of immunity. There is, however, a subset of COVID-19 patients with delayed recovery that continue to show significant ^{18}F -FDG uptake, reminiscent of our findings in ILD (48–50, 256), and raising the possibility that COVID-19 pneumonitis is associated with an activated host immune response rather than direct viral pathology (35, 257, 258). It would be useful to understand the ability of lung avidity to predict clinical course or the likelihood of development of a post-COVID-19 ILD, in this patient-cohort.

The RECOVERY study, which this study pre-dates, demonstrated survival benefit with steroids in hypoxic patients with COVID-19 (257). In our study, several patients went on to develop an inflammatory organising-pneumonia, characterised by persistent and increasing ^{18}F -FDG-uptake. Steroid therapy is a recognised treatment for organizing-pneumonia and other inflammatory ILDs (257), and in those cases treated with post-discharge steroids, ^{18}F -FDG-uptake was consistently lower. Our findings raise the question of whether steroid administration has a role, not just for acute hypoxia but also in the later stages of COVID-19 and for PCLD. This approach has been debated (257) with calls for a randomized-control trial to define the role of steroid therapy more widely. Although imaging may be useful, it is hard to determine from CT whether parenchymal changes indicate reversible inflammation or irreversible fibrosis. It is possible that ^{18}F -FDG-PET/CT may offer a sensitive and specific biomarker to guide and rationalise steroid treatment.

7.5.1 Limitations

Given the challenges of nuclear medicine imaging in the pandemic this study has methodological limitations. They are directly related to the infectious and emergent

epidemic, the workload and severe capacity restraints of PET/CT departments, staff protection and equipment sterilization, and the medical instability of seriously ill COVID-19 patients. This limits patient numbers, preventing the use of a control group and longitudinal ^{18}F -FDG-PET/CT imaging. Diagnostic CT will likely remain the most practical way to investigate acute COVID-19, although PET imaging may give potential mechanistic insights. However, PCLD patients are not currently believed to be an infection risk and thus performing longitudinal ^{18}F -FDG-PET/CT studies in this population may be realistic and feasible. This study was not prospectively designed to study the use of steroid in PCLD; however, statistically-significant lower ^{18}F -FDG uptake in PCLD patients with steroid administration versus those without was observed. Finally, the lack of PCR testing in the first wave, as well as the high incidence of asymptomatic cases throughout the pandemic, creates uncertainties in prevalence and thus retrospective analysis may suffer from selection bias. Despite design limitations, the findings of this study offer some insight into the development of pulmonary disease in COVID-19 and can help provide the evidence to justify performing formal prospective studies on this topic in future.

7.6 Conclusion

In this novel chapter it is shown that ^{18}F -FDG uptake in COVID-19 increases with time after infection and correlates with severity. Persistent ^{18}F -FDG uptake is seen in patients with PCLD disease. These findings suggest that future studies may be directed at the use of ^{18}F -FDG-PET/CT to understand disease trajectory and may aid management of those patients with persistent respiratory symptoms.

7.7 Figures

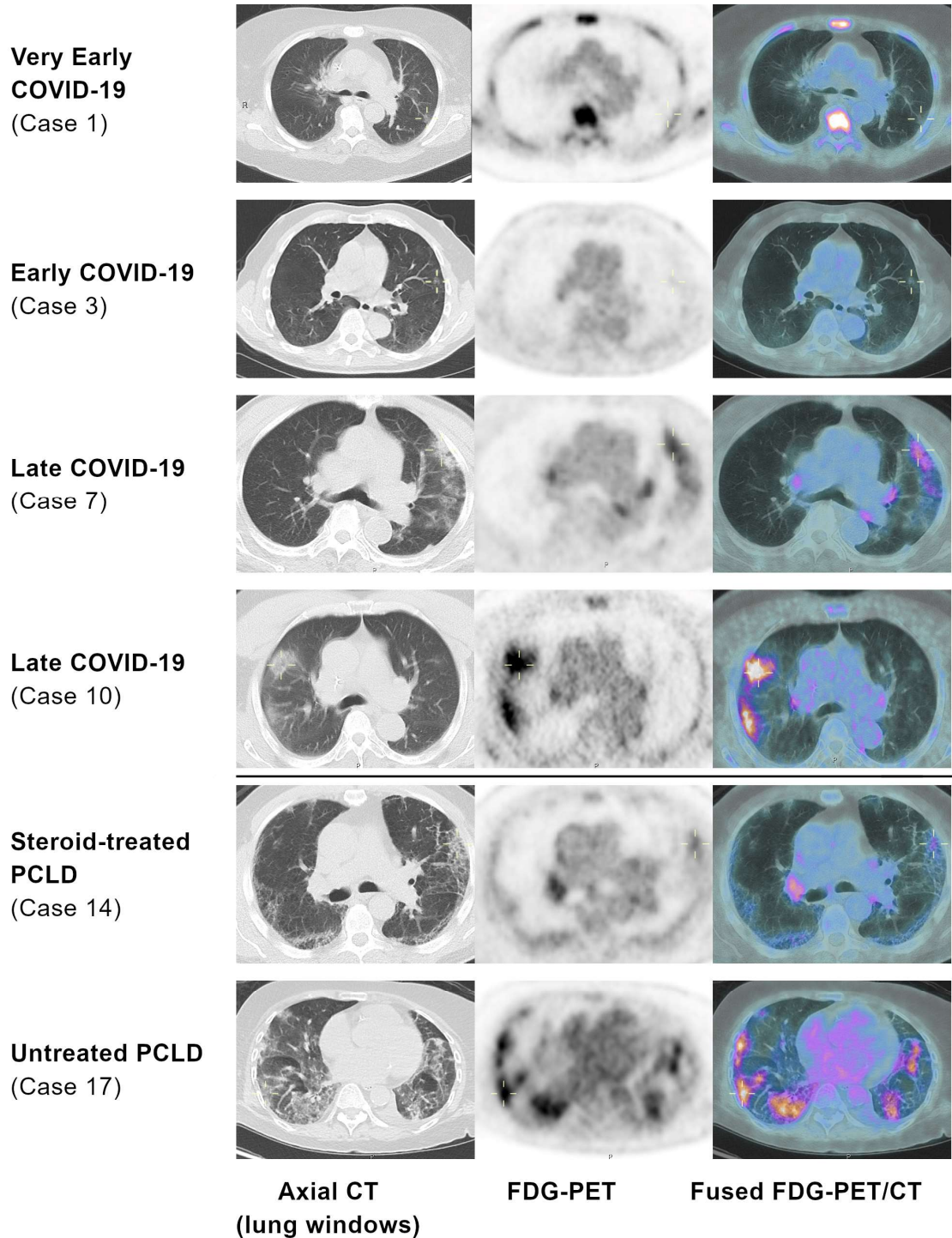


Figure 14: Exemplar images demonstrating increasing ^{18}F -FDG-uptake with temporal stage and lower ^{18}F -FDG-uptake in steroid-treated PCLD.

(Lung-windowed Axial-CT, ^{18}F -FDG-PET windowed SUV 0–5 and fused ^{18}F -FDG-PET/CT images.)

Medullary uptake in case 1 was due to leukaemia and not COVID-19.

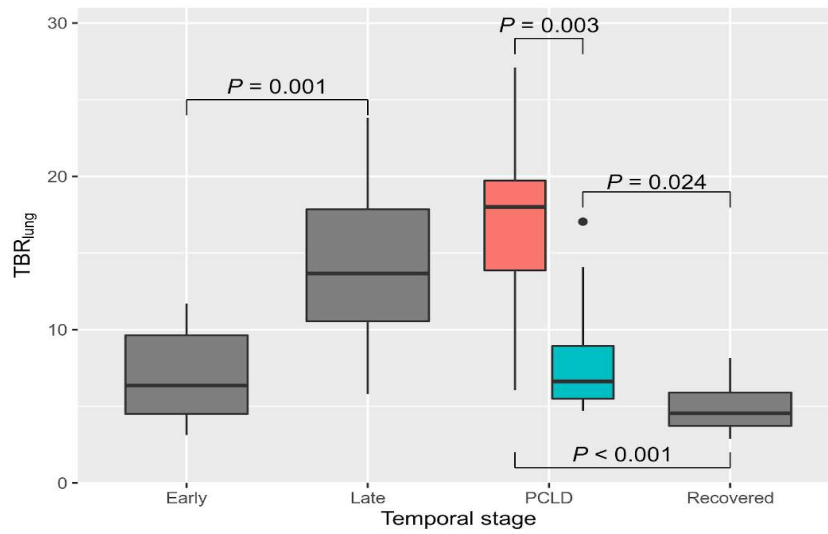


Figure 15: ^{18}F -FDG-uptake (TBR_{lung}) by temporal stage

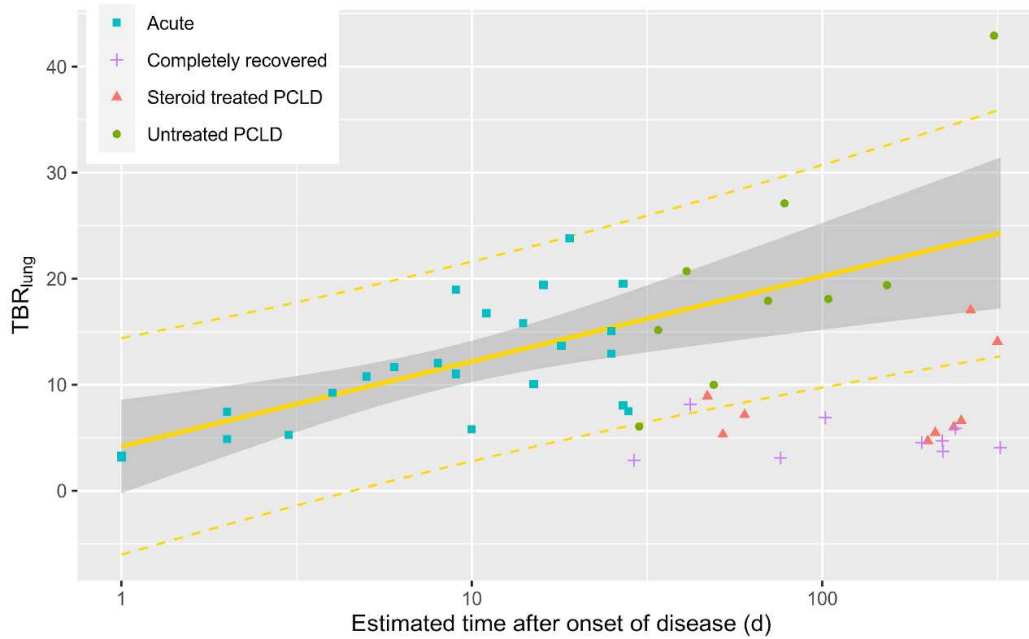


Figure 16: ^{18}F -FDG-uptake (TBR_{lung}) against the estimated time after onset of disease (on a logarithmic scale) with superimposed regression using the 23 acute (early & late) patients. (F -statistic=14.94, $p < 0.001$. Spearman's $r_s = 0.595$, $p = 0.003$.) Steroid treatment means ≥ 10 days high-dose steroid treatment.

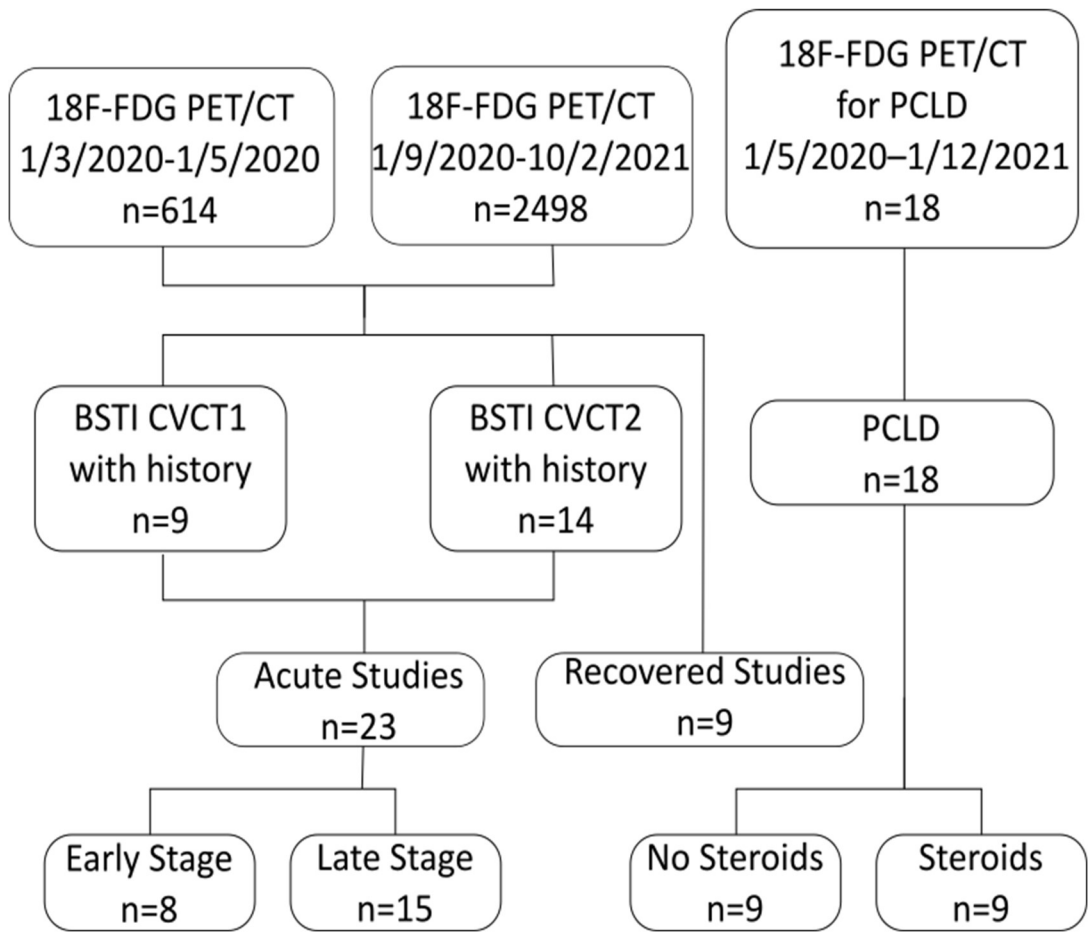


Figure 17: STARD flow chart of study selection.

7.8 Tables

Previous Study Type	Number of papers
Individual case reports demonstrating ¹⁸ F-FDG avidity	23
Case series:	6
<ul style="list-style-type: none"> • 1 paper with 5 patients • 1 paper with 5 patients • 1 paper with 4 patients • 1 paper with 5 patients • 1 paper with 6 patients • 1 paper with 4 patients 	
Incidence & Prevalence of COVID-19 in PET/CT	3
Discussion of the potential future role of PET/CT	3

Table 37: Results of literature review of published papers on COVID-19 and ¹⁸F-FDG PET/CT

Inclusion Criteria

18F-FDG-PET/CT performed within period of acute study collection or referred for PCLD study
 BSTI CVCT1 or CVCT2 changes on CT component of scan or CVCT0 and previous confirmed history of COVID-19 compatible with asymptomatic recovery.
 Clinical history compatible with COVID-19 available on electronic health records

Exclusion Criteria

BSTI CVCT0, CVCT3 changes on CT component except when previously confirmed COVID-19 disease and considered recovered
 No clinical history available or CVCT2 changes explained by other pathology

Table 38: Inclusion and exclusion criteria

Indications	Number of patients
Non-thoracic Cancer	19
Pyrexia of Unknown Origin	2
Paraneoplastic Syndrome	1
Vasculitis	1

Table 39: Indications of the acute cases

Indications	Number of patients
Non-thoracic Cancer	6
Musculoskeletal Inflammation	1
Paraneoplastic Syndrome	1
Cardiac Sarcoid	1

Table 40: Indications of the asymptomatic recovered cases

Case Number	Age at scan (years) & Sex	Temporal Stage	Estimated Time since onset of disease (days)	Admitted to Hospital	PCR Proven	CRP (mg/L)	ESR (mm/hr)	D-Dimer (µg/L FEU)	SpO ₂ during scan	Oxygen during scan	Inpatient at time of scan	Steroid Therapy
1	61F	Early	Early (1–3)	y	y	9.6	—	810	95%	RA	y	n
2	58F	Early	Early (3–7)	n	— ^a	—	—	—	—	RA	n	n
3	72M	Early	Early (3–7)	n	— ^a	—	—	—	—	RA	n	n
4	43F	Early	Early (3–7)	n	— ^a	—	—	—	—	RA	n	n
5	68F	Early	Borderline Early (4–9)	y	y	—	—	—	95%	2L NC	y	n
6	62M	Late	Borderline Late (7–10)	y	y	37.5	—	—	96%	RA	y	n
7	84M	Late	Late (9–14)	n	— ^a	—	—	—	—	RA	n	n
8	18F	Late	Late (10–14)	y	n	228.7	8	2478	97%	RA	y	n
9	76M	Late	Late (11–14)	y	y	6.8	—	1970	98%	RA	y	n
10	60M	Late	Late (11–14)	n	— ^a	—	—	—	—	RA	n	n
11	64M	Late	Late (11–14)	n	— ^a	—	—	—	97%	RA	n	n
12	60M	PCLD	28–36	y	n	1.0 ^c	—	—	100%	RA	y	n
13	80M	PCLD	30–38	y	y	— ^c	—	—	92%	1L NC	y	n
14	60M	PCLD	42–52	y	n	8.4 ^c	—	—	97%	RA	y	y
15	71M	PCLD	48–56	y	y	— ^c	—	—	94% ^b	RA	n	y
16	68F	PCLD	54–64	y	n	14.7 ^c	—	—	95%	1L NC	y	y
17	72F	PCLD	64–74	y	y	121.6 ^c	—	—	91%	RA	y	n
18	60F	PCLD	70–85	y	y	— ^c	—	—	96% ^b	RA	n	n
19	60M	PCLD	150–160	y	y	121.2 ^c	70	300	96%	RA	n	n
20	56M	PCLD	210–215	y	y	1.2 ^c	—	—	95%	RA	n	y
21	27F	Recovered	76–80	y	y	—	—	—	100%	RA	n	n
22	39M	Recovered	26–30	y	y	—	—	—	99%	RA	n	n
23	58M	PCLD	195–205	y	y	63.7 ^c	120	1080	95%	RA	n	y
24	60M	PCLD	260–270	y	y	51.9 ^c	28	190	99%	RA	n	y
25	51M	Recovered	180–200	y	y	—	—	—	95%	RA	n	n
26	45M	PCLD	100–120	n	y	14.5 ^c	—	500	95%	RA	n	n
27	61M	PCLD	240–250	y	y	0 ^c	—	1280	95%	RA	n	y
28	72M	PCLD	45–52	y	y	122.8 ^c	111	1570	99%	RA	y	n
29	47F	Late	Borderline Late (9–12)	y	y	43.4	—	390	99%	RA	y	n
30	61M	PCLD	232–242	y	n	11.9 ^c	—	—	100%	RA	n	y
31	48M	Late	Late (20–30)	y	y	5.7	5	1690	99%	RA	y	n
32	70M	PCLD	39–43	y	y	—	—	—	95%	RA	y	n
33	87F	Late	Late (22–28)	y	y	38.7	—	1290	92%	1L NC	y	n
34	66M	PCLD	309–320	y	y	—	—	—	95%	2L NC	n	y
35	59F	Late	Late (13–18)	n	y	—	—	—	97%	RA	n	n
36	51F	Late	Late (15–25)	n	y	—	—	—	95%	RA	n	n
37	87F	Early	Early (5–7)	y	y	10.4	27	—	96%	RA	y	n
38	61M	Recovered	215–225	n	y	—	—	—	97%	RA	n	n
39	79M	Recovered	200–240	n	y	—	—	—	95%	RA	n	n
40	60F	Early	Early (1–3)	n	y	—	—	—	95%	RA	n	n
41	51M	Late	Late (26–28)	y	y	—	—	1380	95%	RA	n	n
42	60M	Recovered	200–220	n	— ^a	—	—	—	96%	RA	n	n
43	61M	Late	Late (20–28)	y	n	—	—	—	95%	RA	n	n
44	61F	PCLD	300–315	y	y	—	—	—	96%	RA	n	n
45	79M	Late	Late (19–23)	y	y	—	—	—	98%	RA	y	n
46	61M	Recovered	317–330	y	y	—	—	—	95%	RA	n	n
47	61M	Recovered	38–44	y	y	—	—	—	97%	RA	n	n

48	75F	Late	Late (25–28)	y	y	—	—	—	94%	2L NC	y	n
49	74F	Recovered	90–120	n	y	—	—	—	95%	RA	n	n
50	80M	Early	Early (1–3)	y	y	—	—	—	96%	RA	y	n

Table 41: Distribution and Clinical Parameters

^a At the time of infection availability of PCR testing was limited to only patients admitted to hospital

^b Saturations measured on different day to imaging. RA: Room Air; NC: nasal cannulae

^c CRP was noted to be falling from peak for all Delayed Recovery patients

—: Test not performed

Steroid therapy was defined as high dose steroids for 10 days or more

Please note: formal lung function tests were not performed on these patients due to the pandemic.

8 Limitations

8.1 Lung Cancer Dataset

As discussed in Chapters 3-6 there are a number of limitations with the lung cancer dataset. Due to the importance of ^{18}F -FDG PET/CT in the diagnosis of lung cancer many patients who undergo imaging with ^{18}F -FDG PET/CT will not have lung cancer.

Recruitment was therefore focused on patients whom it was felt had a high pre-test probability of having lung cancer. This severely biases our population of patients who were eventually not diagnosed with lung cancer meaning these patients do not represent a fair sample and thus these patients were excluded from analysis.

Similarly, due to the desire for surgical histology, patient recruitment was focused on patients who were expected to be fit for surgery and to have operable disease. This results in a patient population heavily weighted towards lower stage disease, and biases the population toward surgically fit patients as compared to the normal population of the lung cancers. These biases mean that the survival of our population of Stage II–IV patients is likely to be artificially large — especially for the larger tumours. (For example, our one-year survival for all our patients and all Stage III patients was 74.9% and 63.4% respectively whereas the 2013–2017 age standardised one-year survival in the UK is only 40.6% and 48.1% respectively (3)). It may also artificially increase the difference in survival between those treated with Surgery versus those not, as non-surgical treatment may reflect worse non-tumoural prognostic factors, e.g. heart disease, fibrosis, and emphysema. It should be noted that these biases which improve survival make finding significant correlations with survival more difficult rather than easier, and thus should strengthen positive results.

The requirement for CT perfusion and desire for surgical histology also excludes very small tumours because the results of CT perfusion imaging of tumours smaller than 1cm can be rather inaccurate and very small tumours may be treated non-surgically. The overall smaller stage however, still means that the imaging biomarkers may be negatively affected by partial volume effects, breath motion and other motion artefacts.

The overall population size is still relatively small, and somewhat heterogeneous in stage of disease meaning that we could not check if there were statistically significant correlations between biomarkers and substages nor correlate against full-staging (i.e. Stage Ia, Ib, Ic, IIa etc. vs Stage I, II, III and IV).

8.2 COVID-19 Dataset

The limitations of the COVID-19 dataset are discussed in detail in Section 7.5.1.

9 Conclusion

The The main findings of this study and possible clinical relevance are summarized here.

9.1 ^{18}F -FDG PET/CT Biomarkers

Both lower SUV_{max} and TBR_{lung} are statistically associated with survival but neither are independent of Stage. Lower TBR_{lung} is more strongly associated with survival than SUV_{max} .

The finding that these prognostic factors are not independent of stage are in some ways unsurprising given the role of SUV_{max} (and other uptake measures) in diagnosis and the part they play in staging. The discovery that a cut-off for TBR_{lung} acts as a strong predictor especially in Stage I disease is a novel and interesting finding and suggests further investigation with a larger cohort may prove a direct role for TBR_{lung} (or even SUV_{max}) in sub-staging Stage I disease in addition to lesion size.

9.2 CT Perfusion in Lung Cancer

There is no definite clear correlation with CT perfusion biomarkers and survival within our study population, and there is no clear added benefit to CT perfusion over that of ^{18}F -FDG based staging and surgery. Subgroup analysis restricting to the higher stage patients treated with chemotherapy shows statistically significant correlations between survival and the CT perfusion biomarkers which does replicate the findings of other studies and, whilst caution should be taken when interpreting these as the numbers of patients in this group are small, they highlight the potential utility of CT Perfusion imaging in these cases.

9.3 Texture Analysis with TexRAD in Lung Cancer

Multiple CT and PET textural features are statistically significantly related to survival and in particular CT entropy at fine texture ($\text{SSF}=2\text{mm}$) is statistically significantly related to survival when combined with Surgery and Staging and remains statistically significant when the whole treatment group is split into training and validation sets.

The finding that $\text{entropy_ct_ssf_2} > 4.81$ remains statistically significant in a combined model with staging and surgical status across the whole dataset suggests that textural analysis can be used to provide additional stratification over that of staging and surgical status alone. The technique for ROI selection used in the study is quick and simple, many other studies have relied on segmenting the whole tumour often using a separate diagnostic CT, and was further coupled with CT thresholding, allowing one to draw more generous borders around tumours centred within the lung but still result with the same ROI. Prospective analysis on a future cohort using this cut-off would help further prove the utility of this measure; it may also be helpful to review the effect of radiotherapy and chemotherapy on entropy_ct_ssf_2 and whether it could provide an earlier marker of recurrence or response.

9.4 Correlation Between Immunohistochemistry and Mutation and Imaging Biomarkers

There were several interesting correlations between imaging biomarkers and the immunohistochemical and mutation biomarkers, some of which were highly significant. In particular the correlations found between imaging biomarkers and GLUT1 and CD105 give potentially tantalising *in vivo* insights into tumour metabolism, hypoxia and vascularity. These techniques have significant prognostic and predictive potential and further large studies applied to lung-cancer treatment studies may prove this. The initial results could be further investigated to suggest multivariate predictors for mutation status or immunohistochemical markers.

9.5 Evolution of ^{18}F -FDG-PET/CT Findings in Patients Following COVID-19

This study opportunistically analysed incidental findings of COVID-19 disease and post-COVID-19 lung disease in a novel manner: correlating CT findings and clinical details to estimate disease time course and then using this information to further study ^{18}F -FDG uptake. The study demonstrated ^{18}F -FDG uptake in COVID-19 increases with time after infection and correlates with severity in contrast to the usual appearances of viral or infectious diseases, thus suggesting an inflammatory component to disease symptoms.

The persistent ^{18}F -FDG uptake seen in patients with PCLD disease suggests that this may be due to abnormally long-lasting inflammation. These findings suggest that future studies may be directed at the use of ^{18}F -FDG-PET/CT to understand disease trajectory and may aid management of those patients with persistent respiratory symptoms.

This study further demonstrates the value of TBR_{lung} in ILD and suggests it has a role across the spectrum of ILD not just in IPF.

9.6 Further Work

The findings in this thesis suggest further investigation of the ^{18}F -FDG-PET biomarkers and ^{18}F -FDG-PET/CT TexRAD biomarkers would be of value. In particular it would be helpful to more closely study $\text{SUV}_{\text{max}} > 7.6$ and $\text{entropy}_{\text{ct_ssf_2}} > 4.81$ across both more focused multicentre datasets and more general multicentre lung cancer datasets. It would similarly be of interest to evaluate if $\text{TBR}_{\text{lung}} \leq 26.2$ remains prognostic in a Stage I disease. Further multivariate analysis of the histological dataset should also be performed with the histological dataset expanded with further recruitment. The correlations found between imaging biomarkers and GLUT1 and CD105 give potentially tantalising *in vivo* insights into tumour metabolism, hypoxia and vascularity. These techniques have significant prognostic and predictive potential and further large studies applied to lung-cancer treatment studies may prove this.

The findings in Chapter 7 suggest that future studies directed at the use of ^{18}F -FDG-PET/CT to understand disease trajectory of COVID-19 and PCLD should be considered and that ^{18}F -FDG-PET/CT should be considered when managing patients with persistent respiratory symptoms following infection. Of course, the emergency phase of the SARS-CoV-2 pandemic is now over which makes further work here difficult, but should another variant of concern arise or another novel coronavirus epidemic/pandemic these results should be used to guide further work.

9.7 Summary

The most important results of this thesis are:

- The findings that cut-offs of $SUV_{max} > 7.6$ & $TBR_{lung} > 26.2$ are statistically significantly associated with worse prognosis.
- The finding that $entropy_ct_ssf_2 > 4.81$ is an independent predictor of survival across the whole TexRAD cohort in a combined model with staging and survival, and also stratifies survival when there mutations present in the histological subset.
- PCLD is associated with avidity which is reduced by steroids

Bibliography

1. Cancer survival statistics for all cancers combined. Cancer Research UK [Internet]. 2015 [cited 2021 Dec 13]. Available from: <https://www.cancerresearchuk.org/health-professional/cancer-statistics/survival/all-cancers-combined>.
2. Quaresma M, Coleman MP, Rachet B. 40-year trends in an index of survival for all cancers combined and survival adjusted for age and sex for each cancer in England and Wales, 1971–2011: a population-based study. *The Lancet* [Internet]. Elsevier; 2015 [cited 2021 Dec 16]; 385(9974):1206–18. Available from: [https://www.thelancet.com/journals/lancet/article/PIIS0140-6736\(14\)61396-9/fulltext](https://www.thelancet.com/journals/lancet/article/PIIS0140-6736(14)61396-9/fulltext).
3. Cancer survival in England - adults diagnosed - Office for National Statistics [Internet]. [cited 2021 Dec 13]. Available from: <https://www.ons.gov.uk/peoplepopulationandcommunity/healthandsocialcare/conditionsanddiseases/datasets/cancersurvivalratescancersurvivalinenglandadultsdiagnosed>.
4. Goldstraw P, Chansky K, Crowley J, Rami-Porta R, Asamura H, Eberhardt WEE, et al. The IASLC Lung Cancer Staging Project: Proposals for Revision of the TNM Stage Groupings in the Forthcoming (Eighth) Edition of the TNM Classification for Lung Cancer. *Journal of Thoracic Oncology* [Internet]. Elsevier; 2016 [cited 2021 Dec 16]; 11(1):39–51. Available from: [https://www.jto.org/article/S1556-0864\(15\)00017-9/fulltext](https://www.jto.org/article/S1556-0864(15)00017-9/fulltext).
5. Lung cancer statistics. Cancer Research UK [Internet]. 2015 [cited 2022 Feb 7]. Available from: <https://www.cancerresearchuk.org/health-professional/cancer-statistics/statistics-by-cancer-type/lung-cancer>.
6. Ferlay J, Colombet M, Soerjomataram I, Dyba T, Randi G, Bettio M, et al. Cancer incidence and mortality patterns in Europe: Estimates for 40 countries and 25 major cancers in 2018. *European Journal of Cancer* [Internet]. Elsevier; 2018 [cited 2021 Dec 16]; 103:356–87. Available from: [https://www.ejca.com/article/S0959-8049\(18\)30955-9/fulltext](https://www.ejca.com/article/S0959-8049(18)30955-9/fulltext).
7. Groot PM de, Wu CC, Carter BW, Munden RF. The epidemiology of lung cancer. *Transl Lung Cancer Res* [Internet]. 2018 [cited 2022 Feb 7]; 7(3):220–33. Available from: <https://www.ncbi.nlm.nih.gov/pmc/articles/PMC6037963/>.
8. Alberg AJ, Samet JM. Epidemiology of Lung Cancer*. *CHEST* [Internet]. Elsevier; 2003 [cited 2022 Jul 18]; 123(1):21S–49S. Available from: [https://journal.chestnet.org/article/S0012-3692\(15\)32981-0/abstract](https://journal.chestnet.org/article/S0012-3692(15)32981-0/abstract).
9. Siddiqui F, Vaqar S, Siddiqui AH. Lung Cancer. In: *StatPearls* [Internet]. Treasure Island (FL): StatPearls Publishing; 2022 [cited 2022 Jul 15]. Available from: <http://www.ncbi.nlm.nih.gov/books/NBK482357/>.
10. Miller YE. Pathogenesis of Lung Cancer. *Am J Respir Cell Mol Biol* [Internet]. 2005 [cited 2022 Jul 15]; 33(3):216–23. Available from: <https://www.ncbi.nlm.nih.gov/pmc/articles/PMC2715312/>.
11. Agents Classified by the IARC Monographs, Volumes 1–130 – IARC Monographs on the Identification of Carcinogenic Hazards to Humans [Internet]. [cited 2022 Feb 7]. Available from: <https://monographs.iarc.who.int/agents-classified-by-the-iarc/>.
12. Brown KF, Rungay H, Dunlop C, Ryan M, Quartly F, Cox A, et al. The fraction of cancer attributable to modifiable risk factors in England, Wales, Scotland, Northern Ireland, and the United Kingdom in 2015. *Br J Cancer*. 2018; 118(8):1130–41.

13. Peto R, Boreham J, Lopez AD, Thun M, Heath C. Mortality from tobacco in developed countries: indirect estimation from national vital statistics. *The Lancet* [Internet]. Elsevier; 1992 [cited 2022 Feb 7]; 339(8804):1268–78. Available from: [https://www.thelancet.com/journals/lancet/article/PII0140-6736\(92\)91600-D/fulltext](https://www.thelancet.com/journals/lancet/article/PII0140-6736(92)91600-D/fulltext).
14. Cagle PT, Allen TC, Olsen RJ. Lung cancer biomarkers: present status and future developments. *Arch Pathol Lab Med*. 2013; 137(9):1191–8.
15. Nicholson AG, Tsao MS, Beasley MB, Borczuk AC, Brambilla E, Cooper WA, et al. The 2021 WHO Classification of Lung Tumors: Impact of Advances Since 2015. *Journal of Thoracic Oncology* [Internet]. Elsevier; 2022 [cited 2022 Jul 21]; 17(3):362–87. Available from: [https://www.jto.org/article/S1556-0864\(21\)03316-5/fulltext](https://www.jto.org/article/S1556-0864(21)03316-5/fulltext).
16. National Institute for Health and Care Excellence. Lung cancer: diagnosis and management [Internet]. NICE; 2019 [cited 2022 Feb 9]. Available from: <https://www.nice.org.uk/guidance/ng122>.
17. Postdiagnosis Smoking Cessation and Reduced Risk for Lung Cancer Progression and Mortality: A Prospective Cohort Study: *Annals of Internal Medicine*: Vol 174, No 9 [Internet]. [cited 2022 Feb 9]. Available from: https://www.acpjournals.org/doi/full/10.7326/M21-0252?rfr_dat=cr_pub++0pubmed&url_ver=Z39.88-2003&rfr_id=ori%3Arid%3Acrossref.org.
18. Wells AU, Hirani N, on behalf of the BTS Interstitial Lung Disease Guideline Group, a subgroup of the British Thoracic Society Standards of Care Committee, in collaboration with the Thoracic Society of Australia and New Zealand and the Irish Thoracic Society. Interstitial lung disease guideline. *Thorax* [Internet]. 2008 [cited 2022 Jun 10]; 63(Supplement 5):v1–58. Available from: <https://thorax.bmj.com/lookup/doi/10.1136/thx.2008.101691>.
19. Chapman S, Robinson G, Stradling J, West S, Wrightson J. Diffuse lung disease. *Oxford Handbook of Respiratory Medicine* [Internet]. Oxford University Press; [cited 2022 Jun 10]. Available from: <https://oxfordmedicine.com/view/10.1093/med/9780198703860.001.0001/med-9780198703860-chapter-6>.
20. Ryu JH, Olson EJ, Midthun DE, Swensen SJ. Diagnostic Approach to the Patient With Diffuse Lung Disease. *Mayo Clinic Proceedings* [Internet]. Elsevier; 2002 [cited 2022 Jun 10]; 77(11):1221–7. Available from: [https://www.mayoclinicproceedings.org/article/S0025-6196\(11\)61812-0/fulltext](https://www.mayoclinicproceedings.org/article/S0025-6196(11)61812-0/fulltext).
21. Gruden JF, Naidich DP, Machnicki SC, Cohen SL, Girvin F, Raouf S. An Algorithmic Approach to the Interpretation of Diffuse Lung Disease on Chest CT Imaging: A Theory of Almost Everything. *CHEST* [Internet]. Elsevier; 2020 [cited 2022 Jun 10]; 157(3):612–35. Available from: [https://journal.chestnet.org/article/S0012-3692\(19\)34121-2/abstract](https://journal.chestnet.org/article/S0012-3692(19)34121-2/abstract).
22. Radiology (ACR) RS of NA (RSNA) and AC of. Diffuse Interstitial Lung Disease. *Radiologyinfo.org* [Internet]. [cited 2022 Jun 10]. Available from: <https://www.radiologyinfo.org/en/info/diffuselung>.
23. Huang C, Wang Y, Li X, Ren L, Zhao J, Hu Y, et al. Clinical features of patients infected with 2019 novel coronavirus in Wuhan, China. *Lancet* [Internet]. Elsevier; 2020 [cited 2020 May 21]; 395(10223):497–506. Available from: [https://www.thelancet.com/journals/lancet/article/PIIS0140-6736\(20\)30183-5/abstract](https://www.thelancet.com/journals/lancet/article/PIIS0140-6736(20)30183-5/abstract).
24. Cucinotta D, Vanelli M. WHO Declares COVID-19 a Pandemic. *Acta Biomed*. 2020; 91(1):157–60.
25. Perez Guzman P, Daunt A, Mukherjee S, Crook P, Forlano R, Kont M, et al. Report 17: Clinical characteristics and predictors of outcomes of hospitalised patients with COVID-19 in a London NHS

Trust: a retrospective cohort study [Internet]. Imperial College London; 2020 [cited 2020 May 21]. Available from: <http://spiral.imperial.ac.uk/handle/10044/1/78613>.

26. Bernheim A, Mei X, Huang M, Yang Y, Fayad ZA, Zhang N, et al. Chest CT Findings in Coronavirus Disease-19 (COVID-19): Relationship to Duration of Infection. *Radiology* [Internet]. Radiological Society of North America; 2020 [cited 2020 Apr 29]; 200463. Available from: <https://pubs.rsna.org/doi/10.1148/radiol.2020200463>.
27. Wang Y, Dong C, Hu Y, Li C, Ren Q, Zhang X, et al. Temporal Changes of CT Findings in 90 Patients with COVID-19 Pneumonia: A Longitudinal Study. *Radiology* [Internet]. Radiological Society of North America; 2020 [cited 2020 Apr 29]; 200843. Available from: <https://pubs.rsna.org/doi/full/10.1148/radiol.2020200843>.
28. Pan Y, Guan H, Zhou S, Wang Y, Li Q, Zhu T, et al. Initial CT findings and temporal changes in patients with the novel coronavirus pneumonia (2019-nCoV): a study of 63 patients in Wuhan, China. *Eur Radiol* [Internet]. 2020 [cited 2020 May 20]. Available from: <https://doi.org/10.1007/s00330-020-06731-x>.
29. UPDATED BSTI COVID-19 Guidance for the Reporting Radiologist. The British Society of Thoracic Imaging website [Internet]. [cited 2020 May 18]. Available from: <https://www.bsti.org.uk/standards-clinical-guidelines/clinical-guidelines/bsti-covid-19-guidance-for-the-reporting-radiologist/>.
30. Shi H, Han X, Jiang N, Cao Y, Alwalid O, Gu J, et al. Radiological findings from 81 patients with COVID-19 pneumonia in Wuhan, China: a descriptive study. *Lancet Infect Dis* [Internet]. Elsevier; 2020 [cited 2020 May 18]; 20(4):425–34. Available from: [https://www.thelancet.com/journals/laninf/article/PIIS1473-3099\(20\)30086-4/abstract](https://www.thelancet.com/journals/laninf/article/PIIS1473-3099(20)30086-4/abstract).
31. Kanne JP. Chest CT Findings in 2019 Novel Coronavirus (2019-nCoV) Infections from Wuhan, China: Key Points for the Radiologist. *Radiology* [Internet]. Radiological Society of North America; 2020 [cited 2020 May 18]; 295(1):16–7. Available from: <https://pubs.rsna.org/doi/10.1148/radiol.2020200241>.
32. Pan F, Ye T, Sun P, Gui S, Liang B, Li L, et al. Time Course of Lung Changes at Chest CT during Recovery from Coronavirus Disease 2019 (COVID-19). *Radiology* [Internet]. Radiological Society of North America; 2020 [cited 2020 May 20]; 295(3):715–21. Available from: <https://pubs.rsna.org/doi/10.1148/radiol.2020200370>.
33. Chung M, Bernheim A, Mei X, Zhang N, Huang M, Zeng X, et al. CT Imaging Features of 2019 Novel Coronavirus (2019-nCoV). *Radiology* [Internet]. Radiological Society of North America; 2020 [cited 2020 Apr 29]; 295(1):202–7. Available from: <https://pubs.rsna.org/doi/full/10.1148/radiol.2020200230>.
34. Phua J, Weng L, Ling L, Egi M, Lim C-M, Divatia JV, et al. Intensive care management of coronavirus disease 2019 (COVID-19): challenges and recommendations. *The Lancet Respiratory Medicine* [Internet]. 2020 [cited 2020 May 21]; 8(5):506–17. Available from: <https://linkinghub.elsevier.com/retrieve/pii/S2213260020301612>.
35. Bouadma L, Lescure F-X, Lucet J-C, Yazdanpanah Y, Timsit J-F. Severe SARS-CoV-2 infections: practical considerations and management strategy for intensivists. *Intensive Care Med* [Internet]. 2020 [cited 2020 May 21]; 46(4):579–82. Available from: <https://doi.org/10.1007/s00134-020-05967-x>.
36. Wang D, Hu B, Hu C, Zhu F, Liu X, Zhang J, et al. Clinical Characteristics of 138 Hospitalized Patients With 2019 Novel Coronavirus–Infected Pneumonia in Wuhan, China. *JAMA* [Internet]. American

Medical Association; 2020 [cited 2020 May 21]; 323(11):1061–9. Available from: <https://jamanetwork.com/journals/jama/fullarticle/2761044>.

37. Czernin J, Fanti S, Meyer PT, Allen-Auerbach M, Hacker M, Sathekge M, et al. Nuclear Medicine Operations in the Times of COVID-19: Strategies, Precautions, and Experiences. *J Nucl Med* [Internet]. Society of Nuclear Medicine; 2020 [cited 2020 May 18]; 61(5):626–9. Available from: <http://jnm.snmjournals.org/content/61/5/626>.
38. Young BE, Ong SWX, Kalimuddin S, Low JG, Tan SY, Loh J, et al. Epidemiologic Features and Clinical Course of Patients Infected With SARS-CoV-2 in Singapore. *JAMA* [Internet]. American Medical Association; 2020 [cited 2020 May 21]; 323(15):1488–94. Available from: <https://jamanetwork.com/journals/jama/fullarticle/2762688>.
39. Salehi S, Abedi A, Balakrishnan S, Gholamrezaezhad A. Coronavirus Disease 2019 (COVID-19): A Systematic Review of Imaging Findings in 919 Patients. *American Journal of Roentgenology* [Internet]. American Roentgen Ray Society; 2020 [cited 2020 May 21]; 1–7. Available from: <https://www.ajronline.org/doi/full/10.2214/AJR.20.23034>.
40. Sardanelli F, Cozzi A, Monfardini L, Bnà C, Foà RA, Spinazzola A, et al. Association of mediastinal lymphadenopathy with COVID-19 prognosis. *Lancet Infect Dis* [Internet]. 2020 [cited 2020 Jul 4]. Available from: <https://www.ncbi.nlm.nih.gov/pmc/articles/PMC7304961/>.
41. Mo X, Jian W, Su Z, Chen M, Peng H, Peng P, et al. Abnormal pulmonary function in COVID-19 patients at time of hospital discharge. *European Respiratory Journal* [Internet]. European Respiratory Society; 2020 [cited 2020 Jul 20]. Available from: <https://erj.ersjournals.com/content/early/2020/05/07/13993003.01217-2020>.
42. Carfi A, Bernabei R, Landi F, Group for the GAC-19 P-ACS. Persistent Symptoms in Patients After Acute COVID-19. *JAMA* [Internet]. American Medical Association; 2020 [cited 2020 Sep 9]; 324(6):603–5. Available from: <https://jamanetwork.com/journals/jama/fullarticle/2768351>.
43. Stavem K, Ghanima W, Olsen MK, Gilboe HM, Einvik G. Persistent symptoms 1.5–6 months after COVID-19 in non-hospitalised subjects: a population-based cohort study. *Thorax* [Internet]. BMJ Publishing Group Ltd; 2021 [cited 2021 Apr 26]; 76(4):405–7. Available from: <https://thorax.bmj.com/content/76/4/405>.
44. Sahanic S, Thomas S, Alex P, Gerlig W, Anna L, Magdalena A, et al. Abstract no: OA4143: Persisting pulmonary impairment following severe SARS-CoV-2 infection, preliminary results from the CovILD study. *European Respiratory Society International Congress*. European Respiratory Society; 2020.
45. Arnold DT, Hamilton FW, Milne A, Morley A, Viner J, Attwood M, et al. Patient outcomes after hospitalisation with COVID-19 and implications for follow-up; results from a prospective UK cohort. *medRxiv* [Internet]. Cold Spring Harbor Laboratory Press; 2020 [cited 2020 Sep 8]; 2020.08.12.20173526. Available from: <https://www.medrxiv.org/content/10.1101/2020.08.12.20173526v1>.
46. Hosseiny M, Kooraki S, Gholamrezaezhad A, Reddy S, Myers L. Radiology Perspective of Coronavirus Disease 2019 (COVID-19): Lessons From Severe Acute Respiratory Syndrome and Middle East Respiratory Syndrome. *American Journal of Roentgenology* [Internet]. American Roentgen Ray Society; 2020 [cited 2020 May 21]; 214(5):1078–82. Available from: <https://www.ajronline.org/doi/full/10.2214/AJR.20.22969>.
47. Assiri A, Al-Tawfiq JA, Al-Rabeeh AA, Al-Rabiah FA, Al-Hajjar S, Al-Barrak A, et al. Epidemiological, demographic, and clinical characteristics of 47 cases of Middle East respiratory syndrome coronavirus disease from Saudi Arabia: a descriptive study. *The Lancet Infectious Diseases*

[Internet]. 2013 [cited 2020 May 21]; 13(9):752–61. Available from: <http://www.sciencedirect.com/science/article/pii/S1473309913702044>.

48. Groves AM, Win T, Screatton NJ, Berovic M, Endozo R, Booth H, et al. Idiopathic pulmonary fibrosis and diffuse parenchymal lung disease: implications from initial experience with 18F-FDG PET/CT. *J Nucl Med*. 2009; 50(4):538–45.
49. Win T, Screatton NJ, Porter JC, Ganeshan B, Maher TM, Fraioli F, et al. Pulmonary 18F-FDG uptake helps refine current risk stratification in idiopathic pulmonary fibrosis (IPF). *Eur J Nucl Med Mol Imaging* [Internet]. 2018 [cited 2020 Apr 27]; 45(5):806–15. Available from: <https://www.ncbi.nlm.nih.gov/pmc/articles/PMC5978900/>.
50. Win T, Screatton NJ, Porter J, Endozo R, Wild D, Kayani I, et al. Novel positron emission tomography/computed tomography of diffuse parenchymal lung disease combining a labeled somatostatin receptor analogue and 2-deoxy-2[18F]fluoro-D-glucose. *Mol Imaging*. 2012; 11(2):91–8.
51. Chen DL, Ballout S, Chen L, Cheriyan J, Choudhury G, Denis-Bacelar AM, et al. Consensus recommendations on the use of 18F-FDG PET/CT in lung disease. *J Nucl Med*. 2020.
52. Rodrigues RS, Miller PR, Bozza FA, Marchiori E, Zimmerman GA, Hoffman JM, et al. FDG-PET in patients at risk for acute respiratory distress syndrome: a preliminary report. *Intensive Care Med* [Internet]. 2008 [cited 2020 May 18]; 34(12):2273. Available from: <https://doi.org/10.1007/s00134-008-1220-7>.
53. Jacene HA, Cohade C, Wahl RL. F-18 FDG PET/CT in Acute Respiratory Distress Syndrome: A Case Report: *Clinical Nuclear Medicine* [Internet]. 2004 [cited 2020 May 18]; 29(12):786–8. Available from: <http://content.wkhealth.com/linkback/openurl?sid=WKPTLP:landingpage&an=00003072-200412000-00002>.
54. Biomarkers and surrogate endpoints: Preferred definitions and conceptual framework. *Clinical Pharmacology & Therapeutics* [Internet]. 2001 [cited 2022 Feb 10]; 69(3):89–95. Available from: <https://onlinelibrary.wiley.com/doi/abs/10.1067/mcp.2001.113989>.
55. FDA-NIH Biomarker Working Group. BEST (Biomarkers, EndpointS, and other Tools) Resource [Internet]. Silver Spring (MD): Food and Drug Administration (US); 2016 [cited 2022 Feb 10]. Available from: <http://www.ncbi.nlm.nih.gov/books/NBK326791/>.
56. Croteau E, Renaud JM, Richard MA, Ruddy TD, Bénard F, deKemp RA. PET Metabolic Biomarkers for Cancer. *Biomark Cancer* [Internet]. 2016 [cited 2019 Oct 30]; 8(Suppl 2):61–9. Available from: <https://www.ncbi.nlm.nih.gov/pmc/articles/PMC5030827/>.
57. Plana JC, Galderisi M, Barac A, Ewer MS, Ky B, Scherrer-Crosbie M, et al. Expert Consensus for Multimodality Imaging Evaluation of Adult Patients during and after Cancer Therapy: A Report from the American Society of Echocardiography and the European Association of Cardiovascular Imaging. *Journal of the American Society of Echocardiography* [Internet]. Elsevier; 2014 [cited 2022 Feb 25]; 27(9):911–39. Available from: [https://www.onlinejase.com/article/S0894-7317\(14\)00534-3/fulltext](https://www.onlinejase.com/article/S0894-7317(14)00534-3/fulltext).
58. O'Connor JPB, Aboagye EO, Adams JE, Aerts HJWL, Barrington SF, Beer AJ, et al. Imaging biomarker roadmap for cancer studies. *Nat Rev Clin Oncol* [Internet]. Nature Publishing Group; 2017 [cited 2022 Feb 7]; 14(3):169–86. Available from: <https://www.nature.com/articles/nrclinonc.2016.162>.

59. Law WP, Miles KA. Incorporating prognostic imaging biomarkers into clinical practice. *Cancer Imaging* [Internet]. 2013 [cited 2022 Feb 7]; 13(3):332–41. Available from: <https://www.ncbi.nlm.nih.gov/pmc/articles/PMC3781605/>.
60. Kawada K, Iwamoto M, Sakai Y. Mechanisms underlying 18F-fluorodeoxyglucose accumulation in colorectal cancer. *World J Radiol* [Internet]. 2016 [cited 2021 Dec 16]; 8(11):880–6. Available from: <https://www.ncbi.nlm.nih.gov/pmc/articles/PMC5120247/>.
61. Li X-F, Du Y, Ma Y, Postel GC, Civelek AC. 18F-Fluorodeoxyglucose Uptake and Tumor Hypoxia: Revisit 18F-Fluorodeoxyglucose in Oncology Application. *Transl Oncol* [Internet]. 2014 [cited 2021 Dec 16]; 7(2):240–7. Available from: <https://www.ncbi.nlm.nih.gov/pmc/articles/PMC4101348/>.
62. Muz B, Puente P de la, Azab F, Azab AK. The role of hypoxia in cancer progression, angiogenesis, metastasis, and resistance to therapy. *Hypoxia (Auckl)* [Internet]. 2015 [cited 2021 Dec 16]; 3:83–92. Available from: <https://www.ncbi.nlm.nih.gov/pmc/articles/PMC5045092/>.
63. AL-Jahdali H, Khan AN, Loutfi S, Al-Harbi AS. Guidelines for the role of FDG-PET/CT in lung cancer management. *Journal of Infection and Public Health* [Internet]. 2012 [cited 2022 Feb 28]; 5:535–40. Available from: <https://www.sciencedirect.com/science/article/pii/S1876034112000974>.
64. Dwamena BA, Sonnad SS, Angobaldo JO, Wahl RL. Metastases from Non-Small Cell Lung Cancer: Mediastinal Staging in the 1990s—Meta-analytic Comparison Of PET and CT. *Radiology* [Internet]. Radiological Society of North America; 1999 [cited 2022 Feb 28]; 213(2):530–6. Available from: <https://pubs.rsna.org/doi/10.1148/radiology.213.2.r99nv46530>.
65. Gould MK, Kuschner WG, Rydzak CE, Maclean CC, Demas AN, Shigemitsu H, et al. Test performance of positron emission tomography and computed tomography for mediastinal staging in patients with non-small-cell lung cancer: a meta-analysis. *Ann Intern Med*. 2003; 139(11):879–92.
66. Silvestri GA, Gould MK, Margolis ML, Tanoue LT, McCrory D, Toloza E, et al. Noninvasive Staging of Non-small Cell Lung Cancer: ACCP Evidenced-Based Clinical Practice Guidelines (2nd Edition). *Chest* [Internet]. 2007 [cited 2022 Feb 28]; 132(3, Supplement):178S–201S. Available from: <https://www.sciencedirect.com/science/article/pii/S0012369215355197>.
67. Silvestri GA, Gonzalez AV, Jantz MA, Margolis ML, Gould MK, Tanoue LT, et al. Methods for Staging Non-small Cell Lung Cancer: Diagnosis and Management of Lung Cancer, 3rd ed: American College of Chest Physicians Evidence-Based Clinical Practice Guidelines. *CHEST* [Internet]. Elsevier; 2013 [cited 2022 Feb 28]; 143(5):e211S–e250S. Available from: [https://journal.chestnet.org/article/S0012-3692\(13\)60296-2/abstract](https://journal.chestnet.org/article/S0012-3692(13)60296-2/abstract).
68. Huang (Henry) Sung-Cheng. Anatomy of SUV. *Nuclear Medicine and Biology* [Internet]. 2000 [cited 2022 Feb 28]; 27(7):643–6. Available from: <https://www.sciencedirect.com/science/article/pii/S0969805100001554>.
69. Ahuja V, Coleman RE, Herndon J, Patz EF. The prognostic significance of fluorodeoxyglucose positron emission tomography imaging for patients with nonsmall cell lung carcinoma. *Cancer*. 1998; 83(5):918–24.
70. Dhital K, Saunders CAB, Seed PT, O’Doherty MJ, Dussek J. [18F]Fluorodeoxyglucose positron emission tomography and its prognostic value in lung cancer☆. *European Journal of Cardio-Thoracic Surgery* [Internet]. 2000 [cited 2022 Jan 14]; 18(4):425–8. Available from: [https://doi.org/10.1016/S1010-7940\(00\)00535-2](https://doi.org/10.1016/S1010-7940(00)00535-2).

71. Jeong H-J, Min J-J, Park JM, Chung J-K, Kim BT, Jeong JM, et al. Determination of the prognostic value of [(18)F]fluorodeoxyglucose uptake by using positron emission tomography in patients with non-small cell lung cancer. *Nucl Med Commun*. 2002; 23(9):865–70.
72. Downey RJ, Akhurst T, Gonen M, Vincent A, Bains MS, Larson S, et al. Preoperative F-18 fluorodeoxyglucose-positron emission tomography maximal standardized uptake value predicts survival after lung cancer resection. *J Clin Oncol*. 2004; 22(16):3255–60.
73. Borst GR, Belderbos JSA, Boellaard R, Comans EFI, Jaeger KD, Lammertsma AA, et al. Standardised FDG uptake: A prognostic factor for inoperable non-small cell lung cancer. *European Journal of Cancer* [Internet]. Elsevier; 2005 [cited 2022 Jan 10]; 41(11):1533–41. Available from: [https://www.ejancer.com/article/S0959-8049\(05\)00338-2/fulltext](https://www.ejancer.com/article/S0959-8049(05)00338-2/fulltext).
74. Sasaki R, Komaki R, Macapinlac H, Erasmus J, Allen P, Forster K, et al. [18F]Fluorodeoxyglucose Uptake by Positron Emission Tomography Predicts Outcome of Non–Small-Cell Lung Cancer. *JCO* [Internet]. Wolters Kluwer; 2005 [cited 2022 Jan 14]; 23(6):1136–43. Available from: <https://ascopubs.org/doi/10.1200/JCO.2005.06.129>.
75. Davies A, Tan C, Paschalides C, Barrington SF, O’Doherty M, Utley M, et al. FDG-PET maximum standardised uptake value is associated with variation in survival: Analysis of 498 lung cancer patients. *Lung Cancer* [Internet]. Elsevier; 2007 [cited 2022 Jan 14]; 55(1):75–8. Available from: [https://www.lungcancerjournal.info/article/S0169-5002\(06\)00489-2/fulltext](https://www.lungcancerjournal.info/article/S0169-5002(06)00489-2/fulltext).
76. Lee YJ, Cho A, Cho BC, Yun M, Kim SK, Chang J, et al. High Tumor Metabolic Activity as Measured by Fluorodeoxyglucose Positron Emission Tomography Is Associated with Poor Prognosis in Limited and Extensive Stage Small-Cell Lung Cancer. *Clin Cancer Res* [Internet]. American Association for Cancer Research; 2009 [cited 2022 Jan 14]; 15(7):2426–32. Available from: <https://clincancerres.aacrjournals.org/content/15/7/2426>.
77. Uehara H, Tsutani Y, Okumura S, Nakayama H, Adachi S, Yoshimura M, et al. Prognostic Role of Positron Emission Tomography and High-Resolution Computed Tomography in Clinical Stage IA Lung Adenocarcinoma. *The Annals of Thoracic Surgery* [Internet]. Elsevier; 2013 [cited 2022 Jan 14]; 96(6):1958–65. Available from: [https://www.annalsthoracicsurgery.org/article/S0003-4975\(13\)01432-X/fulltext](https://www.annalsthoracicsurgery.org/article/S0003-4975(13)01432-X/fulltext).
78. Khiewvan B, Ziai P, Houshmand S, Salavati A, Ziai P, Alavi A. The role of PET/CT as a prognosticator and outcome predictor in lung cancer. *Expert Review of Respiratory Medicine* [Internet]. Taylor & Francis; 2016 [cited 2022 Jan 10]; 10(3):317–30. Available from: <https://doi.org/10.1586/17476348.2016.1147959>.
79. Geus-Oei L-F de, Heijden HFM van der, Corstens FHM, Oyen WJG. Predictive and prognostic value of FDG-PET in nonsmall-cell lung cancer. *Cancer* [Internet]. 2007 [cited 2022 Mar 31]; 110(8):1654–64. Available from: <https://onlinelibrary.wiley.com/doi/abs/10.1002/cncr.22979>.
80. Cerfolio RJ, Bryant AS, Ohja B, Bartolucci AA. The maximum standardized uptake values on positron emission tomography of a non-small cell lung cancer predict stage, recurrence, and survival. *The Journal of Thoracic and Cardiovascular Surgery* [Internet]. Elsevier; 2005 [cited 2022 Jan 14]; 130(1):151–9. Available from: [https://www.jtcvs.org/article/S0022-5223\(04\)01601-0/fulltext](https://www.jtcvs.org/article/S0022-5223(04)01601-0/fulltext).
81. Eschmann SM, Friedel G, Paulsen F, Reimold M, Hehr T, Budach W, et al. Is standardised 18F-FDG uptake value an outcome predictor in patients with stage III non-small cell lung cancer? *Eur J Nucl Med Mol Imaging* [Internet]. 2006 [cited 2022 Mar 31]; 33(3):263–9. Available from: <https://doi.org/10.1007/s00259-005-1953-2>.

82. Hanin F-X, Lonneux M, Cornet J, Noirhomme P, Coulon C, Distexhe J, et al. Prognostic value of FDG uptake in early stage non-small cell lung cancer. *European Journal of Cardio-Thoracic Surgery* [Internet]. 2008 [cited 2022 Jan 14]; 33(5):819–23. Available from: <https://doi.org/10.1016/j.ejcts.2008.02.005>.
83. Vansteenkiste JF, Stroobants SG, Dupont PJ, Leyn PRD, Verbeken EK, Deneffe GJ, et al. Prognostic Importance of the Standardized Uptake Value on 18F-Fluoro-2-Deoxy-Glucose–Positron Emission Tomography Scan in Non–Small-Cell Lung Cancer: An Analysis of 125 Cases. *Journal of Clinical Oncology* [Internet]. American Society of Clinical Oncology; 2016 [cited 2022 Jan 14]. Available from: <https://ascopubs.org/doi/pdf/10.1200/JCO.1999.17.10.3201>.
84. Mertoğlu A, Üçvet A, Balci G, Aksel N, Batum Ö, Cireli E, et al. Correlation of preoperative PET/computer tomography 18F-fluorodeoxyglucose uptake (maximum standardized uptake value) with prognosis in patients with operated lung cancer. *Nuclear Medicine Communications* [Internet]. 2022 [cited 2022 Apr 1]; 43(4):475–82. Available from: https://journals.lww.com/nuclearmedicinecomm/Abstract/2022/04000/Correlation_of_preoperative_PET_computer.13.aspx.
85. Mostafa R, Abdelsamie Kandeel A, Abd Elkareem M, Nardo L, Abdelhafez YG. Pretherapy 18F-fluorodeoxyglucose positron emission tomography/computed tomography robust radiomic features predict overall survival in non-small cell lung cancer. *Nuclear Medicine Communications* [Internet]. 2022 [cited 2022 Apr 1]. Available from: https://journals.lww.com/nuclearmedicinecomm/Abstract/9000/Pretherapy_18F_fluorodeoxyglucose_positron.97915.aspx.
86. Dong M, Liu J, Sun X, Xing L. Prognostic significance of SUVmax on pretreatment 18F-FDG PET/CT in early-stage non-small cell lung cancer treated with stereotactic body radiotherapy: A meta-analysis. *Journal of Medical Imaging and Radiation Oncology* [Internet]. 2017 [cited 2022 Apr 1]; 61(5):652–9. Available from: <https://onlinelibrary.wiley.com/doi/abs/10.1111/1754-9485.12599>.
87. Clarke K, Taremi M, Dahele M, Freeman M, Fung S, Franks K, et al. Stereotactic body radiotherapy (SBRT) for non-small cell lung cancer (NSCLC): Is FDG-PET a predictor of outcome? *Radiotherapy and Oncology* [Internet]. Elsevier; 2012 [cited 2022 Apr 1]; 104(1):62–6. Available from: [https://www.thegreenjournal.com/article/S0167-8140\(12\)00223-X/abstract](https://www.thegreenjournal.com/article/S0167-8140(12)00223-X/abstract).
88. Takeda A, Yokosuka N, Ohashi T, Kunieda E, Fujii H, Aoki Y, et al. The maximum standardized uptake value (SUVmax) on FDG-PET is a strong predictor of local recurrence for localized non-small-cell lung cancer after stereotactic body radiotherapy (SBRT). *Radiotherapy and Oncology* [Internet]. Elsevier; 2011 [cited 2022 Apr 1]; 101(2):291–7. Available from: [https://www.thegreenjournal.com/article/S0167-8140\(11\)00458-0/abstract](https://www.thegreenjournal.com/article/S0167-8140(11)00458-0/abstract).
89. Zhang X, Liu H, Balter P, Allen PK, Komaki R, Pan T, et al. Positron Emission Tomography for Assessing Local Failure After Stereotactic Body Radiotherapy for Non-Small-Cell Lung Cancer. *International Journal of Radiation Oncology, Biology, Physics* [Internet]. Elsevier; 2012 [cited 2022 Apr 1]; 83(5):1558–65. Available from: [https://www.redjournal.org/article/S0360-3016\(11\)03442-0/abstract](https://www.redjournal.org/article/S0360-3016(11)03442-0/abstract).
90. Satoh Y, Nambu A, Onishi H, Sawada E, Tominaga L, Kuriyama K, et al. Value of dual time point F-18 FDG-PET/CT imaging for the evaluation of prognosis and risk factors for recurrence in patients with stage I non-small cell lung cancer treated with stereotactic body radiation therapy. *European Journal of Radiology* [Internet]. Elsevier; 2012 [cited 2022 Apr 1]; 81(11):3530–4. Available from: [https://www.ejradiology.com/article/S0720-048X\(11\)00825-4/abstract](https://www.ejradiology.com/article/S0720-048X(11)00825-4/abstract).
91. Lee DS, Kim YS, Yoo IR, Kang YN, Kim SJ, Oh JK, et al. Long-term clinical experience of high-dose ablative lung radiotherapy: High pre-treatment [18F]Fluorodeoxyglucose-positron emission

tomography maximal standardized uptake value of the primary tumor adversely affects treatment outcome. *Lung Cancer* [Internet]. Elsevier; 2013 [cited 2022 Apr 1]; 80(2):172–8. Available from: [https://www.lungcancerjournal.info/article/S0169-5002\(13\)00006-8/abstract](https://www.lungcancerjournal.info/article/S0169-5002(13)00006-8/abstract).

92. Chang JY, Liu H, Balter P, Komaki R, Liao Z, Welsh J, et al. Clinical outcome and predictors of survival and pneumonitis after stereotactic ablative radiotherapy for stage I non-small cell lung cancer. *Radiat Oncol* [Internet]. 2012 [cited 2022 Apr 1]; 7:152. Available from: <https://www.ncbi.nlm.nih.gov/pmc/articles/PMC3444889/>.
93. Liu J, Dong M, Sun X, Li W, Xing L, Yu J. Prognostic Value of 18F-FDG PET/CT in Surgical Non-Small Cell Lung Cancer: A Meta-Analysis. *PLOS ONE* [Internet]. Public Library of Science; 2016 [cited 2022 Apr 1]; 11(1):e0146195. Available from: <https://journals.plos.org/plosone/article?id=10.1371/journal.pone.0146195>.
94. Higashi K, Ueda Y, Arisaka Y, Sakuma T, Nambu Y, Oguchi M, et al. 18F-FDG Uptake as a Biologic Prognostic Factor for Recurrence in Patients with Surgically Resected Non-Small Cell Lung Cancer. *Journal of Nuclear Medicine* [Internet]. Society of Nuclear Medicine; 2002 [cited 2022 Jan 14]; 43(1):39–45. Available from: <https://jnm.snmjournals.org/content/43/1/39>.
95. Nair VS, Barnett PG, Ananth L, Gould MK. PET Scan 18F-Fluorodeoxyglucose Uptake and Prognosis in Patients With Resected Clinical Stage IA Non-small Cell Lung Cancer. *CHEST* [Internet]. Elsevier; 2010 [cited 2022 Jan 14]; 137(5):1150–6. Available from: [https://journal.chestnet.org/article/S0012-3692\(10\)60243-7/abstract](https://journal.chestnet.org/article/S0012-3692(10)60243-7/abstract).
96. Tomita M, Shimizu T, Ayabe T, Onitsuka T. Maximum SUV on positron emission tomography and serum CEA level as prognostic factors after curative resection for non-small cell lung cancer. *Asia-Pacific Journal of Clinical Oncology* [Internet]. 2012 [cited 2022 Jan 14]; 8(3):244–7. Available from: <https://onlinelibrary.wiley.com/doi/abs/10.1111/j.1743-7563.2012.01549.x>.
97. Hwang SH, Yoo MR, Park CH, Jeon TJ, Kim SJ, Kim TH. Dynamic contrast-enhanced CT to assess metabolic response in patients with advanced non-small cell lung cancer and stable disease after chemotherapy or chemoradiotherapy. *Eur Radiol* [Internet]. 2013 [cited 2022 Jan 27]; 23(6):1573–81. Available from: <https://doi.org/10.1007/s00330-012-2755-0>.
98. Hellwig D, Graeter TP, Ukena D, Georg T, Kirsch C-M, Schäfers H-J. Value of F-18-fluorodeoxyglucose positron emission tomography after induction therapy of locally advanced bronchogenic carcinoma. *The Journal of Thoracic and Cardiovascular Surgery* [Internet]. Elsevier; 2004 [cited 2022 Mar 31]; 128(6):892–9. Available from: [https://www.jtcvs.org/article/S0022-5223\(04\)01077-3/fulltext](https://www.jtcvs.org/article/S0022-5223(04)01077-3/fulltext).
99. Guerra JLL, Gladish G, Komaki R, Gomez D, Zhuang Y, Liao Z. Large Decreases in Standardized Uptake Values After Definitive Radiation Are Associated with Better Survival of Patients with Locally Advanced Non-Small Cell Lung Cancer. *Journal of Nuclear Medicine* [Internet]. Society of Nuclear Medicine; 2012 [cited 2022 Apr 1]; 53(2):225–33. Available from: <https://jnm.snmjournals.org/content/53/2/225>.
100. Bollineni VR, Widder J, Pruijm J, Langendijk JA, Wiegman EM. Residual 18F-FDG-PET Uptake 12 Weeks After Stereotactic Ablative Radiotherapy for Stage I Non-Small-Cell Lung Cancer Predicts Local Control. *International Journal of Radiation Oncology, Biology, Physics* [Internet]. Elsevier; 2012 [cited 2022 Apr 1]; 83(4):e551–5. Available from: [https://www.redjournal.org/article/S0360-3016\(12\)00055-7/abstract](https://www.redjournal.org/article/S0360-3016(12)00055-7/abstract).
101. Jiménez Londoño GA, García Vicente AM, Bosque JJ, Amo-Salas M, Pérez-Beteta J, Honguero-Martínez AF, et al. SUVmax to tumor perimeter distance: a robust radiomics prognostic biomarker

- in resectable non-small cell lung cancer patients. *Eur Radiol* [Internet]. 2022 [cited 2022 Apr 1]. Available from: <https://doi.org/10.1007/s00330-021-08523-3>.
102. Im H-J, Pak K, Cheon GJ, Kang KW, Kim S-J, Kim I-J, et al. Prognostic value of volumetric parameters of 18F-FDG PET in non-small-cell lung cancer: a meta-analysis. *Eur J Nucl Med Mol Imaging* [Internet]. 2015 [cited 2022 Apr 1]; 42(2):241–51. Available from: <https://doi.org/10.1007/s00259-014-2903-7>.
 103. Burdick MJ, Stephans KL, Reddy CA, Djemil T, Srinivas SM, Videtic GMM. Maximum Standardized Uptake Value From Staging FDG-PET/CT Does not Predict Treatment Outcome for Early-Stage Non-Small-Cell Lung Cancer Treated With Stereotactic Body Radiotherapy. *International Journal of Radiation Oncology, Biology, Physics* [Internet]. Elsevier; 2010 [cited 2022 Apr 1]; 78(4):1033–9. Available from: [https://www.redjournal.org/article/S0360-3016\(09\)03584-6/abstract](https://www.redjournal.org/article/S0360-3016(09)03584-6/abstract).
 104. Liao S, Penney BC, Wroblewski K, Zhang H, Simon CA, Kampalath R, et al. Prognostic value of metabolic tumor burden on 18F-FDG PET in nonsurgical patients with non-small cell lung cancer. *Eur J Nucl Med Mol Imaging* [Internet]. 2012 [cited 2022 Jan 14]; 39(1):27–38. Available from: <https://doi.org/10.1007/s00259-011-1934-6>.
 105. Im H-J, Bradshaw T, Solaiyappan M, Cho SY. Current Methods to Define Metabolic Tumor Volume in Positron Emission Tomography: Which One is Better? *Nucl Med Mol Imaging* [Internet]. 2018 [cited 2022 Jan 10]; 52(1):5–15. Available from: <https://www.ncbi.nlm.nih.gov/pmc/articles/PMC5777960/>.
 106. Unterrainer M, Taugner J, Käsmann L, Tufman A, Reinmuth N, Li M, et al. Differential role of residual metabolic tumor volume in inoperable stage III NSCLC after chemoradiotherapy ± immune checkpoint inhibition. *Eur J Nucl Med Mol Imaging* [Internet]. 2022 [cited 2022 Apr 1]; 49(4):1407–16. Available from: <https://www.ncbi.nlm.nih.gov/pmc/articles/PMC8921088/>.
 107. Eude F, Guisier F, Salaün M, Thiberville L, Pressat-Laffouilhère T, Vera P, et al. Prognostic value of total tumour volume, adding necrosis to metabolic tumour volume, in advanced or metastatic non-small cell lung cancer treated with first-line pembrolizumab. *Ann Nucl Med* [Internet]. 2022 [cited 2022 Apr 1]; 36(3):224–34. Available from: <https://doi.org/10.1007/s12149-021-01694-5>.
 108. Miles KA. Measurement of tissue perfusion by dynamic computed tomography. *BJR* [Internet]. The British Institute of Radiology; 1991 [cited 2022 Feb 11]; 64(761):409–12. Available from: <https://www.birpublications.org/doi/10.1259/0007-1285-64-761-409>.
 109. Miles KA. Functional CT imaging in oncology. *Eur Radiol* [Internet]. 2003 [cited 2022 Feb 14]; 13(5):134–8. Available from: <https://doi.org/10.1007/s00330-003-2108-0>.
 110. Miles KA, Charnsangavej C, Lee FT, Fishman EK, Horton K, Lee TY. Application of CT in the investigation of angiogenesis in oncology. *Acad Radiol*. 2000; 7(10):840–50.
 111. Djuric-Stefanovic A, Saranovic D, Masulovic D, Ivanovic A, Pesko P. Comparison between the deconvolution and maximum slope 64-MDCT perfusion analysis of the esophageal cancer: Is conversion possible? *European Journal of Radiology* [Internet]. Elsevier; 2013 [cited 2022 Feb 15]; 82(10):1716–23. Available from: [https://www.ejradiology.com/article/S0720-048X\(13\)00293-3/fulltext](https://www.ejradiology.com/article/S0720-048X(13)00293-3/fulltext).
 112. Goh V, Halligan S, Bartram CI. Quantitative Tumor Perfusion Assessment with Multidetector CT: Are Measurements from Two Commercial Software Packages Interchangeable? *Radiology* [Internet]. Radiological Society of North America; 2007 [cited 2021 Dec 20]; 242(3):777–82. Available from: <https://pubs.rsna.org/doi/10.1148/radiol.2423060279>.

113. Cuenod CA, Balvay D. Perfusion and vascular permeability: Basic concepts and measurement in DCE-CT and DCE-MRI. *Diagnostic and Interventional Imaging* [Internet]. 2013 [cited 2019 Nov 19]; 94(12):1187–204. Available from: <http://www.sciencedirect.com/science/article/pii/S2211568413003306>.
114. Cuenod CA, Leconte I, Siauve N, Frouin F, Dromain C, Clément O, et al. Deconvolution Technique for Measuring Tissue Perfusion by Dynamic CT: Application to Normal and Metastatic Liver. *Academic Radiology* [Internet]. Elsevier; 2002 [cited 2022 Feb 11]; 9(1):S205–11. Available from: [https://www.academicradiology.org/article/S1076-6332\(03\)80437-3/fulltext](https://www.academicradiology.org/article/S1076-6332(03)80437-3/fulltext).
115. Mazzei MA, Squitieri NC, Sani E, Guerrini S, Imbriaco G, Di Lucia D, et al. Differences in perfusion CT parameter values with commercial software upgrades: a preliminary report about algorithm consistency and stability. *Acta Radiol* [Internet]. SAGE Publications; 2013 [cited 2021 Dec 17]; 54(7):805–11. Available from: <https://doi.org/10.1177/0284185113484643>.
116. Ng Q-S, Goh V, Fichte H, Klotz E, Fernie P, Saunders MI, et al. Lung Cancer Perfusion at Multi-Detector Row CT: Reproducibility of Whole Tumor Quantitative Measurements. *Radiology* [Internet]. Radiological Society of North America; 2006 [cited 2021 Dec 17]; 239(2):547–53. Available from: <https://pubs.rsna.org/doi/10.1148/radiol.2392050568>.
117. Han K, Yoon KW, Kim JH, Kim GM. Bronchial Artery Embolization for Hemoptysis in Primary Lung Cancer: A Retrospective Review of 84 Patients. *Journal of Vascular and Interventional Radiology* [Internet]. Elsevier; 2019 [cited 2022 Jan 28]; 30(3):428–34. Available from: [https://www.jvir.org/article/S1051-0443\(18\)31444-1/fulltext](https://www.jvir.org/article/S1051-0443(18)31444-1/fulltext).
118. Eldridge L, Moldobaeva A, Zhong Q, Jenkins J, Snyder M, Brown RH, et al. Bronchial Artery Angiogenesis Drives Lung Tumor Growth. *Cancer Res* [Internet]. American Association for Cancer Research; 2016 [cited 2022 Jan 28]; 76(20):5962–9. Available from: <https://cancerres.aacrjournals.org/content/76/20/5962>.
119. Yuan X, Zhang J, Ao G, Quan C, Tian Y, Li H. Lung cancer perfusion: can we measure pulmonary and bronchial circulation simultaneously? *Eur Radiol* [Internet]. 2012 [cited 2021 Dec 16]; 22(8):1665–71. Available from: <https://doi.org/10.1007/s00330-012-2414-5>.
120. Boas FE, Kemeny NE, Sofocleous CT, Yeh R, Thompson VR, Hsu M, et al. Bronchial or Pulmonary Artery Chemoembolization for Unresectable and Unablatable Lung Metastases: A Phase I Clinical Trial. *Radiology* [Internet]. Radiological Society of North America; 2021 [cited 2022 Jan 28]; 301(2):474–84. Available from: <https://pubs.rsna.org/doi/10.1148/radiol.2021210213>.
121. Li XS, Fan HX, Fang H, Huang H, Song YL, Zhou CW. Value of Whole-Tumor Dual-Input Perfusion CT in Predicting the Effect of Multiarterial Infusion Chemotherapy on Advanced Non-Small Cell Lung Cancer. *American Journal of Roentgenology* [Internet]. American Roentgen Ray Society; 2014 [cited 2022 Jan 26]; 203(5):W497–505. Available from: <https://www.ajronline.org/doi/10.2214/AJR.13.11621>.
122. Deng L, Tang H, Qiang J, Wang J, Xiao S. Blood Supply of Early Lung Adenocarcinomas in Mice and the Tumor-supplying Vessel Relationship: A Micro-CT Angiography Study. *Cancer Prev Res* [Internet]. American Association for Cancer Research; 2020 [cited 2022 Jan 28]; 13(12):989–96. Available from: <https://cancerpreventionresearch.aacrjournals.org/content/13/12/989>.
123. Nguyen-Kim TDL, Frauenfelder T, Strobel K, Veit-Haibach P, Huellner MW. Assessment of bronchial and pulmonary blood supply in non-small cell lung cancer subtypes using computed tomography perfusion. *Investigative Radiology* [Internet]. Lippincott Williams & Wilkins; 2015 [cited 2022 Feb 4]; 50(3):179–86. Available from: <https://www.zora.uzh.ch/id/eprint/103173/>.

124. Chu LL, Knebel RJ, Shay AD, Santos J, Badawi RD, Gandara DR, et al. CT perfusion imaging of lung cancer: benefit of motion correction for blood flow estimates. *Eur Radiol* [Internet]. 2018 [cited 2021 Dec 16]; 28(12):5069–75. Available from: <https://doi.org/10.1007/s00330-018-5492-1>.
125. Bevilacqua A, Barone D, Malavasi S, Gavelli G. Quantitative Assessment of Effects of Motion Compensation for Liver and Lung Tumors in CT Perfusion. *Academic Radiology* [Internet]. Elsevier; 2014 [cited 2022 Feb 15]; 21(11):1416–26. Available from: [https://www.academicradiology.org/article/S1076-6332\(14\)00233-5/fulltext](https://www.academicradiology.org/article/S1076-6332(14)00233-5/fulltext).
126. Ohno Y, Koyama H, Matsumoto K, Onishi Y, Takenaka D, Fujisawa Y, et al. Differentiation of Malignant and Benign Pulmonary Nodules with Quantitative First-Pass 320–Detector Row Perfusion CT versus FDG PET/CT. *Radiology* [Internet]. 2011 [cited 2019 Nov 19]; 258(2):599–609. Available from: <https://pubs.rsna.org/doi/10.1148/radiol.10100245>.
127. Chandler A, Wei W, Herron DH, Anderson EF, Johnson VE, Ng CS. Semiautomated Motion Correction of Tumors in Lung CT-perfusion Studies. *Academic Radiology* [Internet]. Elsevier; 2011 [cited 2022 Feb 15]; 18(3):286–93. Available from: [https://www.academicradiology.org/article/S1076-6332\(10\)00576-3/fulltext](https://www.academicradiology.org/article/S1076-6332(10)00576-3/fulltext).
128. García-Figueiras R, Goh VJ, Padhani AR, Baleato-González S, Garrido M, León L, et al. CT Perfusion in Oncologic Imaging: A Useful Tool? *American Journal of Roentgenology* [Internet]. 2013 [cited 2019 Nov 18]; 200(1):8–19. Available from: <http://www.ajronline.org/doi/abs/10.2214/AJR.11.8476>.
129. Miles KA, Lee T-Y, Goh V, Klotz E, Cuenod C, Bisdas S, et al. Current status and guidelines for the assessment of tumour vascular support with dynamic contrast-enhanced computed tomography. *Eur Radiol* [Internet]. 2012 [cited 2022 Feb 18]; 22(7):1430–41. Available from: <https://doi.org/10.1007/s00330-012-2379-4>.
130. Huang T, Sun H, Luo X, Zhang X, Jin K, Wang F, et al. Correlation study between flash dual source CT perfusion imaging and regional lymph node metastasis of non-small cell lung cancer. *BMC Cancer* [Internet]. 2020 [cited 2021 Dec 16]; 20(1):547. Available from: <https://doi.org/10.1186/s12885-020-07032-8>.
131. Tateishi U, Nishihara H, Watanabe S, Morikawa T, Abe K, Miyasaka K. Tumor angiogenesis and dynamic CT in lung adenocarcinoma: radiologic-pathologic correlation. *J Comput Assist Tomogr* [Internet]. 2001 [cited 2022 Feb 14]; 25(1):23–7. Available from: <https://doi.org/10.1097/00004728-200101000-00004>.
132. Spira D, Neumeister H, Spira SM, Hetzel J, Spengler W, Weyhern CH von, et al. Assessment of Tumor Vascularity in Lung Cancer Using Volume Perfusion CT (VPCT) With Histopathologic Comparison: A Further Step Toward an Individualized Tumor Characterization. *Journal of Computer Assisted Tomography* [Internet]. 2013 [cited 2022 Feb 24]; 37(1):15–21. Available from: https://journals.lww.com/jcat/Abstract/2013/01000/Assessment_of_Tumor_Vascularity_in_Lung_Cancer.3.aspx.
133. Sauter AW, Winterstein S, Spira D, Hetzel J, Schulze M, Mueller M, et al. Multifunctional Profiling of Non–Small Cell Lung Cancer Using 18F-FDG PET/CT and Volume Perfusion CT. *Journal of Nuclear Medicine* [Internet]. Society of Nuclear Medicine; 2012 [cited 2022 Feb 24]; 53(4):521–9. Available from: <https://jnm.snmjournals.org/content/53/4/521>.
134. Mineo TC, Ambrogi V, Baldi A, Rabitti C, Bollero P, Vincenzi B, et al. Prognostic impact of VEGF, CD31, CD34, and CD105 expression and tumour vessel invasion after radical surgery for IB–IIA non-small cell lung cancer. *Journal of Clinical Pathology* [Internet]. 2004 [cited 2019 Oct 31]; 57(6):591–7. Available from: <https://jcp.bmj.com/content/57/6/591>.

135. Weidner N. Current pathologic methods for measuring intratumoral microvessel density within breast carcinoma and other solid tumors. *Breast Cancer Res Tr* [Internet]. 1995 [cited 2021 Dec 16]; 36(2):169–80. Available from: <https://doi.org/10.1007/BF00666038>.
136. Weidner N, Semple JP, Welch WR, Folkman J. Tumor Angiogenesis and Metastasis — Correlation in Invasive Breast Carcinoma. *N Engl J Med* [Internet]. Massachusetts Medical Society; 1991 [cited 2022 Feb 21]; 324(1):1–8. Available from: <https://www.nejm.org/doi/10.1056/NEJM199101033240101>.
137. Chen M-L, Wei Y-Y, Li X-T, Qi L-P, Sun Y-S. Low-dose spectral CT perfusion imaging of lung cancer quantitative analysis in different pathological subtypes. *Transl Cancer Res* [Internet]. 2021 [cited 2022 Feb 18]; 10(6):2841–8. Available from: <https://www.ncbi.nlm.nih.gov/pmc/articles/PMC8797941/>.
138. Ovali GY, Sakar A, Gökten C, Çelik P, Yorgancıoğlu A, Nese N, et al. Thorax perfusion CT in non-small cell lung cancer. *Computerized Medical Imaging and Graphics* [Internet]. 2007 [cited 2022 Feb 18]; 31(8):686–91. Available from: <https://www.sciencedirect.com/science/article/pii/S0895611107001310>.
139. Fraioli F, Anzidei M, Serra G, Liberali S, Fiorelli A, Zaccagna F, et al. Whole-tumour CT-perfusion of unresectable lung cancer for the monitoring of anti-angiogenetic chemotherapy effects. *BJR* [Internet]. The British Institute of Radiology; 2013 [cited 2021 Dec 16]; 86(1029):20120174. Available from: <https://www.birpublications.org/doi/10.1259/bjr.20120174>.
140. Fraioli F, Anzidei M, Zaccagna F, Mennini ML, Serra G, Gori B, et al. Whole-Tumor Perfusion CT in Patients with Advanced Lung Adenocarcinoma Treated with Conventional and Antiangiogenetic Chemotherapy: Initial Experience. *Radiology* [Internet]. 2011 [cited 2019 Nov 26]; 259(2):574–82. Available from: <https://pubs.rsna.org/doi/10.1148/radiol.11100600>.
141. Shi L, Zhou X-L, Sun J-J, Huang J-H, Wang X, Li K, et al. Whole-tumor perfusion CT using texture analysis in unresectable stage IIIA/B non-small cell lung cancer treated with recombinant human endostatin. *Quantitative Imaging in Medicine and Surgery* [Internet]. AME Publishing Company; 2019 [cited 2021 Dec 16]; 9(6):96875–975. Available from: <https://qims.amegroups.com/article/view/26541>.
142. Tacelli N, Remy-Jardin M, Copin M-C, Scherpereel A, Mensier E, Jaillard S, et al. Assessment of Non–Small Cell Lung Cancer Perfusion: Pathologic-CT Correlation in 15 Patients. *Radiology* [Internet]. 2010 [cited 2019 Nov 26]; 257(3):863–71. Available from: <https://pubs.rsna.org/doi/10.1148/radiol.10100181>.
143. Miles KA, Griffiths MR, Fuentes MA. Standardized Perfusion Value: Universal CT Contrast Enhancement Scale that Correlates with FDG PET in Lung Nodules. *Radiology* [Internet]. 2001 [cited 2019 Oct 31]; 220(2):548–53. Available from: <https://pubs.rsna.org/doi/10.1148/radiology.220.2.r01au26548>.
144. Yang L, Sun L, Liu J, Liu Q. Role of low dose 256-slice CT perfusion imaging in predicting mediastinal lymph node metastasis of lung cancer. *Rev Assoc Med Bras* [Internet]. Associação Médica Brasileira; 2019 [cited 2021 Dec 16]; 65:761–6. Available from: <http://www.scielo.br/j/ramb/a/F5VLMjWwJVvfZXZYrz3v5YL/?lang=en>.
145. Tacelli N, Santangelo T, Scherpereel A, Duhamel A, Deken V, Klotz E, et al. Perfusion CT allows prediction of therapy response in non-small cell lung cancer treated with conventional and anti-angiogenic chemotherapy. *Eur Radiol* [Internet]. 2013 [cited 2021 Dec 16]; 23(8):2127–36. Available from: <https://doi.org/10.1007/s00330-013-2821-2>.

146. Yang D-M, Palma DA, Kwan K, Louie AV, Malthaner R, Fortin D, et al. Predicting pathological complete response (pCR) after stereotactic ablative radiation therapy (SABR) of lung cancer using quantitative dynamic [¹⁸F]FDG PET and CT perfusion: a prospective exploratory clinical study. *Radiat Oncol* [Internet]. 2021 [cited 2022 Feb 24]; 16:11. Available from: <https://www.ncbi.nlm.nih.gov/pmc/articles/PMC7805034/>.
147. Sudarski S, Hagelstein C, Weis M, Schoenberg SO, Apfaltrer P. Dual-energy snap-shot perfusion CT in suspect pulmonary nodules and masses and for lung cancer staging. *European Journal of Radiology* [Internet]. Elsevier; 2015 [cited 2021 Dec 16]; 84(12):2393–400. Available from: [https://www.ejradiology.com/article/S0720-048X\(15\)30116-9/fulltext](https://www.ejradiology.com/article/S0720-048X(15)30116-9/fulltext).
148. Yuan X, Zhang J, Quan C, Cao J, Ao G, Tian Y, et al. Differentiation of malignant and benign pulmonary nodules with first-pass dual-input perfusion CT. *Eur Radiol* [Internet]. 2013 [cited 2019 Nov 19]; 23(9):2469–74. Available from: <https://doi.org/10.1007/s00330-013-2842-x>.
149. Huang C, Liang J, Lei X, Xu X, Xiao Z, Luo L. Diagnostic Performance of Perfusion Computed Tomography for Differentiating Lung Cancer from Benign Lesions: A Meta-Analysis. *Med Sci Monit* [Internet]. 2019 [cited 2022 Feb 24]; 25:3485–94. Available from: <https://www.ncbi.nlm.nih.gov/pmc/articles/PMC6526743/>.
150. Win T, Miles KA, Janes SM, Ganeshan B, Shastry M, Endozo R, et al. Tumor Heterogeneity and Permeability as Measured on the CT Component of PET/CT Predict Survival in Patients with Non-Small Cell Lung Cancer. *Clin Cancer Res* [Internet]. 2013 [cited 2020 Apr 2]; 19(13):3591–9. Available from: <https://clincancerres.aacrjournals.org/content/19/13/3591>.
151. Huellner MW, Collen TD, Gut P, Winterhalder R, Pauli C, Diebold J, et al. Multiparametric PET/CT-perfusion does not add significant additional information for initial staging in lung cancer compared with standard PET/CT. *EJNMMI Res* [Internet]. 2014 [cited 2019 Nov 18]; 4:6. Available from: <https://www.ncbi.nlm.nih.gov/pmc/articles/PMC3901766/>.
152. Haralick RM, Shanmugam K, Dinstein I. Textural Features for Image Classification. *IEEE Transactions on Systems, Man, and Cybernetics*. 1973; SMC-3(6):610–21.
153. Julesz B. Experiments in the visual perception of texture. *Sci Am*. 1975; 232(4):34–43.
154. Galloway MM. Texture analysis using gray level run lengths. *Computer Graphics and Image Processing* [Internet]. 1975 [cited 2022 Apr 21]; 4(2):172–9. Available from: <https://www.sciencedirect.com/science/article/pii/S0146664X75800086>.
155. Haralick RM. Statistical and structural approaches to texture. *Proceedings of the IEEE*. 1979; 67(5):786–804.
156. Amadasun M, King R. Textural features corresponding to textural properties. *IEEE Transactions on Systems Man and Cybernetics*. 1989; 19(5):1264–74.
157. He D-C, Wang L. Texture features based on texture spectrum. *Pattern Recognition* [Internet]. 1991 [cited 2022 Apr 21]; 24(5):391–9. Available from: <https://www.sciencedirect.com/science/article/pii/0031320391900527>.
158. Castellano G, Bonilha L, Li LM, Cendes F. Texture analysis of medical images. *Clinical Radiology* [Internet]. Elsevier; 2004 [cited 2022 Apr 21]; 59(12):1061–9. Available from: [https://www.clinicalradiologyonline.net/article/S0009-9260\(04\)00265-X/fulltext](https://www.clinicalradiologyonline.net/article/S0009-9260(04)00265-X/fulltext).

159. Maria Petrou, Pedro García Sevilla. Image Processing: Dealing with Texture [Internet]. John Wiley & Sons, Ltd; 2006 [cited 2022 Apr 21]. Available from: <https://onlinelibrary.wiley.com/doi/book/10.1002/047003534X>.
160. Thibault G, FERTIL B, Navarro C, Pereira S, Lévy N, Sequeira J, et al. Texture Indexes and Gray Level Size Zone Matrix Application to Cell Nuclei Classification. 2009.
161. Ganeshan B, Miles KA, Young RCD, Chatwin CR. Texture analysis in non-contrast enhanced CT: Impact of malignancy on texture in apparently disease-free areas of the liver. *European Journal of Radiology* [Internet]. Elsevier; 2009 [cited 2022 Apr 21]; 70(1):101–10. Available from: [https://www.ejradiology.com/article/S0720-048X\(07\)00607-9/fulltext](https://www.ejradiology.com/article/S0720-048X(07)00607-9/fulltext).
162. Lopes R, Betrouni N. Fractal and multifractal analysis: A review. *Medical Image Analysis* [Internet]. 2009 [cited 2022 Apr 21]; 13(4):634–49. Available from: <https://www.sciencedirect.com/science/article/pii/S1361841509000395>.
163. Armi L, Fekri-Ershad S. Texture image analysis and texture classification methods - A review. arXiv:1904.06554 [cs] [Internet]. 2019 [cited 2022 Apr 21]. Available from: <http://arxiv.org/abs/1904.06554>.
164. Xu Y, Yang X, Ling H, Ji H. A new texture descriptor using multifractal analysis in multi-orientation wavelet pyramid. 2010 IEEE Computer Society Conference on Computer Vision and Pattern Recognition [Internet]. San Francisco, CA, USA: IEEE; 2010 [cited 2022 Apr 21]. Available from: <http://ieeexplore.ieee.org/document/5540217/>.
165. Cross GR, Jain AK. Markov random field texture models. *IEEE Trans Pattern Anal Mach Intell*. 1983; 5(1):25–39.
166. Mao J, Jain AK. Texture classification and segmentation using multiresolution simultaneous autoregressive models. *Pattern Recognit*. 1992.
167. Procter AJ, Jacob J. Visual vs. computer-based computed tomography analysis for the identification of functional patterns in interstitial lung diseases. *Curr Opin Pulm Med*. 2019; 25(5):426–33.
168. Shi B, Zhang G-M-Y, Xu M, Jin Z-Y, Sun H. Distinguishing metastases from benign adrenal masses: what can CT texture analysis do? *Acta Radiol* [Internet]. SAGE Publications; 2019 [cited 2022 May 4]; 60(11):1553–61. Available from: <https://doi.org/10.1177/0284185119830292>.
169. Yu H, Parakh A, Blake M, McDermott S. Texture Analysis as a Radiomic Marker for Differentiating Benign From Malignant Adrenal Tumors. *Journal of Computer Assisted Tomography* [Internet]. 2020 [cited 2022 May 4]; 44(5):766–71. Available from: <https://journals.lww.com/jcat/pages/articleviewer.aspx?year=2020&issue=09000&article=00021&type=Fulltext>.
170. Andersen MB, Bodtger U, Andersen IR, Thorup KS, Ganeshan B, Rasmussen F. Metastases or benign adrenal lesions in patients with histopathological verification of lung cancer: Can CT texture analysis distinguish? *European Journal of Radiology* [Internet]. Elsevier; 2021 [cited 2022 May 4]; 138. Available from: [https://www.ejradiology.com/article/S0720-048X\(21\)00144-3/fulltext](https://www.ejradiology.com/article/S0720-048X(21)00144-3/fulltext).
171. Ren Z, Che J, Wu XW, Xia J. Analysis of KRAS Mutation Status Prediction Model for Colorectal Cancer Based on Medical Imaging. *Computational and Mathematical Methods in Medicine* [Internet]. Hindawi; 2021 [cited 2022 May 4]; 2021:e3953442. Available from: <https://www.hindawi.com/journals/cmmm/2021/3953442/>.

172. Rajamohan N, Goyal A, Kandasamy D, Bhalla AS, Parshad R, Jain D, et al. CT texture analysis in evaluation of thymic tumors and thymic hyperplasia: correlation with the international thymic malignancy interest group (ITMIG) stage and WHO grade. *BJR* [Internet]. The British Institute of Radiology; 2021 [cited 2022 May 4]; 94(1128):20210583. Available from: <https://www.birpublications.org/doi/10.1259/bjr.20210583>.
173. Guerrisi A, Russillo M, Loi E, Ganeshan B, Ungania S, Desiderio F, et al. Exploring CT Texture Parameters as Predictive and Response Imaging Biomarkers of Survival in Patients With Metastatic Melanoma Treated With PD-1 Inhibitor Nivolumab: A Pilot Study Using a Delta-Radiomics Approach. *Frontiers in Oncology* [Internet]. 2021 [cited 2022 May 4]; 11. Available from: <https://www.frontiersin.org/article/10.3389/fonc.2021.704607>.
174. Brown AL, Jeong J, Wahab RA, Zhang B, Mahoney MC. Diagnostic accuracy of MRI textural analysis in the classification of breast tumors. *Clinical Imaging* [Internet]. Elsevier; 2021 [cited 2022 May 4]; 77:86–91. Available from: [https://www.clinicalimaging.org/article/S0899-7071\(21\)00087-5/fulltext](https://www.clinicalimaging.org/article/S0899-7071(21)00087-5/fulltext).
175. MacIver CL, Busaidi AA, Ganeshan B, Maynard JA, Wastling S, Hyare H, et al. Filtration-Histogram Based Magnetic Resonance Texture Analysis (MRTA) for the Distinction of Primary Central Nervous System Lymphoma and Glioblastoma. *Journal of Personalized Medicine* [Internet]. Multidisciplinary Digital Publishing Institute; 2021 [cited 2022 May 4]; 11(9):876. Available from: <https://www.mdpi.com/2075-4426/11/9/876>.
176. Song SE, Seo BK, Cho KR, Woo OH, Ganeshan B, Kim ES, et al. Prediction of Inflammatory Breast Cancer Survival Outcomes Using Computed Tomography-Based Texture Analysis. *Frontiers in Bioengineering and Biotechnology* [Internet]. 2021 [cited 2022 May 4]; 9. Available from: <https://www.frontiersin.org/article/10.3389/fbioe.2021.695305>.
177. An H, Wang Y, Wong EMF, Lyu S, Han L, Perucho JAU, et al. CT texture analysis in histological classification of epithelial ovarian carcinoma. *Eur Radiol* [Internet]. 2021 [cited 2022 May 4]; 31(7):5050–8. Available from: <https://doi.org/10.1007/s00330-020-07565-3>.
178. Agazzi GM, Ravanelli M, Roca E, Medicina D, Balzarini P, Pessina C, et al. CT texture analysis for prediction of EGFR mutational status and ALK rearrangement in patients with non-small cell lung cancer. *Radiol med* [Internet]. 2021 [cited 2022 May 4]; 126(6):786–94. Available from: <https://doi.org/10.1007/s11547-020-01323-7>.
179. Park H, Qin L, Guerra P, Bay CP, Shinagare AB. Decoding incidental ovarian lesions: use of texture analysis and machine learning for characterization and detection of malignancy. *Abdom Radiol* [Internet]. 2021 [cited 2022 May 4]; 46(6):2376–83. Available from: <https://doi.org/10.1007/s00261-020-02668-3>.
180. Szychot E, Youssef A, Ganeshan B, Endozo R, Hyare H, Gains J, et al. Predicting outcome in childhood diffuse midline gliomas using magnetic resonance imaging based texture analysis. *J Neuroradiol*. 2021; 48(4):243–7.
181. Ganeshan B, Abaleke S, Young RCD, Chatwin CR, Miles KA. Texture analysis of non-small cell lung cancer on unenhanced computed tomography: initial evidence for a relationship with tumour glucose metabolism and stage. *Cancer Imaging* [Internet]. 2010 [cited 2022 Apr 20]; 10(1):137–43. Available from: <https://www.ncbi.nlm.nih.gov/pmc/articles/PMC2904029/>.
182. Ganeshan B, Miles K, Afaq A, Punwani S, Rodriguez M, Wan S, et al. Texture Analysis of Fractional Water Content Images Acquired during PET/MRI: Initial Evidence for an Association with Total Lesion Glycolysis, Survival and Gene Mutation Profile in Primary Colorectal Cancer. *Cancers*

- [Internet]. Multidisciplinary Digital Publishing Institute; 2021 [cited 2022 May 4]; 13(11):2715. Available from: <https://www.mdpi.com/2072-6694/13/11/2715>.
183. Ganeshan B, Goh V, Mandeville HC, Ng QS, Hoskin PJ, Miles KA. Non–Small Cell Lung Cancer: Histopathologic Correlates for Texture Parameters at CT. *Radiology* [Internet]. Radiological Society of North America; 2013 [cited 2022 Apr 20]; 266(1):326–36. Available from: <https://pubs.rsna.org/doi/10.1148/radiol.12112428>.
 184. Groves AM, Kayani I, Dickson JC, Townsend C, Croasdale I, Syed R, et al. Oral contrast medium in PET/CT: should you or shouldn't you? *Eur J Nucl Med Mol Imaging* [Internet]. 2005 [cited 2021 Dec 17]; 32(10):1160–6. Available from: <https://doi.org/10.1007/s00259-005-1833-9>.
 185. General Electric Company,. *CT Perfusion 4 User Guide*. 2011.
 186. Groves AM, Shastry M, Rodriguez-Justo M, Malhotra A, Endozo R, Davidson T, et al. 18F-FDG PET and biomarkers for tumour angiogenesis in early breast cancer. *Eur J Nucl Med Mol Imaging* [Internet]. 2011 [cited 2022 Aug 8]; 38(1):46–52. Available from: <https://doi.org/10.1007/s00259-010-1590-2>.
 187. Yao Y, Pan Y, Chen J, Sun X, Qiu Y, Ding Y. Endoglin (CD105) Expression in Angiogenesis of Primary Hepatocellular Carcinomas: Analysis using Tissue Microarrays and Comparisons with CD34 and VEGF. *Ann Clin Lab Sci* [Internet]. Association of Clinical Scientists; 2007 [cited 2022 Aug 8]; 37(1):39–48. Available from: <http://www.annclinlabsci.org/content/37/1/39>.
 188. Uzzan B, Nicolas P, Cucherat M, Perret G-Y. Microvessel density as a prognostic factor in women with breast cancer: a systematic review of the literature and meta-analysis. *Cancer Res*. 2004; 64(9):2941–55.
 189. R Core Team. *R: A Language and Environment for Statistical Computing* [Internet]. Vienna, Austria: R Foundation for Statistical Computing; 2020. Available from: <https://www.R-project.org/>.
 190. Therneau TM. *A Package for Survival Analysis in S* [Internet]. 2015. Available from: <https://CRAN.R-project.org/package=survival>.
 191. Terry M. Therneau, Patricia M. Grambsch. *Modeling Survival Data: Extending the Cox Model*. New York: Springer; 2000.
 192. Wickham H. *ggplot2: Elegant Graphics for Data Analysis* [Internet]. Springer-Verlag New York; 2016. Available from: <https://ggplot2.tidyverse.org>.
 193. Wickham H, Averick M, Bryan J, Chang W, McGowan LD, François R, et al. Welcome to the tidyverse. *Journal of Open Source Software*. 2019; 4(43):1686.
 194. Heagerty PJ, Saha-Chaudhuri packaging by P. *survivalROC: Time-dependent ROC curve estimation from censored survival data* [Internet]. 2013. Available from: <https://CRAN.R-project.org/package=survivalROC>.
 195. Yousefi-Koma A, Panah-Moghaddam M, Kalff V. The Utility of Metabolic Imaging by 18F-FDG PET/CT in Lung Cancer: Impact on Diagnosis and Staging. *Tanaffos* [Internet]. 2013 [cited 2021 Dec 22]; 12(1):16–25. Available from: <https://www.ncbi.nlm.nih.gov/pmc/articles/PMC4153235/>.
 196. Brenner H, Rachet B. Hybrid analysis for up-to-date long-term survival rates in cancer registries with delayed recording of incident cases. *European Journal of Cancer* [Internet]. Elsevier; 2004 [cited 2022 Jan 14]; 40(16):2494–501. Available from: [https://www.ejancer.com/article/S0959-8049\(04\)00608-2/fulltext](https://www.ejancer.com/article/S0959-8049(04)00608-2/fulltext).

197. Chen DL, Mintun MA, Schuster DP. Comparison of Methods to Quantitate 18F-FDG Uptake with PET During Experimental Acute Lung Injury. *Journal of Nuclear Medicine* [Internet]. Society of Nuclear Medicine; 2004 [cited 2022 Jan 14]; 45(9):1583–90. Available from: <https://jnm.snmjournals.org/content/45/9/1583>.
198. Hunter GJ, Hamberg LM, Alpert NM, Choi NC, Fischman AJ. Simplified Measurement of Deoxyglucose Utilization Rate. *J Nucl Med* [Internet]. Society of Nuclear Medicine; 1996 [cited 2020 Apr 27]; 37(6):950–5. Available from: <http://jnm.snmjournals.org/content/37/6/950>.
199. Krak NC, Hoeven JJM van der, Hoekstra OS, Twisk JWR, Wall E van der, Lammertsma AA. Measuring [18F]FDG uptake in breast cancer during chemotherapy: comparison of analytical methods. *Eur J Nucl Med Mol Imaging* [Internet]. 2003 [cited 2020 Apr 29]; 30(5):674–81. Available from: <https://doi.org/10.1007/s00259-003-1127-z>.
200. Kiessling F, Boese J, Corvinus C, Ederle JR, Zuna I, Schoenberg SO, et al. Perfusion CT in patients with advanced bronchial carcinomas: a novel chance for characterization and treatment monitoring? *Eur Radiol* [Internet]. 2004 [cited 2022 Jan 27]; 14(7):1226–33. Available from: <https://doi.org/10.1007/s00330-004-2288-2>.
201. Hori S, Nakamura T, Kennoki N, Dejima I, Hori A. Transarterial management of advance lung cancer. *Jpn J Clin Oncol* [Internet]. 2021 [cited 2022 Jan 28]; 51(6):851–6. Available from: <https://www.ncbi.nlm.nih.gov/pmc/articles/PMC8163058/>.
202. Chen X, Xu Y, Duan J, Li C, Sun H, Wang W. Correlation of iodine uptake and perfusion parameters between dual-energy CT imaging and first-pass dual-input perfusion CT in lung cancer. *Medicine (Baltimore)* [Internet]. 2017 [cited 2022 Jan 26]; 96(28):e7479. Available from: <https://www.ncbi.nlm.nih.gov/pmc/articles/PMC5515760/>.
203. Meyer CR, Armato SG, Fenimore CP, McLennan G, Bidautn LM, Barboriak DP, et al. Quantitative Imaging to Assess Tumor Response to Therapy: Common Themes of Measurement, Truth Data, and Error Sources. *Translational Oncology* [Internet]. 2009 [cited 2019 Oct 30]; 2(4):198–210. Available from: <http://www.sciencedirect.com/science/article/pii/S1936523309800259>.
204. Nelson DA, Tan T-T, Rabson AB, Anderson D, Degenhardt K, White E. Hypoxia and defective apoptosis drive genomic instability and tumorigenesis. *Genes Dev* [Internet]. 2004 [cited 2022 May 26]; 18(17):2095–107. Available from: <https://www.ncbi.nlm.nih.gov/pmc/articles/PMC515288/>.
205. Dagogo-Jack I, Shaw AT. Tumour heterogeneity and resistance to cancer therapies. *Nat Rev Clin Oncol* [Internet]. Nature Publishing Group; 2018 [cited 2022 May 26]; 15(2):81–94. Available from: <https://www.nature.com/articles/nrclinonc.2017.166>.
206. Weiss J, Sos ML, Seidel D, Peifer M, Zander T, Heuckmann JM, et al. Frequent and Focal FGFR1 Amplification Associates With Therapeutically Tractable FGFR1 Dependency in Squamous-cell Lung Cancer. *Sci Transl Med* [Internet]. 2010 [cited 2022 Jul 21]; 2(62):62ra93. Available from: <https://www.ncbi.nlm.nih.gov/pmc/articles/PMC3990281/>.
207. Lindeman NI, Cagle PT, Beasley MB, Chitale DA, Dacic S, Giaccone G, et al. Molecular testing guideline for selection of lung cancer patients for EGFR and ALK tyrosine kinase inhibitors: guideline from the College of American Pathologists, International Association for the Study of Lung Cancer, and Association for Molecular Pathology. *J Mol Diagn*. 2013; 15(4):415–53.
208. Lindeman NI, Cagle PT, Aisner DL, Arcila ME, Beasley MB, Bernicker EH, et al. Updated Molecular Testing Guideline for the Selection of Lung Cancer Patients for Treatment With Targeted Tyrosine Kinase Inhibitors: Guideline From the College of American Pathologists, the International

Association for the Study of Lung Cancer, and the Association for Molecular Pathology. *J Mol Diagn*. 2018; 20(2):129–59.

209. Itakura H, Achrol AS, Mitchell LA, Loya JJ, Liu T, Westbroek EM, et al. Magnetic resonance image features identify glioblastoma phenotypic subtypes with distinct molecular pathway activities. *Science Translational Medicine* [Internet]. American Association for the Advancement of Science; 2015 [cited 2022 Aug 4]; 7(303):303ra138-303ra138. Available from: <https://www.science.org/doi/10.1126/scitranslmed.aaa7582>.
210. Sacher AG, Dahlberg SE, Heng J, Mach S, Jänne PA, Oxnard GR. Association Between Younger Age and Targetable Genomic Alterations and Prognosis in Non–Small-Cell Lung Cancer. *JAMA Oncology* [Internet]. 2016 [cited 2022 Aug 4]; 2(3):313–20. Available from: <https://doi.org/10.1001/jamaoncol.2015.4482>.
211. Wang S, Shi J, Ye Z, Dong D, Yu D, Zhou M, et al. Predicting EGFR mutation status in lung adenocarcinoma on computed tomography image using deep learning. *European Respiratory Journal* [Internet]. European Respiratory Society; 2019 [cited 2022 Aug 4]; 53(3). Available from: <https://erj.ersjournals.com/content/53/3/1800986>.
212. Loughran CF, Keeling CR. Seeding of tumour cells following breast biopsy: a literature review. *BJR* [Internet]. The British Institute of Radiology; 2011 [cited 2022 Aug 4]; 84(1006):869–74. Available from: <https://www.birpublications.org/doi/full/10.1259/bjr/77245199>.
213. Aerts HJWL, Velazquez ER, Leijenaar RTH, Parmar C, Grossmann P, Cavalho S, et al. Decoding tumour phenotype by noninvasive imaging using a quantitative radiomics approach. *Nat Commun* [Internet]. 2014 [cited 2022 Aug 4]; 5:4006. Available from: <https://www.ncbi.nlm.nih.gov/pmc/articles/PMC4059926/>.
214. Karlo CA, Di Paolo PL, Chaim J, Hakimi AA, Ostrovskaya I, Russo P, et al. Radiogenomics of clear-cell renal cell carcinoma: Associations between CT imaging features and mutations. *Radiology* [Internet]. 2014 [cited 2022 Aug 4]; 270(2):464–71. Available from: <https://www.ncbi.nlm.nih.gov/pmc/articles/PMC4011179/>.
215. Gevaert O, Xu J, Hoang CD, Leung AN, Xu Y, Quon A, et al. Non–Small Cell Lung Cancer: Identifying Prognostic Imaging Biomarkers by Leveraging Public Gene Expression Microarray Data—Methods and Preliminary Results. *Radiology* [Internet]. 2012 [cited 2022 Aug 4]; 264(2):387–96. Available from: <https://www.ncbi.nlm.nih.gov/pmc/articles/PMC3401348/>.
216. Zhou M, Leung A, Echegaray S, Gentles A, Shrager JB, Jensen KC, et al. Non–Small Cell Lung Cancer Radiogenomics Map Identifies Relationships between Molecular and Imaging Phenotypes with Prognostic Implications. *Radiology* [Internet]. 2018 [cited 2022 Aug 4]; 286(1):307–15. Available from: <https://www.ncbi.nlm.nih.gov/pmc/articles/PMC5749594/>.
217. Caetano MS, Zhang H, Cumpian AM, Gong L, Unver N, Ostrin EJ, et al. IL6 Blockade Reprograms the Lung Tumor Microenvironment to Limit the Development and Progression of K-ras-Mutant Lung Cancer. *Cancer Res*. 2016; 76(11):3189–99.
218. Weichand B, Popp R, Dziumbila S, Mora J, Strack E, Elwakeel E, et al. S1PR1 on tumor-associated macrophages promotes lymphangiogenesis and metastasis via NLRP3/IL-1 β . *J Exp Med* [Internet]. 2017 [cited 2022 Sep 25]; 214(9):2695–713. Available from: <https://www.ncbi.nlm.nih.gov/pmc/articles/PMC5584110/>.
219. Greten FR, Grivnickov SI. Inflammation and Cancer: Triggers, Mechanisms and Consequences. *Immunity* [Internet]. 2019 [cited 2022 Sep 25]; 51(1):27–41. Available from: <https://www.ncbi.nlm.nih.gov/pmc/articles/PMC6831096/>.

220. Chiche J, Ilc K, Laferrière J, Trottier E, Dayan F, Mazure NM, et al. Hypoxia-inducible carbonic anhydrase IX and XII promote tumor cell growth by counteracting acidosis through the regulation of the intracellular pH. *Cancer Res.* 2009; 69(1):358–68.
221. Minhajat R, Mori D, Yamasaki F, Sugita Y, Satoh T, Tokunaga O. Organ-specific endoglin (CD105) expression in the angiogenesis of human cancers. *Pathology International* [Internet]. 2006 [cited 2022 Sep 25]; 56(12):717–23. Available from: <https://onlinelibrary.wiley.com/doi/abs/10.1111/j.1440-1827.2006.02037.x>.
222. Duff SE, Li C, Garland JM, Kumar S. CD105 is important for angiogenesis: evidence and potential applications. *The FASEB Journal* [Internet]. 2003 [cited 2022 Sep 25]; 17(9):984–92. Available from: <https://onlinelibrary.wiley.com/doi/abs/10.1096/fj.02-0634rev>.
223. Minhajat R, Mori D, Yamasaki F, Sugita Y, Satoh T, Tokunaga O. Endoglin (CD105) expression in angiogenesis of colon cancer: analysis using tissue microarrays and comparison with other endothelial markers. *Virchows Arch* [Internet]. 2006 [cited 2022 Sep 25]; 448(2):127–34. Available from: <https://doi.org/10.1007/s00428-005-0062-8>.
224. Zhao H, Sun J, Shao J, Zou Z, Qiu X, Wang E, et al. Glucose Transporter 1 Promotes the Malignant Phenotype of Non-Small Cell Lung Cancer through Integrin β 1/Src/FAK Signaling. *J Cancer* [Internet]. 2019 [cited 2022 Sep 25]; 10(20):4989–97. Available from: <https://www.ncbi.nlm.nih.gov/pmc/articles/PMC6775508/>.
225. Liang X, Yang D, Hu J, Hao X, Gao J, Mao Z. Hypoxia Inducible Factor-1 α Expression Correlates with Vascular Endothelial Growth Factor-C Expression and Lymphangiogenesis/Angiogenesis in Oral Squamous Cell Carcinoma. *Anticancer Research* [Internet]. International Institute of Anticancer Research; 2008 [cited 2022 Aug 8]; 28(3A):1659–66. Available from: <https://ar.iijournals.org/content/28/3A/1659>.
226. Swinson DEB, Jones JL, Cox G, Richardson D, Harris AL, O’Byrne KJ. Hypoxia-inducible factor-1 α in non small cell lung cancer: Relation to growth factor, protease and apoptosis pathways. *International Journal of Cancer* [Internet]. 2004 [cited 2022 Sep 25]; 111(1):43–50. Available from: <https://onlinelibrary.wiley.com/doi/abs/10.1002/ijc.20052>.
227. Ren W, Mi D, Yang K, Cao N, Tian J, Li Z, et al. The expression of hypoxia-inducible factor-1 α and its clinical significance in lung cancer: a systematic review and meta-analysis. *Swiss Medical Weekly* [Internet]. EMH Media; 2013 [cited 2022 Sep 25]; (35). Available from: <https://smw.ch/article/doi/smw.2013.13855>.
228. Liu Y-Z, Wang B-S, Jiang Y-Y, Cao J, Hao J-J, Zhang Y, et al. MCMs expression in lung cancer: implication of prognostic significance. *J Cancer* [Internet]. 2017 [cited 2022 Sep 25]; 8(18):3641–7. Available from: <https://www.ncbi.nlm.nih.gov/pmc/articles/PMC5688916/>.
229. Yang J, Ramnath N, Moysich KB, Asch HL, Swede H, Alrawi SJ, et al. Prognostic significance of MCM2, Ki-67 and gelsolin in non-small cell lung cancer. *BMC Cancer* [Internet]. 2006 [cited 2022 Sep 25]; 6:203. Available from: <https://www.ncbi.nlm.nih.gov/pmc/articles/PMC1555597/>.
230. Freeman A, Morris LS, Mills AD, Stoeber K, Laskey RA, Williams GH, et al. Minichromosome Maintenance Proteins as Biological Markers of Dysplasia and Malignancy1. *Clinical Cancer Research.* 1999; 5(8):2121–32.
231. Goel HL, Mercurio AM. VEGF targets the tumour cell. *Nat Rev Cancer* [Internet]. 2013 [cited 2022 Sep 25]; 13(12):871–82. Available from: <https://www.ncbi.nlm.nih.gov/pmc/articles/PMC4011842/>.

232. Frezzetti D, Gallo M, Maiello MR, D'Alessio A, Esposito C, Chicchinelli N, et al. VEGF as a potential target in lung cancer. *Expert Opinion on Therapeutic Targets* [Internet]. Taylor & Francis; 2017 [cited 2022 Sep 25]; 21(10):959–66. Available from: <https://doi.org/10.1080/14728222.2017.1371137>.
233. Yang S-R, Schultheis AM, Yu H, Mandelker D, Ladanyi M, Büttner R. Precision medicine in non-small cell lung cancer: Current applications and future directions. *Seminars in Cancer Biology* [Internet]. 2022 [cited 2022 Aug 5]; 84:184–98. Available from: <https://www.sciencedirect.com/science/article/pii/S1044579X20301644>.
234. Kuo MD, Yamamoto S. Next Generation Radiologic-Pathologic Correlation in Oncology: Rad-Path 2.0. *American Journal of Roentgenology* [Internet]. American Roentgen Ray Society; 2011 [cited 2022 Aug 25]; 197(4):990–7. Available from: <https://www.ajronline.org/doi/10.2214/AJR.11.7163>.
235. Meyer H-J, Wienke A, Surov A. Associations between GLUT expression and SUV values derived from FDG-PET in different tumors—A systematic review and meta analysis. *PLoS One* [Internet]. 2019 [cited 2022 Aug 26]; 14(6):e0217781. Available from: <https://www.ncbi.nlm.nih.gov/pmc/articles/PMC6576787/>.
236. Tan AC. Targeting the PI3K/Akt/mTOR pathway in non-small cell lung cancer (NSCLC). *Thorac Cancer* [Internet]. 2020 [cited 2022 Oct 9]; 11(3):511–8. Available from: <https://www.ncbi.nlm.nih.gov/pmc/articles/PMC7049515/>.
237. Lukey PT, Harrison SA, Yang S, Man Y, Holman BF, Rashidnasab A, et al. A Randomised, Placebo-Controlled Study of Omipalisib (PI3K/mTOR) in Idiopathic Pulmonary Fibrosis. *European Respiratory Journal* [Internet]. European Respiratory Society; 2019 [cited 2020 Jul 22]. Available from: <https://erj.ersjournals.com/content/early/2018/12/14/13993003.01992-2018>.
238. Miles KA, Ganeshan B, Rodriguez-Justo M, Goh VJ, Ziauddin Z, Engledow A, et al. Multifunctional Imaging Signature for V-KI-RAS2 Kirsten Rat Sarcoma Viral Oncogene Homolog (KRAS) Mutations in Colorectal Cancer. *Journal of Nuclear Medicine* [Internet]. Society of Nuclear Medicine; 2014 [cited 2022 Oct 15]; 55(3):386–91. Available from: <https://jnm.snmjournals.org/content/55/3/386>.
239. Weiss GJ, Ganeshan B, Miles KA, Campbell DH, Cheung PY, Frank S, et al. Noninvasive Image Texture Analysis Differentiates K-ras Mutation from Pan-Wildtype NSCLC and Is Prognostic. *PLOS ONE* [Internet]. Public Library of Science; 2014 [cited 2022 Oct 15]; 9(7):e100244. Available from: <https://journals.plos.org/plosone/article?id=10.1371/journal.pone.0100244>.
240. Digumarthy SR, Padole AM, Gullo RL, Sequist LV, Kalra MK. Can CT radiomic analysis in NSCLC predict histology and EGFR mutation status? *Medicine (Baltimore)* [Internet]. 2019 [cited 2022 Oct 15]; 98(1):e13963. Available from: <https://www.ncbi.nlm.nih.gov/pmc/articles/PMC6344142/>.
241. Number of coronavirus (COVID-19) cases and risk in the UK. GOV.UK [Internet]. [cited 2020 May 21]. Available from: <https://www.gov.uk/guidance/coronavirus-covid-19-information-for-the-public>.
242. Deaths registered weekly in England and Wales, provisional - Office for National Statistics [Internet]. [cited 2020 May 21]. Available from: <https://www.ons.gov.uk/peoplepopulationandcommunity/birthsdeathsandmarriages/deaths/bulletins/deathsregisteredweeklyinenglandandwalesprovisional/weekending8may2020>.
243. Report of the WHO-China Joint Mission on Coronavirus Disease 2019 (COVID-19) [Internet]. [cited 2020 May 21]. Available from: [https://www.who.int/publications-detail/report-of-the-who-china-joint-mission-on-coronavirus-disease-2019-\(covid-19\)](https://www.who.int/publications-detail/report-of-the-who-china-joint-mission-on-coronavirus-disease-2019-(covid-19)).

244. Lee EYP, Ng M-Y, Khong P-L. COVID-19 pneumonia: what has CT taught us? *The Lancet Infectious Diseases* [Internet]. Elsevier; 2020 [cited 2020 May 18]; 20(4):384–5. Available from: [https://www.thelancet.com/journals/laninf/article/PIIS1473-3099\(20\)30134-1/abstract](https://www.thelancet.com/journals/laninf/article/PIIS1473-3099(20)30134-1/abstract).
245. Lescure F-X, Bouadma L, Nguyen D, Parisey M, Wicky P-H, Behillil S, et al. Clinical and virological data of the first cases of COVID-19 in Europe: a case series. *Lancet Infect Dis*. 2020.
246. Kooraki S, Hosseiny M, Myers L, Gholamrezanezhad A. Coronavirus (COVID-19) Outbreak: What the Department of Radiology Should Know. *Journal of the American College of Radiology* [Internet]. 2020 [cited 2020 May 21]; 17(4):447–51. Available from: <https://linkinghub.elsevier.com/retrieve/pii/S1546144020301502>.
247. Yang X, Yu Y, Xu J, Shu H, Xia J, Liu H, et al. Clinical course and outcomes of critically ill patients with SARS-CoV-2 pneumonia in Wuhan, China: a single-centered, retrospective, observational study. *The Lancet Respiratory Medicine* [Internet]. 2020 [cited 2020 May 21]; 8(5):475–81. Available from: <http://www.sciencedirect.com/science/article/pii/S2213260020300795>.
248. Zhou F, Yu T, Du R, Fan G, Liu Y, Liu Z, et al. Clinical course and risk factors for mortality of adult inpatients with COVID-19 in Wuhan, China: a retrospective cohort study. *The Lancet* [Internet]. 2020 [cited 2020 May 21]; 395(10229):1054–62. Available from: <http://www.sciencedirect.com/science/article/pii/S0140673620305663>.
249. Thomas-Rüddel D, Winning J, Dickmann P, Quart D, Kortgen A, Janssens U, et al. Coronavirus disease 2019 (COVID-19): update for anesthesiologists and intensivists March 2020. *Anaesthesist* [Internet]. 2020 [cited 2020 May 21]; 1–10. Available from: <https://www.ncbi.nlm.nih.gov/pmc/articles/PMC7095212/>.
250. Xie J, Tong Z, Guan X, Du B, Qiu H, Slutsky AS. Critical care crisis and some recommendations during the COVID-19 epidemic in China. *Intensive Care Med* [Internet]. 2020 [cited 2020 May 21]; 46(5):837–40. Available from: <http://link.springer.com/10.1007/s00134-020-05979-7>.
251. Tsang KW, Ho PL, Ooi GC, Yee WK, Wang T, Chan-Yeung M, et al. A Cluster of Cases of Severe Acute Respiratory Syndrome in Hong Kong. *New England Journal of Medicine* [Internet]. Massachusetts Medical Society; 2003 [cited 2020 May 21]; 348(20):1977–85. Available from: <https://doi.org/10.1056/NEJMoa030666>.
252. Zhao Y-M, Shang Y-M, Song W-B, Li Q-Q, Xie H, Xu Q-F, et al. Follow-up study of the pulmonary function and related physiological characteristics of COVID-19 survivors three months after recovery. *EClinicalMedicine*. 2020; 25:100463.
253. Notes for Guidance on the Clinical Administration of Radiopharmaceuticals and Use of Sealed Radioactive Sources. 2021; 71.
254. Giraudo C, Evangelista L, Fraia AS, Lupi A, Quaia E, Cecchin D, et al. Molecular Imaging of Pulmonary Inflammation and Infection. *Int J Mol Sci* [Internet]. 2020 [cited 2020 Jul 13]; 21(3). Available from: <https://www.ncbi.nlm.nih.gov/pmc/articles/PMC7037834/>.
255. Braune A, Hofheinz F, Bluth T, Kiss T, Wittenstein J, Scharffenberg M, et al. Comparison of Static and Dynamic 18F-FDG PET/CT for Quantification of Pulmonary Inflammation in Acute Lung Injury. *J Nucl Med*. 2019; 60(11):1629–34.
256. Sudre CH, Murray B, Varsavsky T, Graham MS, Penfold RS, Bowyer RC, et al. Attributes and predictors of Long-COVID: analysis of COVID cases and their symptoms collected by the Covid Symptoms Study App. medRxiv [Internet]. Cold Spring Harbor Laboratory Press; 2020 [cited 2020

Oct 26]; 2020.10.19.20214494. Available from:
<https://www.medrxiv.org/content/10.1101/2020.10.19.20214494v1>.

257. Horby P, Lim WS, Emberson J, Mafham M, Bell J, Linsell L, et al. Effect of Dexamethasone in Hospitalized Patients with COVID-19: Preliminary Report. medRxiv [Internet]. Cold Spring Harbor Laboratory Press; 2020 [cited 2020 Jul 9]; 2020.06.22.20137273. Available from:
<https://www.medrxiv.org/content/10.1101/2020.06.22.20137273v1>.
258. Ackermann M, Verleden SE, Kuehnel M, Haverich A, Welte T, Laenger F, et al. Pulmonary Vascular Endothelialitis, Thrombosis, and Angiogenesis in Covid-19. N Engl J Med [Internet]. Massachusetts Medical Society; 2020 [cited 2020 Jul 13]; 383(2):120–8. Available from:
<https://doi.org/10.1056/NEJMoa2015432>.